Spring 2015

Spectroscopic characterization and photochemistry of nitrogen-containing molecules relevant to Titan's atmosphere

Deepali N. Mehta-Hurt
Purdue University

Graduate School Form 30
(Updated 11/20/2014)

PURDUE UNIVERSITY
GRADUATE SCHOOL
Thesis/Dissertation Acceptance

This is to certify that the thesis/dissertation prepared

By Deepali N. Mehta-Hurt

Entitled SPECTROSCOPIC CHARACTERIZATION AND PHOTOCHEMISTRY OF NITROGEN-CONTAINING MOLECULES RELEVANT TO TITAN'S ATMOSPHERE

For the degree of Doctor of Philosophy

Is approved by the final examining committee:

Timothy Zwier

Adam Wasserman

Lyudmila Slipchenko

Paul Wenthold

To the best of my knowledge and as understood by the student in the Thesis/Dissertation Agreement, Publication Delay, and Certification/Disclaimer (Graduate School Form 32), this thesis/dissertation adheres to the provisions of Purdue University's "Policy on Integrity in Research" and the use of copyrighted material.

Timothy Zwier

Approved by Major Professor(s): _____

_____

Approved by: R. E. Wild 04/23/2015

Head of the Department Graduate Program Date

SPECTROSCOPIC CHARACTERIZATION AND PHOTOCHEMISTRY OF NITROGEN-CONTAINING MOLECULES RELEVANT TO TITAN'S ATMOSPHERE

A Dissertation

Submitted to the Faculty

of

Purdue University

by

Deepali N. Mehta-Hurt

In Partial Fulfillment of the

Requirements of the Degree

of

Doctor of Philosophy

May 2015

Purdue University

West Lafayette, Indiana

To my family, with love.

ACKNOWLEDGMENTS

I would like to start out by expressing my gratitude towards my advisor Dr. Timothy S. Zwier. Simply put, Tim is not only an exceptional scientist and advisor, but is also a great person. I feel extremely fortunate to have had him as my advisor. Thank you for all of your guidance during my graduate studies, for our thought-provoking conversations, and for providing me with the opportunity to learn from you. I would also like to thank my thesis committee, consisting of Dr. Lyudmila Slipchenko, Dr. Paul Wenthold, and Dr. Adam Wasserman. Thank you for your contributions to this thesis and to my time here at Purdue. A special thanks must be given to Dr. Slipchenko and Dr. Ben Nebgen who provided much-needed theoretical help in understanding the excited state spectroscopy of the phenylcyanomethyl radical. Of course, I must thank the past and present members of the Zwier group: Dr. Brian Dian, Dr. Jaime Stearns, Dr. Joshua Newby, Dr. Christian Mueller, Dr. William James III, Dr. Chirantha Rodrigo, Dr. Anna Gutberlet, Dr. Joshua Sebree, Dr. Vanesa Vaquero-Vara, Dr. Ryoji Kusaka, Dr. James Redwine, Dr. Evan Buchanan, Dr. Jacob Dean, Dr. Nathanael Kidwell, Zachary Davis, Joseph Korn, Di Zhang, Nicole Burke, Joseph Gord, Patrick Walsh, Daniel Hewett, John Hopkins, Khadija Jawad, and our special trio of undergraduates Rachel Clayton, Polina Navotnaya, and Alex Parobek. I am extremely grateful for those who I got to learn from and with, for your help, and the friendships formed during my time in the research group. In particular, I owe a special thanks to Dr. Vanesa Vaquero-Vara and Di Zhang for all of their assistance related to the nitrile microwave spectroscopy presented in this thesis.

My research and stay at Purdue would not have been as smooth if it were not for the help from the staff in the Chemistry Department, so naturally I must acknowledge them. I would like to thank the Amy Instrumentation Facility for their help. In particular, Tim Selby and Randy Replogle have been a great help throughout my time. In

the Chemistry Shop, I must thank Blaine Schutz, Dallas Eikenberry, Betty Dexter, and Ned Gangwer. In the Chemistry Store, I owe thanks to the late Jim Furr, Craig MacDonald, Alan Springer, and Robert Bisher. My gratitude also goes to out Suzy Gustafson and Darci Decamp in the Procurement Center, as well as Rob Reason in the Copy Center for their help. Patricia Herrera, Cathy Lofthouse, and Lisa Wilson in the Business Office have been very helpful on many occasions. I must also mention the Chemistry Office, and in particular, Dr. Bob Wild, Betty Hatfield, Debbie Packer, Lynn Rider, and Steve Scherer. Thank you all for your help in various ways and times throughout my stay at Purdue. And to Elizabeth (Liz) Hewitt, thank you very much for all of your guidance in this thesis formatting process.

Outside of Purdue, I must thank Dr. Timothy Schmidt at The University of New South Wales for his help in acquiring the dispersed fluorescence spectra of the phenylcyanomethyl radical. His data have been a quite useful guide in characterizing and interpreting the spectroscopy of the radical species.

To Ms. Cassandra Whitsett, my high school chemistry teacher, I thank you for showing me how chemistry can be fun, challenging, and a great puzzle to solve. Thank you for also teaching me about humor and facetiousness, it has helped me in the Zwier group and personally. I owe a thanks to my undergraduate research advisor Dr. Zhuangjie Li at California State University, Fullerton (CSUF) for challenging me, guiding me, and persuading me to choose physical chemistry for graduate school. To Dr. Mark Filowitz at CSUF, you are a fantastic mentor. You always supported me, were honest with me, and were never too busy to give me some of your time for guidance.

To my family as a whole, I am indebted. I have been blessed beyond measure to be surrounded by such a supporting environment, and to have positive examples to look up to while growing up. To my new family, from the Hurt side, you all have been supportive, fun, and loving and I am so grateful for the connection I have with you all.

More directly, I would like to also express sincere gratitude for my parents, Nikhil and Nimisha, as well. You are and always will be my parents, but as I am growing older, you are also my friends. No words can accurately describe my level of love, respect, and admiration I have for you both, and for all of the sacrifices you have made in your lives

to raise me. You have quite literally supported me from day one, and believed in me even when I did not believe in myself. And to my parents, John and Tammy, I must thank you as well. You have welcomed me into your lives and treated me as your very own little girl from day one of meeting you. You have been so helpful, loving, and supportive and I appreciate you greatly. All four of you (Nikhil, Nimisha, John, Tammy) are wonderful parents, I love you, and my hope is that Matt and I can be as good parents to our children as you have been to us. And now I must express my love and appreciation for this "Matt character" in the preceding text. To my dear husband Matthew, so many positive thoughts come to my mind when I think of what you have brought to my life. I appreciate how much you have helped support and comfort me throughout this, and your contributions to this thesis are many. You are such a loving, patient, understanding, honest, unselfish, and supportive human being. You truly are a gift from God. I love you, and look forward to what our future holds.

TABLE OF CONTENTS

Page

Page

Page

Page

LIST OF TABLES

Tables Page

LIST OF FIGURES

Figure Page

Figure Page

Figure Page

Figure Page

ABSTRACT

Mehta-Hurt, Deepali N. Ph.D., Purdue University, May 2015. Spectroscopic Characterization and Photochemistry of Nitrogen-Containing Molecules Relevant to Titan's Atmosphere. Major Professor: Timothy S. Zwier.

Titan's atmospheric chemistry has been the source of intrigue since the planetary body's discovery. Though there is a growing understanding of the atmospheric chemistry of small molecules on Titan, much less is known about larger molecule formation, and particularly about nitrile chemistry. This dissertation characterizes nitrile/isonitrile intermediates that are postulated to be important in Titan's atmosphere, adding to the necessary foundation for understanding Titan's atmospheric chemistry. The vibronic spectroscopy of *para*-diisocyanobenzene (*p*DIB, C≡N-Ph-N≡C) has been characterized as a first step towards photochemical studies that can test the transformation of the isonitrile group to other nitrogen-based functionalities. *p*DIB was found to have a excitation spectrum dominated by Herzberg-Teller vibronic coupling to a nearby second electronic excited state, and the S_0-S_1 origin was found to be weak, due to the near cancellation of the transition dipole moment upon electronic excitation. The phenylcyanomethyl radical (PCM, Ph-ĊH-C≡N), a doubly resonance-stabilized radical (RSR), was also spectroscopically characterized for the first time. The ionization potential, excited state lifetime, and rotational band contour of PCM at the D_0-D_1 electronic origin were obtained. The spectroscopy of (E)- and (Z)-phenylvinylnitrile ((E)- and (Z)-PVN, Ph-CH=CH-C≡N), structural isomers of the simplest polycyclic aromatic nitrogen heterocycle (PANH) quinoline, was also characterized. Both (E)- and (Z)-PVN were found to be planar in the ground and first excited electronic state. (E)-

PVN was found to participate in extensive Duschinsky mixing, whereas Duschinsky mixing was not as prominent in (Z)-PVN. The spectral signatures for (E)- and (Z)-PVN, were additionally used to carry out ultraviolet hole-filling (UVHF) experiments to test for the formation of quinoline through photoisomerization. Lastly, the microwave spectroscopy of 4-pentenenitrile (CH_2=$CHCH_2CH_2C$≡N), 4-pentynenitrile (N≡C-CH_2-CH_2-C≡CH), and glutaronitrile (N≡C-CH_2-CH_2-CH_2-C≡N) was studied. Microwave transitions of each molecule were assigned to particular conformations, providing high resolution microwave data that can be used in future microwave searches for their presence in Titan and elsewhere in interstellar space.

CHAPTER 1: INTRODUCTION

1.1. Studying Titan: Motivation and Status Quo

Titan is the sixth moon of Saturn, and its atmosphere is surrounded by a dense optical haze that is orange in color. Scientists are interested in the chemistry of Titan because they seek to understand (1) the complex atmospheric chemistry that leads to the observed orange haze as well as understand (2) the chemistry that may have occurred on prebiotic Earth, due to Titan's status as a model system of primordial Earth. In studying both of these areas, nitrogen-containing functionalities are thought to play important roles.

1.1.1. Titan's Characteristics and Atmospheric Chemistry

The atmosphere of Titan comprises of about 98% nitrogen (N_2), 1.5% percent methane (CH_4), and traces of other organics.[1] Similar to the water cycle on Earth, Titan is known to have a methanological cycle with methane clouds and lakes filled with ethane, methane, and traces of other organics.[1-3] Aside from the organics lakes, Titan's surface is known to have a frozen water crust with traces of organics.[1-3] Furthermore, a water ocean with dissolved organics exists just underneath the surface of Titan, below which is a layer of water-ice mixtures, followed by an ice-rock mixture.[3] Titan is also known to have a reducing atmosphere, much like early Earth, which was partially reducing prior to the emergence of life.[2, 4] With (1) a nitrogen dominated atmosphere containing trace organics, (2) a methanological cycle analogous to Earth's hydrological cycle, and (3) a partially reducing atmosphere, Titan is regarded as a model system by scientists for the study of primordial Earth. As such, Titan is a modern "laboratory" to learn about the chemical processes present prior to the origin of life on Earth.

Titan's chemistry takes place via ion and neutral pathways. Though chemistry on Titan can be initiated via the bombardment of N_2 and CH_4 with energetic particles, the atmospheric chemistry of Titan is predominantly driven via the absorption of solar radiation. Photolysis of N_2 ($\lambda \leq 100$ nm) and CH_4 ($\lambda \leq 150$ nm) initiates much of the photochemistry in Titan's atmosphere and leads to the formation of other small organic molecules that are either open or closed shell neutrals, and/or ions.[1] Some of the photoproducts generated in the atmosphere of Titan include C_2H_6, C_2H_4, C_2H_2, C_4H_2, and nitrile species such as HCN, HC_3N, C_2N_2.[1] These photoproducts absorb longer wavelengths (which have not been absorbed by the N_2 and CH_4) and can undergo photochemical reactions of their own. Amongst the various photoproducts lie nitrile molecules, which are unique because the nitrile functionality is quite stable when formed, relative to other organic functionalities.[5] Our interest specifically lies in studying nitrile intermediates because they are less well-characterized and their chemical evolution to other nitrogen-containing organic functionalities is less well-understood (see Section 1.1.2.). In pursuing these studies, we hope to contribute to the understanding of formation processes for (1) nitrogen-containing, prebiotically relevant molecules and (2) structurally enigmatic tholins, which are also thought to be nitrogen-containing, and responsible for the orange haze of Titan.

1.1.2. Studying the Atmosphere of Titan

In the field of atmospheric chemistry, an atmosphere of interest can be studied either via observation, theoretical models, and/or laboratory experiments.[6] Observations and analysis of Titan data is not easy to obtain due to the difficulties of reaching the site. However, the observations from Titan can help provide boundary conditions for laboratory work and assess the validity of theoretical models of the atmosphere.[6] For example, the Cassini mission has provided invaluable data that has deepened understanding of Titan's atmosphere.[7]

Theoretical models are comprised of hundreds of chemical reactions that are based on laboratory studies. These models incorporate rate constants, product branching

ratios, photochemical quantum yields, absorption profiles, diffusion rates, etc., and rely heavily on laboratory-based experiments and observations for input data and parameters. Theoretical models, provided they well-represent the atmosphere, can provide predictions about molecular constituents that should be present in sufficient concentrations to be observed.[6] Current photochemical models can account for many small hydrocarbons and nitriles, but discrepancies remain amongst various models. For example, due to the absence of laboratory data, Krasnopolsky attempts to provide a complete model by postulating a route towards the formation of pyridine in Titan's atmosphere: $C_3N + C_2H_6 \rightarrow C_5H_5N + H$.[8] The same reactants, however, are predicted to form HC_3N and C_2H_5 in a model by Yung years earlier.[9] Thus, these models need to be refined with the aid of laboratory experiments to obtain an accurate simulation of Titan's photochemistry. Furthermore, there is a pressing need to expand these models (and consequently laboratory experiments) to include a larger molecular size regime, where prebiotically relevant molecules enter the reaction schemes, and an understanding of tholin formation can arise. In this increased molecular size regime, isomers (structural, conformational, etc.) become increasingly important due to their different reactivities. However, much less is known about chemical composition and reactive pathways to and from larger molecules, and oftentimes hydrocarbon and nitrile photochemical products are simply designated as forming "polymer" product, with no clear chemical and isomeric identity. [8, 10-13]

Aside from providing valuable input data to theoretical models and helping refine them, laboratory studies can also provide an experimental database for future observation missions via spectroscopic characterization.[6] With regards to laboratory experimentation, one can imagine that there are a multitude of molecules that the community can study, and such a task may be daunting at first. Studying molecules by brute force is cumbersome, and perhaps a better strategy for laboratory-based studies is to study the chemistry and photochemistry of particular reactive intermediates that are thought to be key in the chemistry of Titan's atmosphere. This thesis will follow the latter strategy, and Section 1.2. will outline the dissertation projects undertaken towards elucidating Titan's nitrogen-based chemistry.

1.2. Organization of Thesis

The goal of this dissertation is to study nitrile/isonitrile molecules that are thought to be important reactive intermediates en route towards tholins and/or prebiotically relevant molecules in order to gain a better understanding of these chemical pathways in Titan's atmosphere. Chapter 2 provides information on the experimental apparatuses and techniques used to carry out the work in this dissertation. Chapter 3 provides the spectroscopic characterization of *para*-diisocyanobenzene (*p*DIB, C≡N-Ph-N≡C). *p*DIB is of particular interest due to its possession of two isonitrile groups. In contrast to the ultra-stable nitrile functional group, which may be more difficult to photoprocess, the isonitrile group provides a fascinating alternative to incorporating nitrogen into various organic functionalities that may be pertinent in Titan's atmosphere.

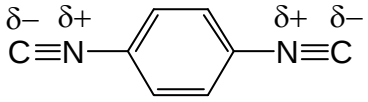

para-diisocyanobenzene (*p*DIB)

Chapter 4 describes the spectroscopic characterization of the phenylcyanomethyl radical (PCM, Ph-ĊH-C≡N), which is proposed to be an important candidate in the formation of larger molecules in Titan's atmosphere. PCM is a doubly resonance-stabilized radical and is the nitrile analog of the 1-phenylpropargyl radical (1PPR, Ph-ĊH-C≡CH). Its characterization helps contribute data on nitrile species, which are generally less well-understood than their hydrocarbon counterparts.

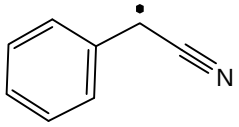

phenylcyanomethyl radical (PCM)

Chapter 5 presents the results of the spectroscopic characterization of (E)- and (Z)-phenylvinylnitrile ((E)- and (Z)-PVN, Ph-CH=CH-C≡N). (E)- and (Z)-PVN are structural isomers of quinoline, and as such, (E)- and (Z)-PVN are thought to be important reactive intermediates that may photoisomerize to quinoline. The characterization of (E)- and (Z)-PVN provided spectroscopic signatures for ultraviolet

hole-filling (UVHF) experiments that tested the formation of quinoline upon (E)- and (Z)-PVN photoexcitation, the results of which are also discussed in Chapter 5. The study on (E)- and (Z)-PVN is an extension of previous Zwier group studies on the spectroscopy and photochemistry of (E)- and (Z)-phenylvinylacetylene ((E)- and (Z)-PVA, Ph-C(H)=C(H)-C≡CH), which were tested for naphthalene formation upon photoirradiation.

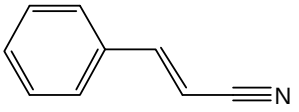

(E)-phenylvinylnitrile ((E)-PVN)

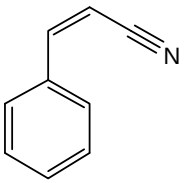

(Z)-phenylvinylnitrile ((Z)-PVN)

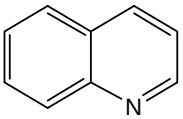

quinoline

Chapter 6 contains the microwave spectroscopy of the molecules 4-pentenenitrile (CH_2=$CHCH_2CH_2C$≡N), 4-pentynenitrile (N≡C-CH_2-CH_2-C≡CH), and glutaronitrile (N≡C-CH_2-CH_2-CH_2-C≡N). The characterization of these molecules provides the necessary spectroscopic signatures for their search in space and on Titan.

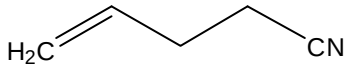

4-pentenenitrile

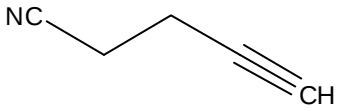

4-pentynenitrile

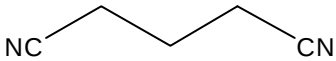

glutaronitrile

4-pentenenitrile is thought to be an important recombination product of the allyl and cyanomethyl radical, and 4-pentynenitrile is anticipated to be the recombination product of the propargyl and cyanomethyl radicals. Moreover, 4-pentynenitrile is a structural isomer of pyridine (C_5H_5N), a simple nitrogen heterocycle. The characterization of 4-pentynenitrile also serves as a first step in studies aimed at exploring 4-pentynenitrile photoisomerization to pyridine. Glutaronitrile is a potential product from the reaction of the cyanomethyl and cyanoethyl radicals, and furthermore interesting due to its conformational flexibility.

1.3. References

1. Raulin, F., et al., Chem. Soc. Rev., 2012. **41** (16): p. 5380-5393.
2. Balucani, N., Chem. Soc. Rev., 2012. **41** (16): p. 5473-5483.
3. Tobie, G., D. Gautier, and F. Hersant, The Astrophysical Journal, 2012. **752** (2): p. 125.
4. Kasting, J.F., Science, 1993. **259**: p. 920-926.
5. Bernstein, M.P., et al., The Astrophysical Journal, 2004. **601** (1): p. 365.
6. Cable, M.L., et al., Chem. Rev., 2012. **112** (3): p. 1882-1909.
7. Waite, J.H., et al., Science, 2007. **316** (5826): p. 870-875.
8. Krasnopolsky, V.A., Icarus, 2009. **201** (1): p. 226-256.
9. Yung, Y.L., Icarus, 1987. **72**: p. 468-472.
10. Wilson, E.H. and S.K. Atreya, Journal of Geophysical Research-Planets, 2004. **109** (E6).
11. Krasnopolsky, V.A., Planetary and Space Science, 2010. **58** (12): p. 1507-1515.
12. Banaszkiewicz, M., et al., Icarus, 2000. **147** (2): p. 386-404.
13. Krasnopolsky, V.A., Icarus, 2014. **236** (0): p. 83-91.

CHAPTER 2: EXPERIMENTAL METHODS

This chapter will provide a general description of the methods that were commonly used throughout the various projects in this dissertation. Techniques that are specific to particular projects will be described in their respective chapters.

2.1. Supersonic Expansion

The samples under study are prepared in collision-free conditions in the gas phase. To achieve this end, supersonic expansion is used as a means.[1-3] The analyte of interest is loaded onto either cotton or glass wool, and placed directly into the sample holder in either a Series 9 general valve (fluorescence chamber, Section 2.2.1.) or a Jordan Valve (time-of-flight mass spectrometer chamber, Section 2.2.2.). When a sample has sufficient vapor pressure at room temperature (Series 9 general valve) or 45˚C (20 Hz, Jordan valve operating temperature), no heating is required; if the sample does not have sufficient vapor pressure under these conditions, it may be heated by utilizing a Variac in conjunction with a heating rope. In the event that the sample has too high of a vapor pressure under normal operating conditions of the Jordan valve, the valve can be equipped with an external sample holder such that the sample is not directly heated to 45 ˚C.

The sample is then entrained in a high backing-pressure gas (He at 3.8 bar total, or Ar at 1.7 bar total) and expanded through a small orifice (500-800 μm diameter) into the vacuum chamber. Upon expansion into the chamber, the sample undergoes many collisions with the backing gas, thereby removing internal energy from the molecule i.e. cooling the molecule down to its zero-point vibrational energy level in the ground state. The supersonic expansion also leaves the molecules isolated and collision-free. These

cold molecules are ideal for gas phase spectroscopy because the number of transitions they can undergo are minimized, thereby simplifying their spectra for assignment. Once the molecules are prepared, their spectroscopy can be investigated with either fluorescence or ionization-based detection.

2.2. Vacuum Chambers

The Zwier laboratory is equipped with vacuum chambers that enable either fluorescence or ionization-based detection. In the case where a molecule has a high fluorescence quantum yield or is difficult to ionize, the fluorescence chamber provides a highly sensitive means for exploring the spectroscopy of molecules, limited only by the lack of mass resolution. This mass resolution is key in cases where the sample is believed to be impure or suspect to thermal degradation. An alternative to the fluorescence chamber is the time-of-flight mass spectrometer (TOF-MS) chamber, which readily provides for the collection of data with mass resolution. A brief overview of the fluorescence chamber and TOF-MS chamber are provided below.

2.2.1. Fluorescence Chamber

A schematic of the fluorescence chamber is presented in Figure 2.1. Timings for the laser, pulsed valve, and electronics were all controlled via triggers generated by a digital delay pulse generator (Berkeley Nucleonics Corporation Model 555). The chamber is pumped down to a pressure of about 10-30 millitorr by a Rootsblower system that is backed by two mechanical pumps. Once the chamber is pumped down, the sample is entrained in a high backing pressure gas (typically 3.8 bar He) and supersonically expanded into the vacuum chamber through a 500-800 μm orifice. Typically, PEEK poppets are used for temperatures above 90 ˚C, and either Teflon or KEL-F poppets are used for temperatures below 90 ˚C.

The frequency doubled output of a dye laser is then introduced into the fluorescence chamber through baffle arms, and the laser is aligned and timed to interact

with the cold, isolated molecules. Upon absorption of a resonant photon, the molecule can fluoresce; this total fluorescence is collected by two spherical mirrors, and then exits the chamber through a hole on the bottom spherical mirror. The total fluorescence is then collimated and can be directed into two separate detection schemes: 1) towards a photomultiplier tube (PMT) for laser induced fluorescence (LIF) studies, or 2) through a monochromator (Spex Jobin Yvon 750i) towards a charge-coupled device (CCD) camera for dispersed fluorescence (DFL). The fluorescence chamber is equipped with a translation stage with mirror that facilitates the easy switch between LIF (translation stage in) and DFL experiments (translation stage out).

In the case of LIF experiments, the current output from the PMT is sent to a Tektronix oscilloscope where the fluorescence is gated and read by LabView software on a personal computer. Longpass cut-off filters (typically chosen to be ~10 nm to the red of the tuning region) are placed in front of the PMT in order to minimize the effects of scattered light. In the event that scattered light is prominent, the fluorescence collection gate on the oscilloscope can also be moved off of the scattered light to increase the signal to scatter ratio.

In DFL experiments, the total fluorescence is directed into the monochromator, and dispersed across a grating and onto the CCD. The monochromator (Spex Jobin Yvon 750i) wavelength position and slitwidth are controlled by LabView software; a slitwidth of 100μm was typically used, resulting in a resolution of about 6-8 cm^{-1}. The output of the CCD is read by software on a personal computer, and the CCD is cooled to minimize noise. Cosmic rays are removed using the CCD software. To remove the scatter light effects from acquisitions, a background is taken by detuning the pulsed valve time, such that a background can be collected and subtracted from the original data. Both LIF and DFL will be developed further in 2.3.1.

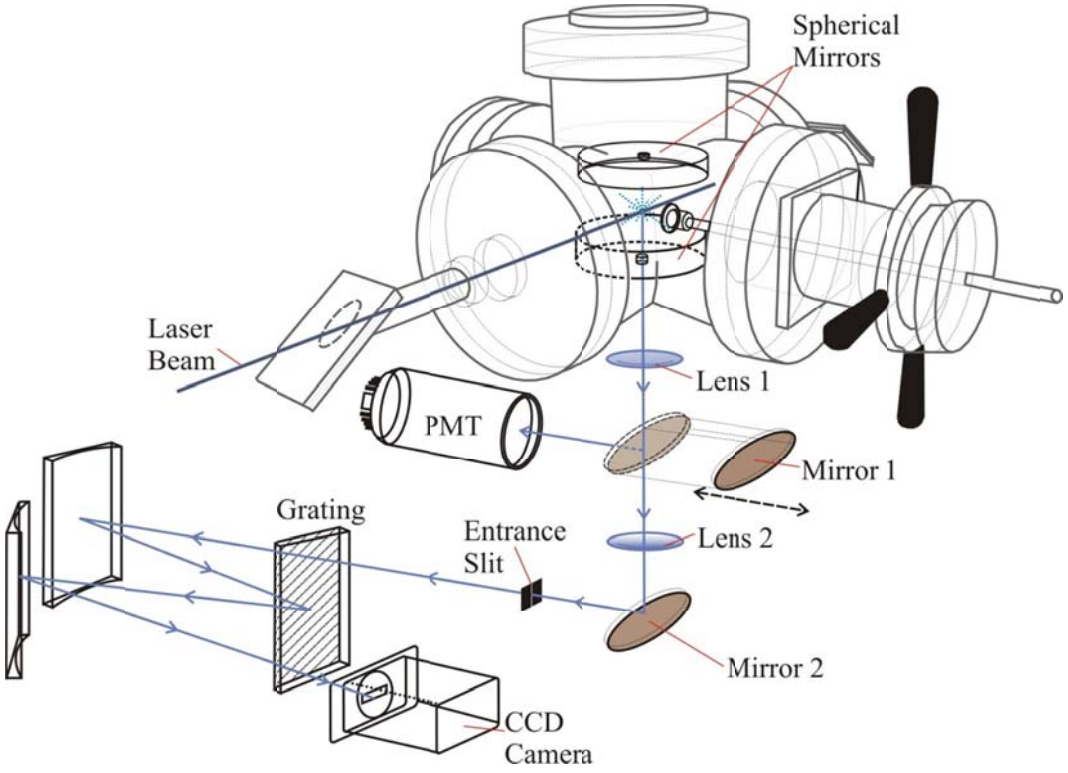

Figure 2.1. Schematic of the fluorescence chamber. The black dotted, double-headed arrow below Mirror 1 and above Lens 2 represents the translation stage that can be in the "in" position for LIF studies, and in the "out" position for DFL studies.

2.2.2. Time-of-Flight Mass Spectrometer Chamber

The time-of-flight mass spectrometer is diagrammed in Figure 2.2. A Berkeley Nucleonics Corporation digital delay pulse generator (Model 555) was used to control the timings of lasers, the pulsed valve, and electronics. The chamber is differentially pumped by two diffusion pumps (Varian VHS-6); the ion source and time-of-flight diffusion pumps get to an ultimate pressure of 10^{-5} Torr and 10^{-6} Torr, respectively, when the pulse valve is operating. The diffusion pumps are outfitted with either cyrocoolers (Polycold P20) or liquid nitrogen cryotraps (Varian BGA 6" ASA) in order to reduce backstreaming of pump oil and reduce background water vapor.

Samples are entrained in a high backing pressure gas (typically 1.7 bar Ar), and are supersonically expanded into the vacuum chamber through a 500 μm orifice. After free expansion, the molecules enter the ion source of a Wiley-McLaren TOF-MS,[4] and

are interrogated with a laser for spectroscopic characterization and ionization. After ionization, the ions are extracted towards the flight tube via the combination of a repeller plate (+ 3000 V) and draw-out-grid (approximately + 2300-2700 V). Prior to entering the flight tube, an Einzel lens (about + 900-1100 V) is used to focus the ion packet. The focused ion packet then enters the field-free region of the 1 meter flight tube, and ultimately gets detected by a microchannel plate (MCP, R.M. Jordan). The raw ion signal is subsequently amplified twice by a factor of 5X, leading to a net amplification of 25X by a Stanford Research Systems SR240 fast preamplifier. The amplified ion signal is then fed into a digital oscilloscope for monitoring (Textronix 3043c) and data is collected via LabVIEW software on a personal computer.

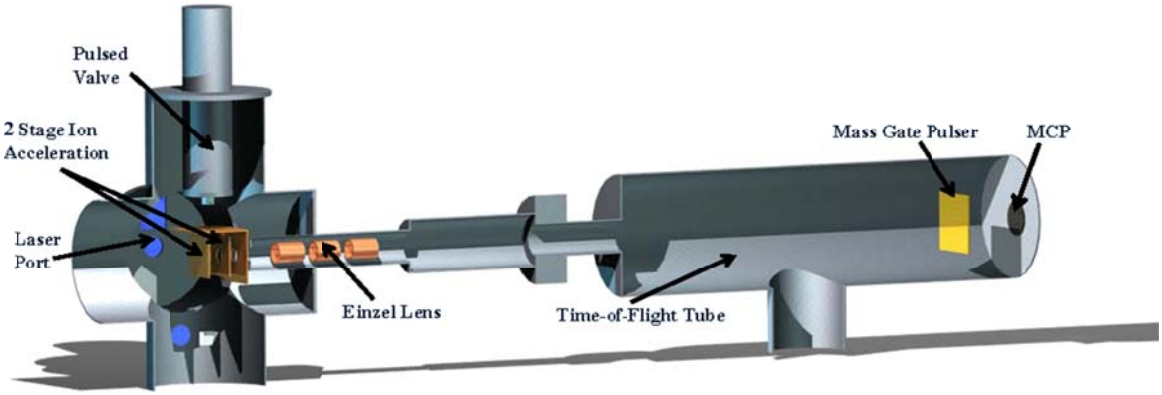

Figure 2.2. Schematic of the time-of-flight mass spectrometry chamber.

2.3. Spectroscopy Methods

2.3.1. Fluorescence Methods

Fluorescence offers a highly sensitive form of detection for species that have a sufficient fluorescence quantum yield. In order to collect an excitation spectrum of a molecule, laser induced fluorescence (LIF) may be used (Figure 2.3). The frequency doubled ultraviolet (UV) output of a dye laser can be aligned and timed to intersect a

collision-free portion of the supersonic expansion containing the analyte. The laser wavelength can be tuned through a region of interest, and when the laser wavelength is resonant with the molecule, absorption followed by fluorescence will occur provided a sufficient fluorescence quantum yield exists. This total fluorescence can be collected, collimated, and directed towards a photomultiplier tube (PMT); by collecting the total fluorescence as a function of excitation wavelength, and excitation spectrum is generated.

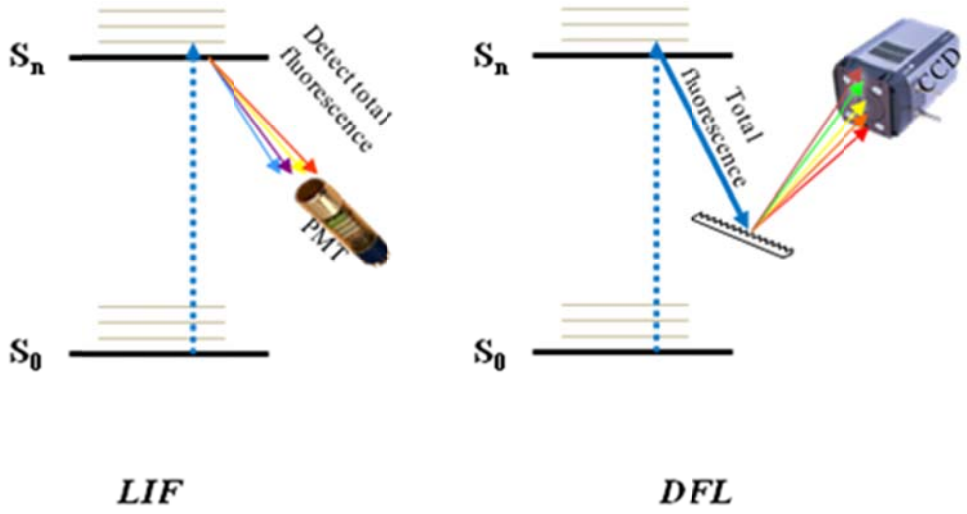

Figure 2.3. Schemes for laser induced fluorescence (LIF) and dispersed fluorescence (DFL). See text for further details.

Dispersed fluorescence (DFL) can be utilized to obtain ground state information on a molecule of interest (Figure 2.3). DFL spectra are acquired by pumping a particular transition in the excitation spectrum, capturing the total fluorescence and directing it to a monochromator where it is dispersed and directed onto a charge-coupled device camera. Both LIF and DF provide a powerful fluorescence-based characterization of the excited and ground states of the molecules under study. The techniques are an ideal one laser experiment, limited only by the lack of mass resolution.

2.3.2. Resonant Two-Photon Ionization

Resonant two-photon ionization (R2PI) provides for the ionization and spectroscopic characterization of molecules in the TOF-MS (Figure 2.4). As the name implies, R2PI is a two-photon process. A first (resonant) photon takes the molecules from the zero-point vibrational energy level in the ground state to vibrational levels of the electronically excited state, and a second photon ionizes the molecule. When the ionization potential of the molecule is sufficiently low, two photons of the same energy can be used; this process is termed one-color resonant two-photon ionization or 1C-R2PI (Figure 2.4). In the case of the nitriles characterized in this thesis, the ionization potentials tend to be higher than their hydrocarbon analogs. Thus, a second photon of higher energy is typically used to ionize the molecule with 2-color resonant two-photon ionization (2C-R2PI) (Figure 2.4). A convenient second "color" is provided by an ArF excimer laser (EX5, GAM Laser, Inc.) at 193 nm. In 1C-R2PI both photons are inherently spatially and temporally overlapped, but in the case of 2C-R2PI the spatial and temporal overlap of the photons must be established. A benefit of 2C-R2PI is that saturation effects, which may be present in 1C-R2PI, can be removed. When a 2C-R2PI experiment is set up with two dye lasers, it is possible to obtain a photoionization efficiency (PIE) scan of a molecule. This is achieved by parking the resonant photon on a transition from the zero-point vibrational energy level in the ground state to an excited state, and turning the wavelength of the ionization laser until an onset of ion signal is observed. The sum of the energy of the two photons used at the onset of ion signal indicates the ionization potential for the molecule.

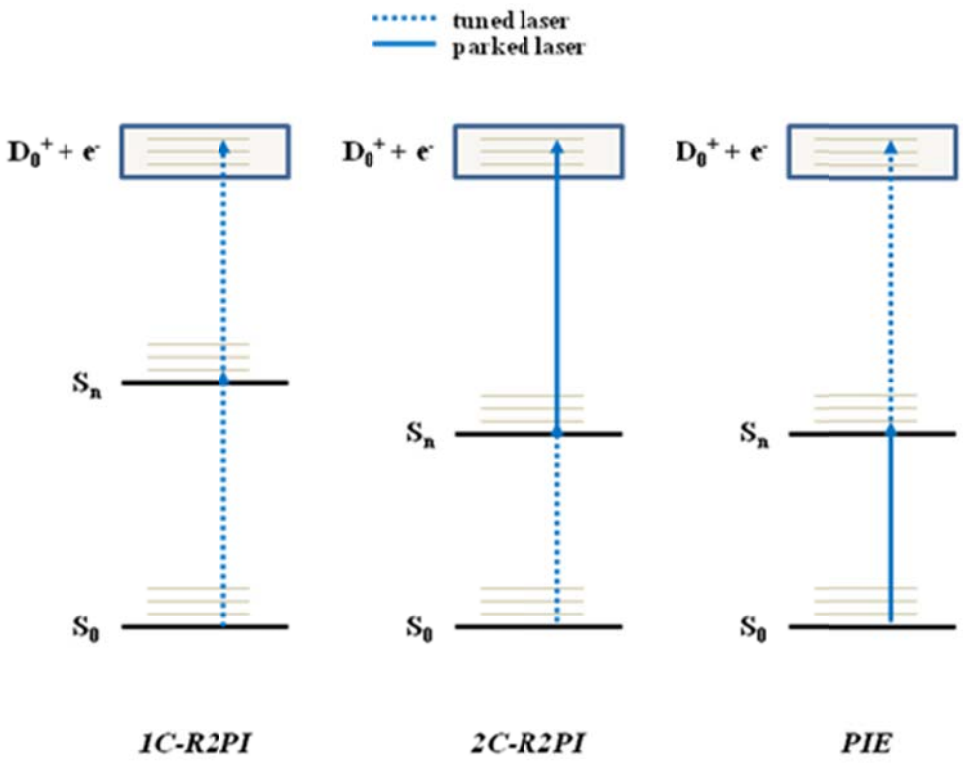

Figure 2.4. Schemes for one-color resonant two-photon ionization (1C-R2PI) and two-color resonant two-photon ionization (2C-R2PI) and photoionization efficiency (PIE) scans. The schemes presented here are for a closed shell neutral species. In the case of an open-shell neutral (radical), the ground state would be designated as D_0, the excited state as D_n, and the ion state as S_0^+.

2.3.3. Multi-resonance Methods

Both of the abovementioned LIF and R2PI allow for the determination of the excited spectrum for a molecule of interest, but there are oftentimes cases where isomers (conformational, structural, etc.) and/or other species (clusters, impurities) exist in the expansion. In these cases, both LIF and R2PI merely provide a composite excitation spectrum of all the species present in the expansion, and alternate detection schemes are necessary for isomer-specific detection. Multi-resonance methods provide a method to simplify the excitation spectrum into components corresponding to particular isomer. Examples of multi-resonance methods include UV-UV hole-burning (UV-UV HB) and UV depletion (UVD) spectroscopy (Figure 2.5).

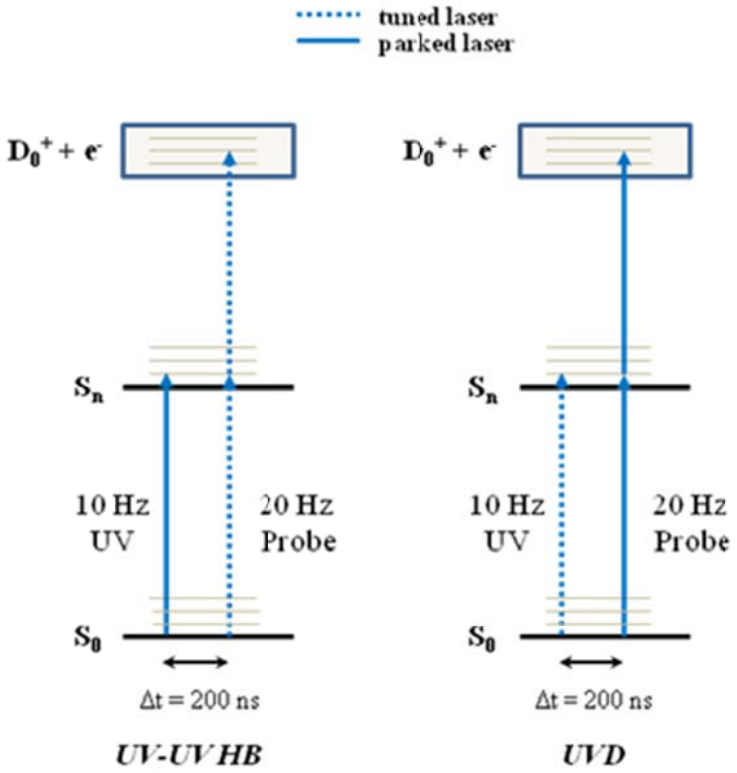

Figure 2.5. Schemes for UV-UV hole-burning (UV-UV HB) and UV depletion (UVD).

UV-UV HB is a double resonance experiment where there is a hole-burn laser operating at 10 Hz and a probe laser operating at 20 Hz. The hole-burn and probe lasers are spatially overlapped but temporally separated such that the hole-burn laser precedes the probe laser by approximately 200 ns. The hole-burn laser is parked on a transition in the excitation spectrum, and the probe laser is tuned through a spectral region of interest. Whenever the probe laser tunes through a transition that shares the same ground state level as the hole-burn laser, depletion ("hole") is observed when using active baseline subtraction via a gated integrator (Stanford Research Systems SR250). For experimental ease, the hole-burn laser is typically parked on the strongest transition in the region of interest. Once a hole-burning spectrum is obtained for a particular species, the process may be repeated if other unburned transitions remain.

UVD is an important variant of UV-UV HB that allows for the detection of radiationless transitions in LIF and transitions with reduced ionization efficiency in R2PI. In UVD, the hole-burn laser (10 Hz) is tuned through the spectral region of interest, and the probe laser (20 Hz) is parked on a particular transition. UVD suffers from poorer signal to noise ratios than UV-UV HB due to the shot to shot fluctuations in the "constant" probe signal; in the case of UV-UV HB these fluctuations are less important due to the presence of signal only when the probe laser is resonant with a transition.

2.3.4. Broadband Chirped Pulse Fourier Transform Microwave Spectrometer

The Zwier group recently acquired access to the broadband chirped pulse Fourier transform microwave (CP-FTMW) spectrometer formerly in Dr. Brian Dian's laboratory (Figure 2.6).[5] Since microwave spectroscopy requires that the a molecule contains a net permanent dipole moment, the CP-FTMW technique is a complementary tool in cases where molecules may be too difficult to ionize by R2PI or the molecules do not fluoresce well in LIF.

Molecules in the broadband CP-FTMW spectrometer are studied under isolated gas phase conditions after supersonic expansion from a Series 9 general valve (1 or 2 mm orifice diameter). A sophisticated electronics train is utilized to generate and detect microwave radiation. An arbitrary waveform generator (AWG, Tektronix AWG7101, 10 Gs/s) generates a linearly swept chirped pulse from 1.875 - 4.625 GHz. The chirped pulse is then filtered by a 5 GHz lowpass filter to remove higher harmonics (Lorch Microwave, 10LP-5000-S). The filtered waveform is subsequently amplified (Mini-Circuits, ZX60-613E-S+) to provide for a uniform power over the 1.875 - 4.625 GHz range. The amplified waveform is then directed into a quadrupler (Phase One Microwave, PS06-0161) resulting in a final waveform spanning 7.5 to 18.5 GHz. A step attenuator is placed after the quadrupler so that the amount of power can be controlled, and the output of the step attenuator is fed directly into the travelling wave tube amplifier (TWTA, Amplifier Research, 200 W, Model 200T8G18A). After the TWTA, the microwave radiation is output via the broadcasting horn such that the supersonically

cooled molecules become polarized and undergo free induction decay (FID). The receiving horn "hears" this molecular emission signal.

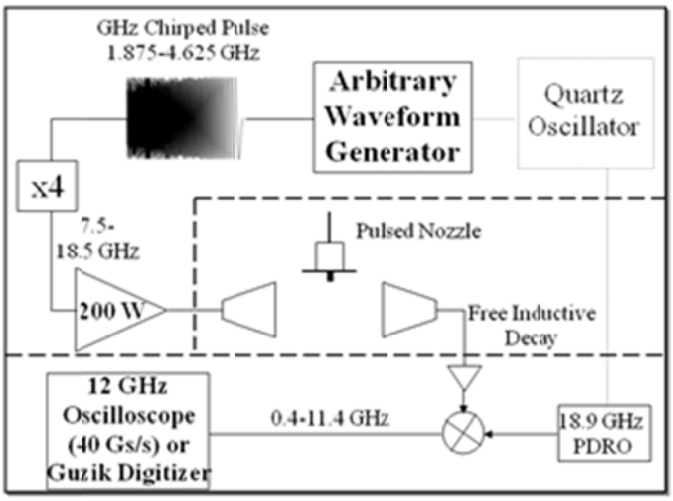

Figure 2.6. Schematic of the broadband chirped pulse Fourier transform microwave (CP-FTMW) spectrometer.

A p-i-n diode limiter (Aeroflex Signal and Control Solutions (formerly Advanced Control Components), ACLM-4619FC361K) is placed after the receiving horn and prior to the receiving electronics to protect them from being damaged by high power. A solid state switch (Advanced Technical Materials PNR S1517D) is placed after the p-i-n diode limiter for further protection, such that when the switch is "open" the there is a break in the circuit and no signal reaches the remainder of the receiving setup, and if the switch is "closed" then the signal reaches the detection electronics. In practice, when the solid state switch is open it cannot completely block out signals, but will greatly reduce their intensity. A low noise amplifier (Miteq AMF-6F-06001809-15-10P) is placed directly after the switch, and is used to amplify the molecular emission signals by about 40 dB. The molecular signals are then down-converted by mixing (Miteq TB0440LW1) with a filtered (Lorch Microwave 7CF7-18900-100-S) 18.9 GHz local oscillator (Microwave Dynamics PLO-2000-18.90) such that the signals can be monitored with a 12 GHz, 40 Gs/s oscilloscope (Tektronix TDS6124C Digital Storage Oscilloscope) in the traditional

setup. Di Zhang pioneered the setup of a fast digitizer (Guzik ADC6131-AVG) that has improved the ability of the Zwier group to average data with the multi-FID detection method, which allows for the collection of up to 20 FIDs in a single gas pulse. In the traditional detection scheme, an average of 10,000 FIDs (10 μs long) would take about 30 mins. With the new Guzik digitizer combined with the multi-chirp technique, the time to take 10,000 FIDs has been reduced to about 1 min! The timings of the AWG and pulsed general valve are controlled by a Masterclock (Thales Laser). A digital delay generator (Stanford Research Systems DG535) is triggered by the AWG, and it is used to control the times at which the 200 W TWTA is turned on/off and the time at which the switch is open/closed. A 10 MHz rubidium frequency standard (Stanford Research Systems FS725) is used to maintain phase stability in the experiment. The collected FIDs are post processed and Fourier transformed via Mathcad programs written by the Dian group. Molecular spectra are plotted and fit via JB95.

2.4. Computational Methods

Experimental spectra and computational chemistry share a symbiotic relationship. On one hand, the analyses of the acquired spectra throughout this dissertation are facilitated by computational chemistry. Computational methods help to determine the excited states, energy splittings, oscillator strengths, transition dipole moments, frequencies, etc. for the molecules under study, thereby aiding in the interpretation of their spectra. On the other hand, there are cases in which the experimental data collected serve as a benchmark for computational chemistry. The computational chemistry methods employed in the various dissertation projects will be detailed in each of the following chapters.

2.5. Project-Specific Techniques

Many experimental techniques used in this dissertation are specific to particular projects. As such, these project-specific techniques will be developed in the chapters that follow. In the chapter on the vibronic spectroscopy of the phenylcyanomethyl radical (Chapter 4), a description of the supersonic expansion discharge source will be provided alongside excited state lifetime and rotational band contour techniques. The photochemical reaction tube and UV population transfer methodologies will be presented in Chapter 5, which details (E)- and (Z)- phenylvinylnitrile spectroscopy and photochemistry.

2.6. References

1. Levy, D.H., Annu. Rev. Phys. Chem., 1980. **31**: p. 197-225.

2. Lubman, D.M., C.T. Rettner, and R.N. Zare, J. Phys. Chem., 1982. **86**: p. 1129-1135.

3. Fenn, J.B., Annu. Rev. Phys. Chem., 1996. **47**: p. 1-41.

4. Wiley, W.C. and I.H. McLaren, Rev. Sci. Instrum., 1955. **26** (12): p. 1150-1157.

5. Brown, G.G., et al., Rev. Sci. Instrum., 2008. **79** (5): p. 053103.

CHAPTER 3: VIBRONIC SPECTROSCOPY OF *PARA*-DIISOCYANOBENZENE

3.1. Introduction

Titan, one of the moons of Saturn, has a photochemically driven atmosphere rich in nitrogen and laced with methane (~3%).[1] The lack of oxygen in the atmosphere produces a reducing atmosphere that, under exposure to solar radiation, has produced a suite of organic hydrocarbons, nitriles, and isonitriles.[1, 2] Thought to be a model for early Earth's atmosphere, the chemical composition of Titan's atmosphere has been the subject of intense investigation via planetary missions and laboratory-based investigations seeking to determine the nature and altitude-dependent abundances of key constituents.[3] Sophisticated photochemical models are now in place that account for many of the smaller hydrocarbons and nitriles, but much work remains to be done in refining these models and extending them to include larger molecules, where much less is known about the pathways and chemical composition.[4-9]

The development of the large-molecule end of the model finds its motivation in part from the presence of a dense optical haze that shrouds Titan.[6-8] The chemical composition of this haze (commonly to referred to as 'tholins') and the atmospheric processes that produce it are known only in general terms.[10] A role is proposed for aromatic hydrocarbons, polyynes, and nitriles.[10] In this increased molecular size regime, structural isomers are more the norm than the exception. Since these isomers are likely to have unique reactivity, laboratory investigations of photochemistry relevant to Titan's atmosphere are increasingly turning attention to isomer-specific detection schemes.

Among the most elementary of structural isomers are nitriles (R-C≡N) and isonitriles (R-N≡C) that differ in the relative positions of the N and C atoms in the terminal diatom chain. When R is an alkyl group, the nitriles are lower in energy than

their isonitrile counterparts by about 80-100 kJ/mol.[11] At thermal equilibrium, the nitrile isomers should therefore dominate in abundance over their isonitrile counterparts.

However, there are reasons to wonder whether the isonitriles may also play a significant role in the chemical processes taking place in Titan's atmosphere. There is intense interest in establishing whether a "prebiotic" atmosphere like Titan's could produce molecules relevant to the development of biological processes, including key building blocks such as amides (R-NH-C(=O)-R) that are pervasive in proteins and nitrogen heteroaromatics (purines, pyrimidines) that are relevant to DNA. However, the nitrile group relegates the nitrogen atom at the terminus of the molecular structure, held firmly in place by an ultrastable C≡N triple bond, with subsequent reactions likely to simply carry along the nitrile substituent unscathed. The isonitrile group represents a first step in incorporation of the nitrogen atom into the chemical structure, and its destabilization makes it a more likely target for subsequent reactions that further transform the nitrogen atom's chemical properties. The unique properties of the isonitrile group are evident in the two resonance structures, which are formally zwitterionic and carbene in character.

The aromatic isonitriles are of particular interest because the pathways that produce the first aromatic ring often do not directly produce benzene, but substituted derivatives such as ethynylbenzene, cyanobenzene, and isocyanobenzene. For instance, the reaction of UV-excited cyanoacetylene (HC_3N) with 1,3-butadiene is known to produce cyanobenzene as one of its prominent products.[12] Since the barrier to isomerization in the electronic ground state is large (~150 kJ/mol),[13] the isonitrile isomers are stable relative to rearrangement once formed. This is especially true at the temperatures important in Titan's atmosphere (T<100 K).

As a result, it is worth exploring in greater depth how substitution of isocyano substituents onto an aromatic ring affects the electronic properties and the chemical and photochemical reactivity. In particular, as a precursor to photochemical studies, we present here a detailed study of the vibronic spectroscopy of a prototypical disubstituted

isocyano derivative, *para*-diisocyanobenzene (CN-Ph-NC, *p*DIB, Figure 3.1b), carried out under jet-cooled conditions in the gas phase. We combine the results of laser induced fluorescence (LIF), dispersed fluorescence (DFL), and resonant two-photon ionization (R2PI) spectroscopy to map out the Franck-Condon active and vibronically-induced transitions in the S_0-S_1 transitions of *p*DIB. When joined with the dicyano derivative *para*-dicyanobenzene (NC-Ph-CN, *p*DCB, Figure 3.1b) and the cyano/isocyano derivative *para*-isocyanobenzonitrile (CN-Ph-CN , *p*IBN, Figure 3.1b, characterized by Joseph Korn), an interesting triad of isomers is formed, with *p*DCB and *p*DIB having no dipole moment and D_{2h} ground state symmetry, while *p*IBN, with its incorporation of nitrile and isonitrile substituents on the same ring, having a calculated dipole moment of 0.795 Debye and C_{2v} symmetry.

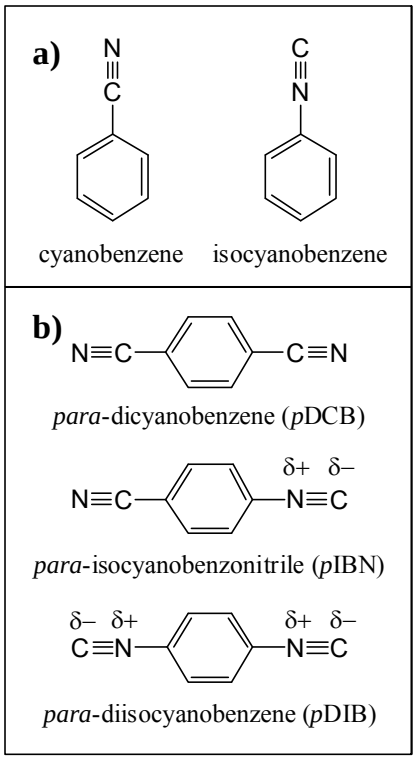

Figure 3.1. a) Structural isomers of nitrile/isonitrile mono-substituted benzenes: cyanobenzene and isocyanobenzene. b) Structure of *p*DIB (D_{2h} point group) that was specifically studied in this work, alongside the structures of *p*DCB (D_{2h} point group) and *p*IBN (C_{2v} point group).

In what follows, we will compare and contrast the spectroscopic results among *p*DIB and *p*DCB, along with the monosubstituted analogs cyanobenzene (benzonitrile, C_6H_5CN, PhCN) and isocyanobenzene (C_6H_5NC, PhNC) (Figure 3.1a). Furthermore, the ethynyl-substituted aromatics ethynylbenzene (phenylacetylene, $C_6H_5C{\equiv}CH$) and *para*-diethynylbenzene ($HC{\equiv}C\text{-}C_6H_4\text{-}C{\equiv}CH$) are isoelectronic with their cyano/isocyano counterparts, and are useful further points of comparison. A comparison to the spectroscopy of *p*IBN is beyond the scope of this work.

Of the monosubstituted nitrile/isonitrile benzene derivatives, Levy and coworkers[14] have studied the perturbative effects of the nitrile group on the electronic spectroscopy of benzene. Cyanobenzene has its S_0-S_1 origin as the most prominent transition in the excitation spectrum, with significant Franck-Condon activity in several of the ring modes typically active in the spectra of benzene derivatives.[15] Vibronically-induced transitions are present, but rather weak, involving b_2 symmetry fundamentals capable of vibronic coupling to the S_2 state, whose transition from the ground state carries significant oscillator strength. Furthermore, while early studies based on low-resolution dispersed fluorescence[14] were interpreted as showing the increasing presence of broad, red-shifted emission attributable to charge-transfer emission, later higher-resolution spectra by Sekiya and coworkers[16] showed this broadening to be simply unresolved sharp transitions, leading them to conclude that charge-transfer emission was not present in cyanobenzene.

Much less is known about its isonitrile counterpart, isocyanobenzene, PhNC. No jet-cooled spectrum is available for PhNC. However, there is an absorption cell study by Lombardi and coworkers that explores the spectroscopy of the isoelectronic series ethynylbenzene, cyanobenzene, and isocyanobenzene.[17] From their absorption cell studies, they found that the S_0-S_1 origin transition for isocyanobenzene was much weaker than in cyanobenzene, with vibronically induced transitions involving an in-plane bend of the isonitrile group dominating the spectrum. Indeed, in this sense, the isonitrile substituent acted more like the ethynyl substituent in ethynylbenzene[18] than the nitrile group in cyanobenzene.

We present near-complete assignments of the major transitions in *p*DIB, identifying the isonitrile bends as major sources of vibronic coupling between S_1 and S_2. The various contributors to the dipole-allowed and vibronically induced components of the spectrum are considered to deduce that changes in the S_0-S_1 oscillator strength are the major source of the spectroscopy observed, with vibronic coupling similar between *p*DIB and *p*DCB.

3.2. Methods

3.2.1. Experimental Methods

Commercially available *p*DIB (Sigma-Aldrich, 98%) was entrained in 3.8 bar backing pressure helium and expanded through a pinhole to generate a supersonic expansion via a Series 9 general valve (500-800 μm, LIF chamber) or a Jordan Valve (500 μm, R2PI chamber) to collisionally cool the molecules down to their zero-point vibrational energy level in the ground state. To obtain sufficient vapor pressure, the sample was heated between 60-80 ˚C in the general valve and between 45-55 ˚C in the Jordan valve. After cooling, the molecules were interrogated using laser spectroscopy via both fluorescence and ionization-based detection schemes.

In LIF, the frequency doubled output of a Nd:YAG pumped dye laser is used to promote the molecules to the excited state, and the total fluorescence from the molecules is collected and plotted as a function of excitation wavelength, thereby generating an excitation spectrum. The ionization based counterpart to LIF is R2PI. In R2PI, two photons are used to ionize a molecule of interest, and the total ion signal is collected as a function of excitation wavelength by a microchannel plate at the end of a time-of-flight mass spectrometer. In the case of the disubstituted benzene studied here, a first resonant photon (supplied from the frequency doubled output of a Nd:YAG pumped dye laser), and a second photon of higher energy (193 nm from a ArF excimer laser) were used to ionize the molecule due to the high ionization potential of the *p*DIB. When the ground

state information about the molecule was desired, DFL spectra were collected by fixing the excitation wavelength on a particular transition, and dispersing the total fluorescence into individual components across a grating on to a CCD or iCCD camera.

3.2.2. Computational Methods

Geometry optimizations and harmonic vibrational frequency calculations were carried out for the ground and first excited singlet state of *p*DIB using DFT and TD-DFT calculations that employed the B3LYP functional and 6-31+G(d) basis set. The Gaussian 09 suite of programs was used for this purpose.[19] Molecular orbitals were visualized using Chemcraft Software.[20]

3.3. Results and Analysis

3.3.1. Calculations

Figure 3.2 summarizes the key structural parameters of the optimized structures calculated for the S_0 and S_1 states of *p*DIB. The Merz-Kollman charges[21] associated with the isonitrile groups and phenyl carbons to which they are attached are included in the figure and were calculated at the DFT B3LYP/6-31+G(d) level of theory. As the zwitterion resonance structure would indicate, the isonitrile group has a charge distribution of +0.40 on the nitrogen and -0.42 on the carbon.

The optimized ground state geometry for *p*DIB has D_{2h} symmetry ($\tilde{X}(^1A_g)$), and its 36 normal modes consist of seven a_g, a single b_{1g}, four b_{2g}, six b_{3g}, two a_u, six b_{1u}, six b_{2u}, and four b_{3u} vibrations. Vibrations that involve the isonitrile groups in substantial ways come in g/u pairs with similar frequency, differing in the phase of oscillation of the atoms in the two substituents.

Vertical TD-DFT B3LYP/6-31+G(d) calculations predict a ππ* first excited state of *p*DIB, $\tilde{A}(^1B_{2u})$, with an allowed b-axis polarized electronic transition from S_0, but very

small oscillator strength (f=0.0012). As anticipated for phenyl derivatives, the optimized excited state geometry of *p*DIB is similar to that in the ground state, with expansion of the ring associated with the ππ* excitation, slight elongation of the NC bonds (by ~0.01 Å), and shortening by about 0.03 Å of the C(Ph)- N bonds (Figure 3.2).

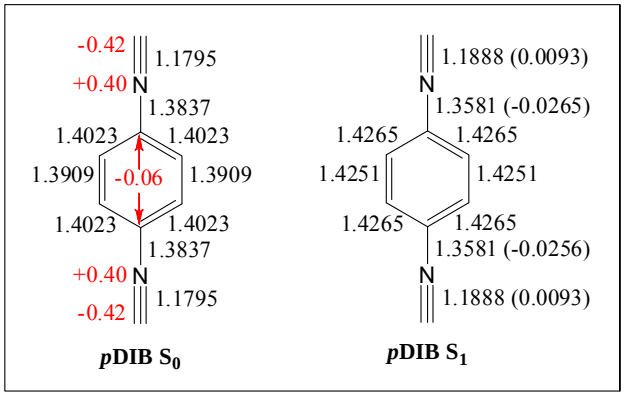

Figure 3.2. Optimized (DFT B3LYP/6-31+G(d)) ground and S_1 excited state geometries for *p*DIB. All bond lengths are in angstroms (Å), and the difference between excited and ground state bond lengths is indicated in parentheses for important bonds. Atomic charges are presented in red next to select atoms, and were computed using the Merz-Kollman scheme. See text for further details.

The vertical TD-DFT B3LYP/6-31+G(d) calculations for *p*DIB also predict the presence of a nearby second excited state of B_{1u} character that has a much larger oscillator strength (f = 0.533). Vertical splitting calculations place the S_2 state some 1,196 cm^{-1} above S_1 at the ground state geometry for *p*DIB. Attempts to optimize the S_2 state of *p*DIB produced structures with energies below the B_{2u} state, counter to experiment (see 3.3.2.). This swap in the energy ordering of S_1 and S_2 states via TD-DFT methods was found previously in the isoelectronic diethynyl substituted benzene.[22] Due to the vertical TD-DFT prediction of a nearby, high oscillator strength second excited state, Herzberg-Teller vibronic coupling of b_{3g} modes was carefully considered when assigning the vibronic spectrum.

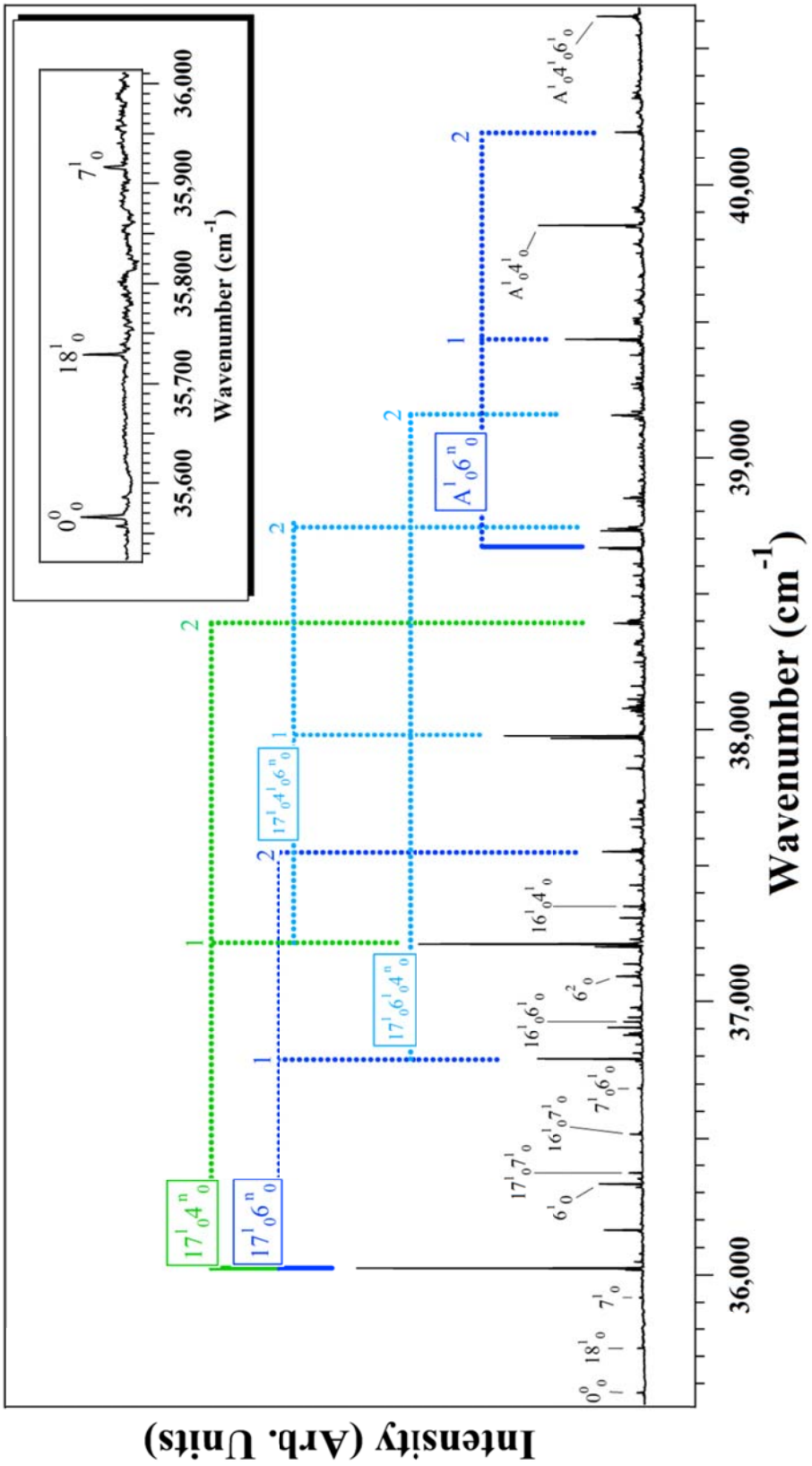

Figure 3.3. S_0-S_1 excitation spectrum of *para*-diisocyanobenzene. The S_0-S_1 origin is weak, and many transitions that carry intensity can be assigned to vibronically coupled b_{3g} modes ($\nu_{16\text{-}17}$) which serve as false origins upon which Franck-Condon activity of totally symmetric a_g modes ($\nu_{4,6\text{-}7}$) is built. The inset provides a zoom in of the S_0-S_1 origin region.

3.3.2. UV Spectroscopy of *para*-diisocyanobenzene (*p*DIB)

The LIF excitation spectrum of *p*DIB has been collected in the region spanning about 35,000 to 42,500 cm^{-1}. We have also recorded R2PI spectra over the 35,500 - 36,550 cm^{-1} region to verify that all the transitions observed in the LIF spectrum are due to the *p*DIB monomer. The LIF excitation spectrum from 35,500 - 40,650 cm^{-1} is shown in Figure 3.3.

The spectrum is notable relative to other phenyl derivatives in that vibronic activity spans this entire 5,000 cm^{-1} range, and remains relatively sharp and uncongested over much of this range. Assignments for the vibronic transitions are included in the figure, which are derived from a comparison with its analogs, the predictions of the calculations, and the DFL spectra, whose description follows. The labeled tie lines provide a framework for understanding the spectrum. The vibrational numbering follows Mulliken notation,[23] with the form of the normal modes involved in the assigned transitions shown in Figure 3.4. Table 3.1 compares the experimental and calculated frequencies for the assigned modes in the S_0 and S_1 states.

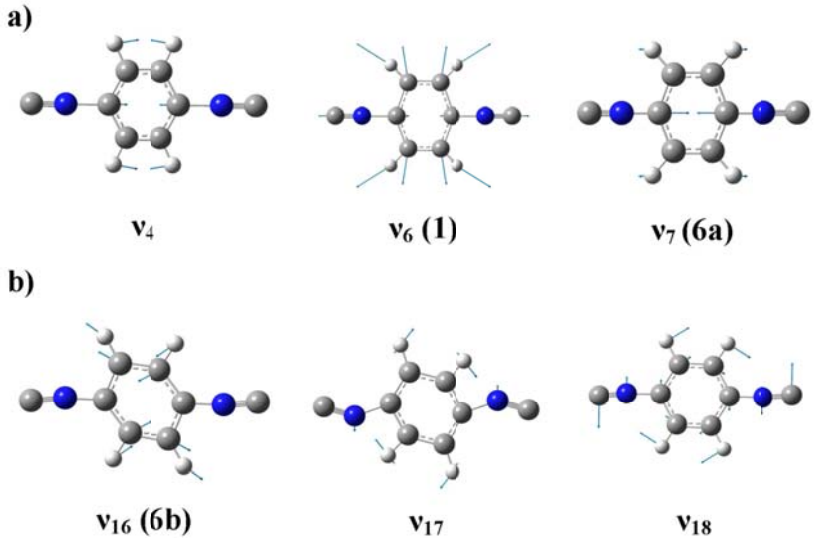

Figure 3.4. Pictorial representation of ground state normal modes of importance in the UV spectroscopy of *p*DIB. a) a_g modes involved in Franck-Condon activity, and b) b_{3g} modes involved in Herzberg-Teller coupling of S_1 to S_2. DFT (B3LYP/6-31+G(d)) was used to calculate the harmonic frequencies.

The S_0-S_1 origin is assigned to the very weak transition at 35,566 cm^{-1}, which is seen most clearly in the magnified view shown in the inset of Figure 3.3. Ultraviolet hole-burning (Figure 3.5a) and backing pressure (Figure 3.5b) studies indicated that this transition, and the other two bands +162 and +350 cm^{-1} above it were not hot bands, but had weak intensity relative to the dominant transition at 36,024 cm^{-1} (+458 cm^{-1}). In order to acquire hole-burn spectra, the hole-burn laser wavelength was fixed on the +458 cm^{-1} transition (marked with an asterisk in Figure 3.5a), and the difference signal was recorded while the probe laser was tuned through the region of interest. The transition at 35,566 cm^{-1} showed up clearly in the UV-UV HB spectrum, confirming it as the S_0-S_1 origin of *p*DIB, with the transition at +350 cm^{-1} attributed to vibronic activity. The transition at +162 cm^{-1} is not present in the R2PI spectrum, perhaps reflecting that the LIF spectrum (Figure 3.3) may be somewhat saturated. Despite its absence, the spectrum shown in Figure 3.5b, recorded at lower backing pressure in order to identify hot band transitions, showed that the transition at +162 cm^{-1} is a cold band, and thus should be identified as a weak transition built off the S_1 origin.

Table 3.1. Assignments for *para*-diisocyanobenzene vibrations

para-diisocyanobenzene (*p*DIB)					
		ground state frequencies		excited state frequencies	
mode	symmetry	expt.	calc.[a]	expt.	calc.[b]
4 (ν C-X)	a_g	1207	1235	1187	1233
6 (ring breath, 1)	a_g	826	834	766	780
7 (ring def., 6a)	a_g	393	394	350	341
16 (ring def., 6b)	b_{3g}	650	659	596	605
17 (β N≡C)	b_{3g}	501	515	458	418
18 (β C-X)	b_{3g}		183	162[c]	179

[a] Ground state calculations were performed using density functional theory with the B3LYP functional and a 6-31+G(d) basis set. Frequencies are unscaled.
[b] Excited state calculations were performed using time dependent density functional theory using the B3LYP functional and a 6-31+G(d) basis set. Frequencies are unscaled.
[c] Assignment is tentative.

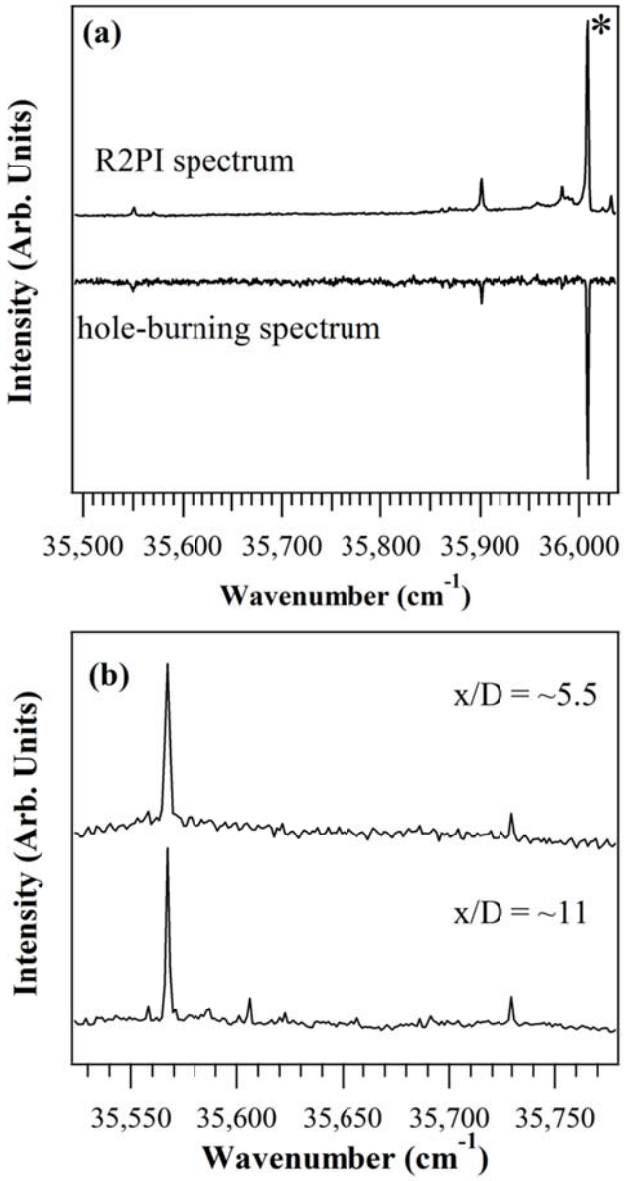

Figure 3.5. Confirmation of S_0-S_1 origin and vibronic bands of *p*DIB. (a) Cursory R2PI and UV-UV Hole-burning spectra of *p*DIB. (b) Hot band study of *p*DIB.

The most intense transition in the spectrum appears +458 cm^{-1} above the origin, assigned to 17^1_0, a b_{3g} fundamental involved in vibronic coupling with the S_2 state. Franck-Condon progressions involving the ν_4, ν_6, and ν_7 ring-deformation and ring-breathing modes build off of this fundamental. Transitions due to other b_{3g} fundamentals

with S_1 frequencies of 162 cm^{-1} (tentatively assigned to 18^1_0), 596 cm^{-1} (16^1_0) and 3,104 cm^{-1} (tentatively assigned as 13^1_0) serve as false origins for other progressions and combination bands involving $\nu_{4,6\text{-}7}$. Taken together, these account for the majority of the most intense transitions in the excitation spectrum.

To aid in the assignment of the excitation spectrum, DFL spectra of the origin and many other prominent transitions in the excitation spectrum were collected. When examining the DFL spectra, the presence of Herzberg-Teller vibronic coupling is unequivocally evident in the emission spectrum of the transition at +458 cm^{-1}, shown in Figure 3.6. This transition exhibits strong $\Delta v = \pm 1$ emission in a vibration of ground state frequency 501 cm^{-1}, and this emission pattern is characteristic to Herzberg-Teller vibronic coupling. Using the Mulliken notation scheme,[23] we assign the transition at +458 cm^{-1} as 17^1_0, a b_{3g} fundamental involving the in-plane bending of the isocyano substituents. The form of this normal mode is shown in Figure 3.4b. The prominent 17^1_2 (-1,002 cm^{-1}) and $17^1_1 16^0_1$ (-1,151 cm^{-1}) transitions in the +458 cm^{-1} DFL spectrum serve as false origins upon which other Franck-Condon vibronic activity involving a_g modes ($\nu_{4,6}$) is built.

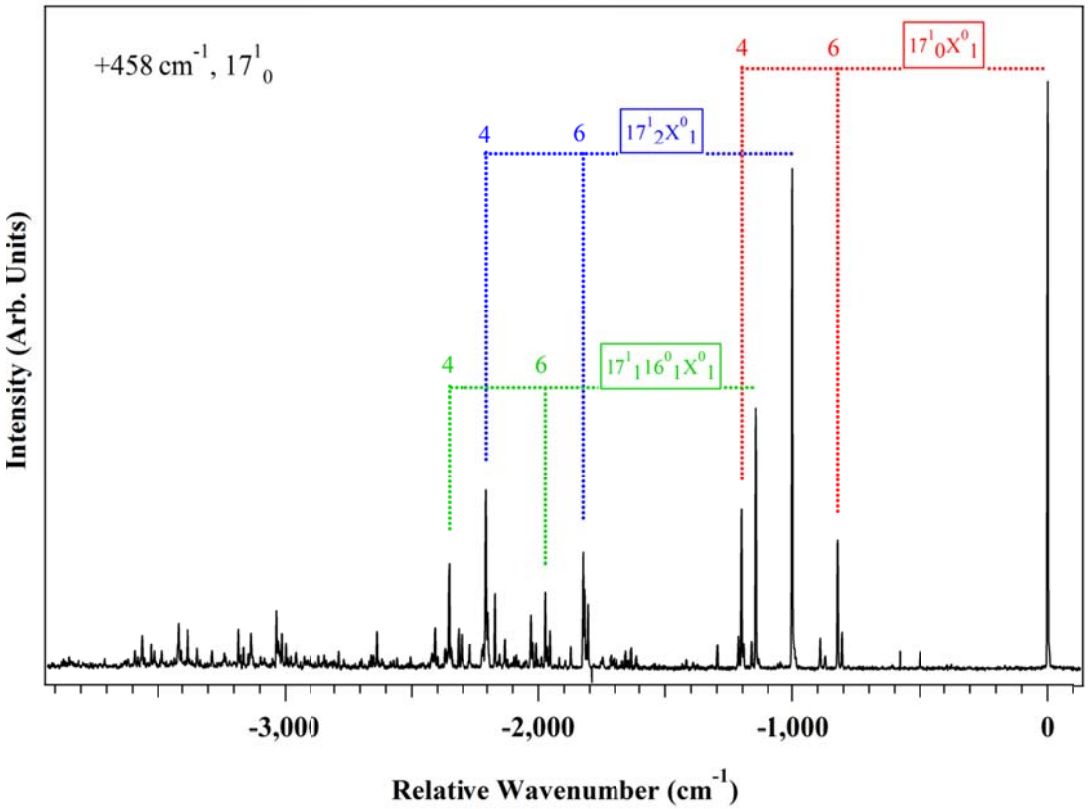

Figure 3.6. DFL spectrum of the +458 cm^{-1} (17^1_0) transition of *p*DIB. The 17^1_0, 17^1_2 and $17^1_1 16^0_1$ transitions serve as false origins upon which Franck-Condon activity is built. X is a totally symmetric mode; the identity of X is listed below each respective tie line.

After assigning these transitions in the DFL spectrum of the 17^1_0 level, the assignment of the DFL spectrum of the 35,566 cm^{-1} transition as the S_0-S_1 electronic origin, shown in Figure 3.7, follows readily. After subtraction of scattered light, resonance fluorescence is the strongest feature in the S_0-S_1 0^0_0 emission spectrum, indicating that the allowed character of the S_0-S_1 transition contributes to the emission, despite its weak character. In addition, as anticipated, the 17^0_1 and 16^0_1 transitions at -501 and -650 cm^{-1} that appear as a result of vibronic coupling, serve as false origins for Franck-Condon activity in $\nu_{4,6}$. The weak transition at -393 cm^{-1} is assigned as 7^0_1 involving the a_g fundamental equivalent to 6a in Varsanyi notation, the substituent-sensitive in-plane ring deformation.[24] The assignment of the ν_7 fundamental is confirmed

by the dispersed fluorescence of the +808 cm^{-1} transition (Figure 3.8) assigned as $17^1_0 7^1_0$, which shows a strong transition at -390 cm^{-1} due to $17^1_0 7^1_1$. The excited state frequency of ν_7 is 350 cm^{-1}. Interestingly, the dispersed fluorescence from the +458 cm^{-1} (17^1_0) transition shows more vibronic activity than the dispersed fluorescence spectrum of the S_0-S_1 origin. Since the strong $\Delta v_{17} = \pm 1$ transitions arise from vibronic coupling of S_1 ($v_{17} = 1$) with S_2, the larger Franck-Condon activity in combination bands built off these transitions must reflect a larger geometry change associated with the S_0-S_2 transition than S_0-S_1.

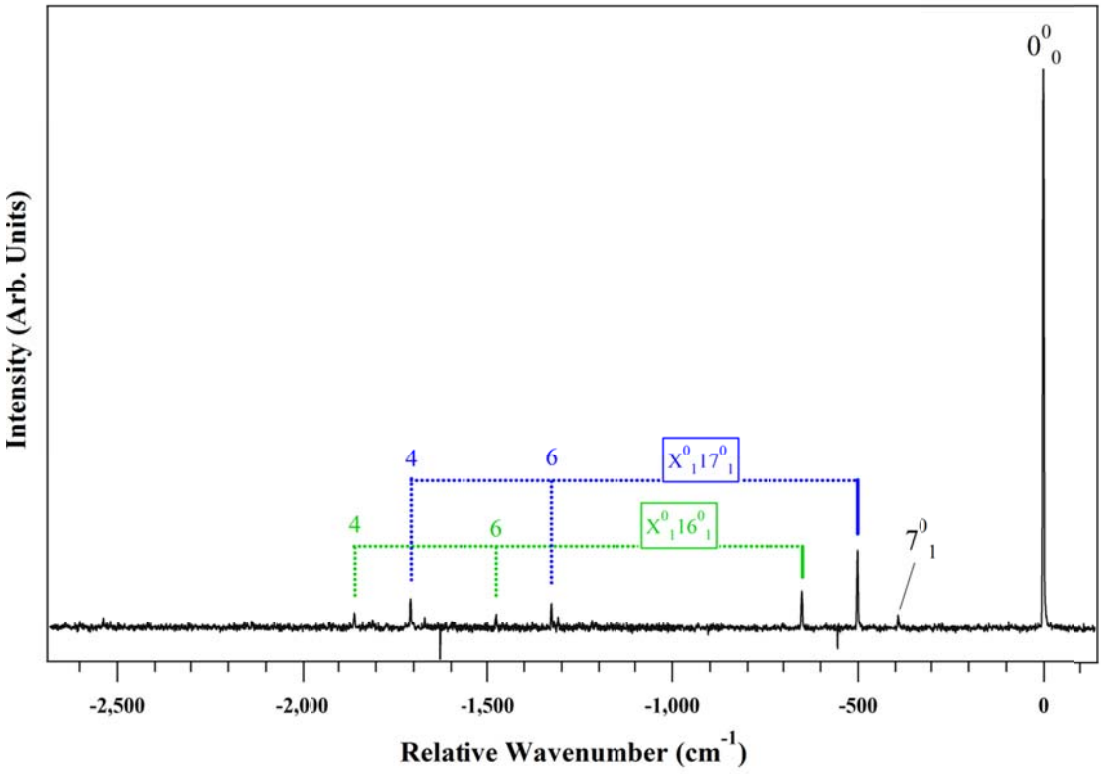

Figure 3.7. DFL spectrum of the S_0-S_1 origin transition of *p*DIB. The 16^0_1 and 17^0_1 transitions serve as false origins upon which Franck-Condon activity is built. X is used to denote a totally symmetric mode; the identity of X is listed below each respective tie line.

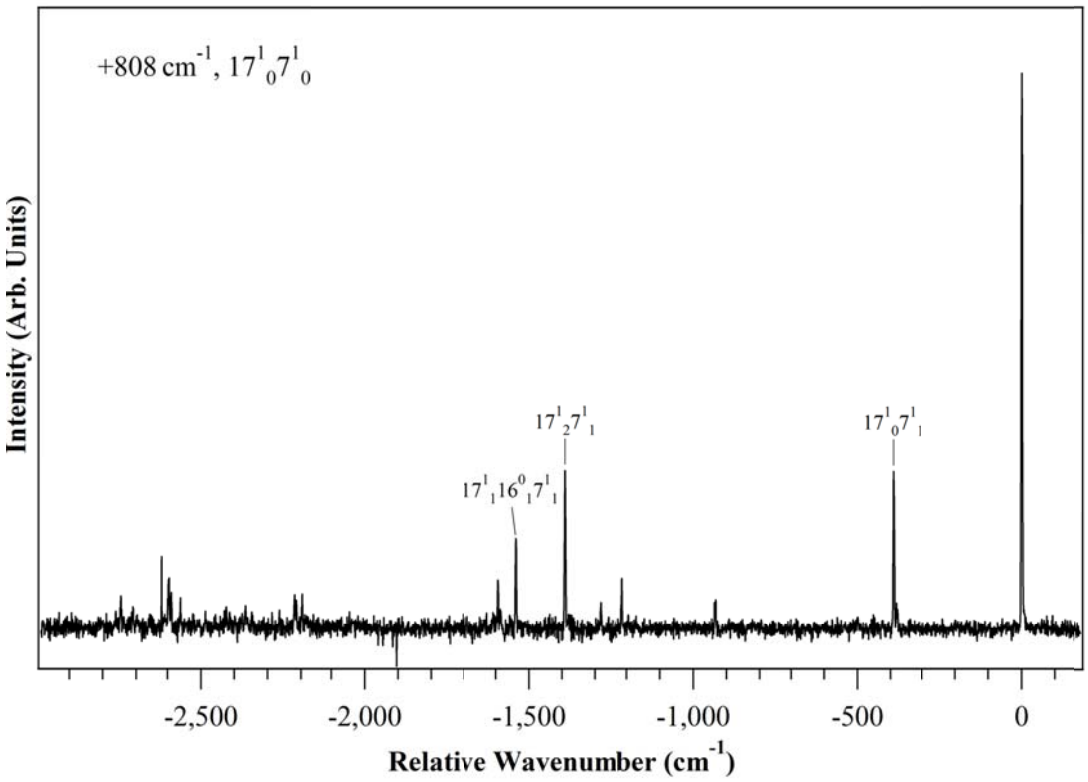

Figure 3.8. DFL spectrum of the +808 cm^{-1} transition in *p*DIB, $17^1_0 7^1_0$.

Figure 3.9 presents DFL spectra from a series of prominent transitions in the excitation spectrum, assigned to Herzberg-Teller induced transitions. For comparison, the spectrum of 17^1_0 is included (Figure 3.9a). The transition +596 cm^{-1} above the S_1 origin is assigned as 16^1_0, with a DFL spectrum (Figure 3.9b) closely analogous to that of the 17^1_0 transition. Vibronic coupling produces a false origin at -1,297 cm^{-1}, assigned to 16^1_2. The calculations predict $\nu_{16,}$ a second b_{3g} vibration analogous to 6b (Varsanyi), to have a frequency of 659/605 cm^{-1} (Table 3.1) in S_0/S_1. Note that, in addition to the pure $\Delta v = \pm 1$ transitions involving the mode 16 (16^1_0 and 16^1_2), the cross-sequence bands producing $16^1_1 17^0_1$ and $16^1_0 17^0_2$ transitions are also present, as they are with reversed intensity pattern from 17^1_0. This effect, analogous to Duschinsky mixing, was pointed out by Small as a necessary consequence when two or more modes of the same symmetry

are involved in vibronic coupling.[25] Further consideration of the consequences of such Duschinsky mixing for vibronic coupling will be taken up in the Discussion section.

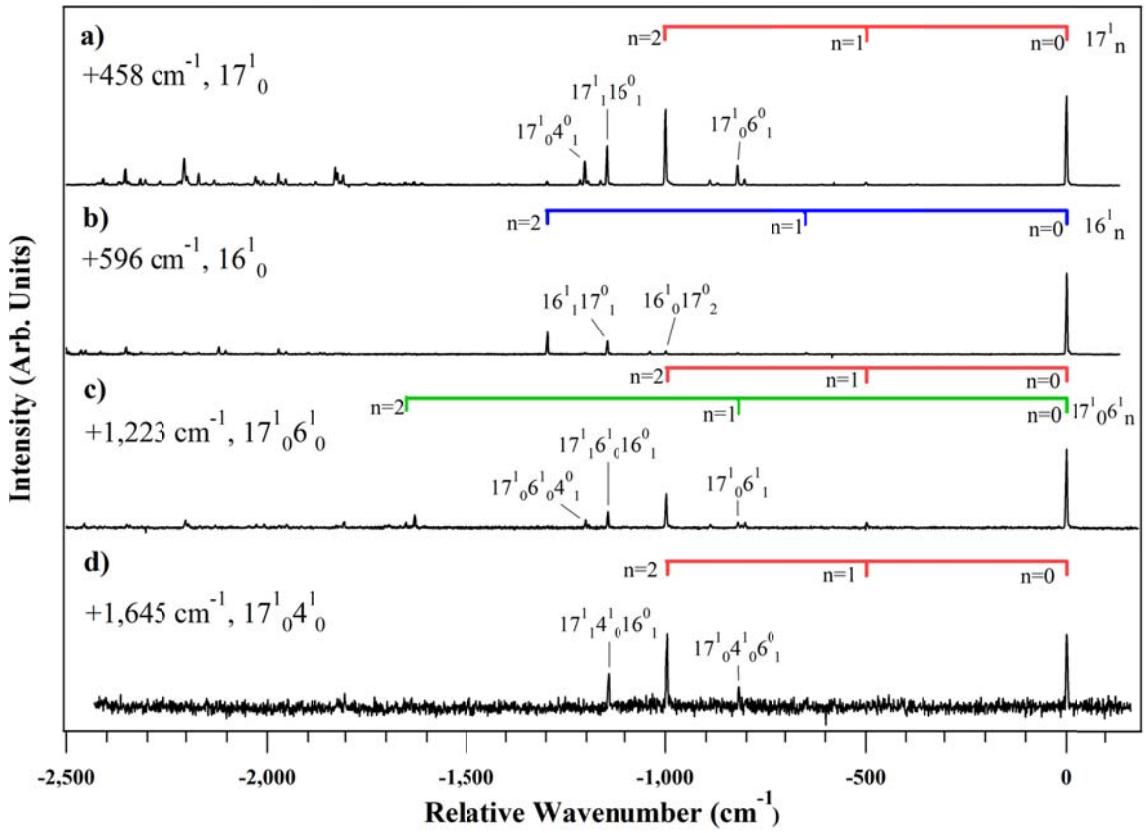

Figure 3.9. DFL spectra of the a) 17^1_0 b) 16^1_0 c) $17^1_0 6^1_0$ and d) $17^1_0 4^1_0$ transitions of *p*DIB. These transitions derive their oscillator strength in excitation from vibronic coupling. See text for further discussion.

The DFL spectra of the +1,223 cm^{-1} and +1,645 cm^{-1} transitions are shown in Figures 3.9c,d, respectively. Their marked similarity to the DFL of 17^1_0 is apparent. On the basis of this similarity, and the strong Franck-Condon activity involving ν_4 and ν_6 in other dispersed fluorescence spectra, the transitions at 1,223 cm^{-1} and 1,645 cm^{-1} are assigned to $17^1_0 6^1_0$ and $17^1_0 4^1_0$, respectively. Progressions in ν_6 (6^1_0 at 765 cm^{-1}, 6^2_0 at 1,528 cm^{-1}), and a $7^1_0 6^1_0$ combination band at +1,116 cm^{-1} are present in the excitation spectrum, consistent with these assignments. The $17^1_0 6^1_0$ dispersed emission (Figure

3.9c) is remarkably similar to 17^1_0 (Figure 3.9a) in the first 1,200 cm^{-1} of the spectrum, signaling the presence of one quantum in ν_{17}. A modulation in the intensity of the $17^1_0 6^1_n$ progression is also apparent, though the intensities of these transitions are likely affected by interference effects between the S_1 and S_2 components of the vibronically mixed excited state wavefunction. It is also possible that $17^1_0 6^1_0$ is in Fermi resonance with 15^1_0, another b_{3g} fundamental with predicted excited state frequency of 1,317 cm^{-1}, producing $\Delta v_{15} = \pm 1$ transitions that land in 15_0 or 15_2, the latter of which is beyond the endpoint of the spectrum. A more detailed investigation of this possibility awaits future work.

Finally, the assignment of the transition at 3,104 cm^{-1}, which serves as a false origin for Franck-Condon activity involving $\nu_{4,6}$ remains. We do not have a firm assignment for this transition, and as such, it is denoted as A^1_0 in Figure 3.3. A candidate assignment for the +3,104 cm^{-1} transition is the 13^1_0 b_{3g} fundamental for the following reasons: (i) theory predicts a C-H stretch fundamental near 3,233 cm^{-1}, which upon scaling by the typical scale factor at this level of theory[26] (0.9636), results in a predicted transition near 3,115 cm^{-1} and (ii) 3,104 cm^{-1} has progressions and combination bands involving $\nu_{4,6}$ built off of it much like the 16^1_0 and 17^1_0 b_{3g} fundamentals. However, there is little by way of precedence for vibronic coupling involving CH stretch modes in aromatics, nor does the mode have any significant component of CN bend to its motion, which is present in the other vibronically coupled b_{3g} modes ($\nu_{16\text{-}18}$).

Given the dominant role played by vibronic coupling of S_1 with S_2, and the large calculated oscillator strength for the S_0-S_2 transition, a search for the S_0-S_2 origin was carried out. We were guided in this search by the case of ethynylbenzene, where the S_2 state was located 41,955 cm^{-1}, 6,076 cm^{-1} above S_1.[18, 27] Figure 3.10a presents the LIF excitation spectrum of *p*DIB in the 41,320 - 42,550 cm^{-1} region, some 5,754 - 6,984 cm^{-1} above the S_1 origin. An intense set of closely-spaced transitions was detected, centered on 41,710 cm^{-1}, some 6,145 cm^{-1} above the S_1 origin. We tentatively assign this to the S_0-S_2 origin, due its large intensity and isolated frequency well above the last S_0-S_1 transition. The absence of an overlapping transition makes it difficult to accurately determine the intensity increase in Figure 3.10a with respect to Figure 3.3, though the

intensity of the transitions in Figure 3.10a is large, in keeping with the tentative association of this region with S_2.

The dispersed fluorescence spectrum from 6,145 cm^{-1} is shown in Figure 3.10b. No sharp transitions are observed, but instead a broad, red-shifted emission peaked ~ 9,500 cm^{-1} above the ground state zero-point level was observed. This red-shifted and broadened emission indicates that if the bands carrying the oscillator strength in absorption are the S_2 origin, then internal conversion to high-lying levels of S_1 must be occurring on a timescale fast compared to fluorescence. Given the large shift, which is about 3,500 cm^{-1} further than $\Delta v = 0$ Franck-Condon emission, there is a possible role for a charge transfer state at these high energies that red-shifts the emission, much as occurs in cyanobenzene.[14]

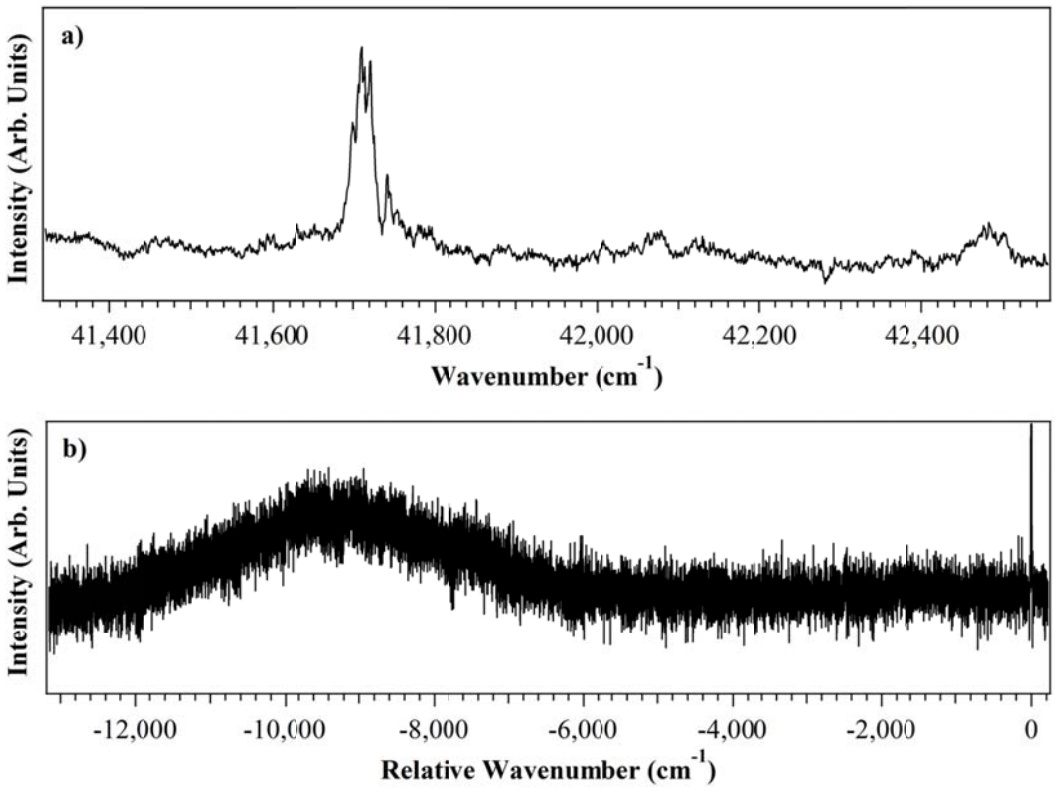

Figure 3.10. a) Tentative identification of S_0-S_2 region in *p*DIB, about 6,100 cm^{-1} above the S_0-S_1 origin transition and b) DFL spectrum of the + 6,145 cm^{-1} transition. Note the resonance fluorescence/scatter is off scale.

3.4. Discussion

3.4.1. Detection in Titan's Atmosphere

Since both aromatics and nitriles are known to be present in Titan's atmosphere, it is natural to postulate the presence of aromatic nitriles as other constituents in the atmosphere. Furthermore, the large barrier to isomerization of isonitriles to nitriles raises the prospect that isonitriles, once formed, would be stable relative to isomerization for long enough timescales to engage in unique reactions that could lead to incorporation of the nitrogen atom into structures of prebiotic relevance. Due to their large bond dipoles, isonitriles typically have large permanent dipole moments, making them detectable in the microwave or millimeter wave regions. However, when symmetry exists, as it would in *p*DCB or *p*DIB, microwave detection is not possible. All the aromatic nitriles included in the series PhCN, PhNC, *p*DCB, and *p*DIB have ultraviolet spectra with sharp vibronic structure that enable their isomer-specific detection. The present study has contributed towards the series of singly- and *para*-substituted nitriles and isonitriles, which have shown unique spectroscopic signatures.

The UV spectra are useful beyond their potential role as spectroscopic signatures, in that these same UV absorptions also can serve as the basis for selective photochemical reactions. In particular, one avenue open to the isonitriles is UV-induced isomerization to their nitrile counterparts. Since the UV absorption begins at about 35,000 cm^{-1} (286 nm), absorption of a UV photon places ~400 kJ/mol into the molecule. If internal conversion to the ground state is facile, it would produce a vibrationally excited ground state molecule with energy significantly in excess of the calculated barriers for isonitrile to nitrile interconversion (34 kcal/mol = 142 kJ/mol).[13] An energy level diagram for the photoisomerization is included in Figure 3.11. One would anticipate that each isomerization could occur independently along the separate hindered rotation coordinate for the NC group. It would be interesting to follow this photoisomerization from *p*DIB→*p*IBN→*p*DCB, a task left for future work. Here, we simply offer photoisomerization as a method for photoprocessing the isonitrile group to its nitrile

counterpart in Titan's atmosphere, anticipating that the lower energy of the nitrile isomer would favor its formation once on the ground state surface.

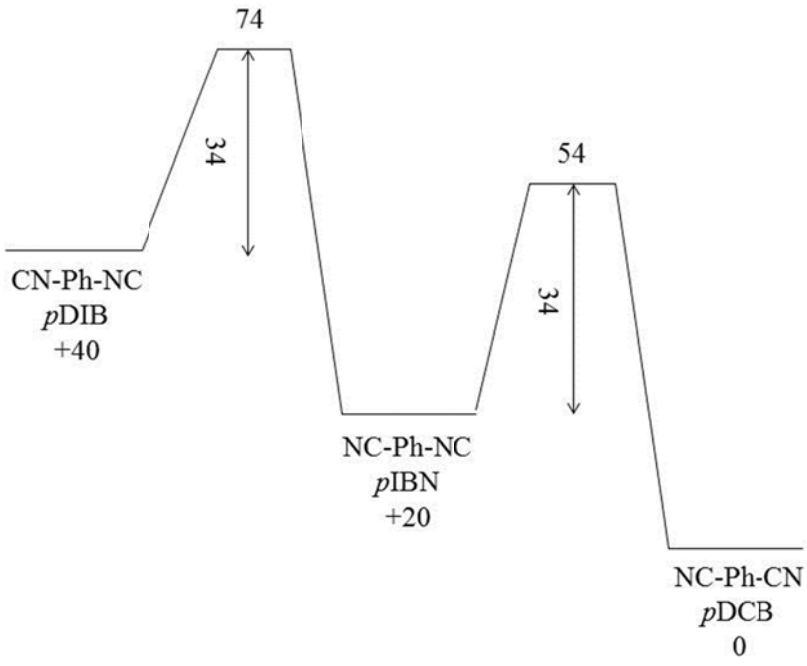

Figure 3.11. Isomerization surface from *p*DIB→*p*IBN→*p*DCB. Units are in kcal/mol, and the energetics were taken from Chapter 2 of "Isocyanide Chemistry: Applications in Synthesis and Material Science" edited by V. Nenajdenko.

Table 3.2. List of experimental S_0-S_1 origins for series, alongside calculated excited state properties.

Molecule	exptl S_0-S_1 0^0_0 (cm^{-1})[a]	calc[b] S_0-S_1 0^0_0 (cm^{-1})	ΔE_{12}[c] (cm^{-1})	f_{01}[c]	f_{02}[c]	dM_e/dQ_β[d]	$I(0^0_0)/I(\beta^1_0)$
Benzene	38,086[e] (0)	41,444	5,397	0	0	--	--
Monosubstituted Benzene							
Ethynylbenzene	35,879[f] (-2,207)	37,673	1,093	0.0003	0.325	--	0.30 (ν_{35} = 492 cm^{-1}), 2.0 (ν_{34} = 561 cm^{-1})
Cyanobenzene	36,516[g] (-1,570)	38,555	3,565	0.0081	0.226	1.28	4.7 (ν_{32} = 517 cm^{-1}), 45.0 (ν_{31} = ~577 cm^{-1})
Isocyanobenzene	36,706[h] (-1,380)	38,673	3,267	0.0014	0.247	1.59	~0.43 (ν_{32} = 452 cm^{-1}), ~0.75 (ν_{31} = 547 cm^{-1})
Disubstituted Benzene (para)							
para-diethynylbenzene[i]	34,255[j] (-3,831)	36,292	1,466	0.001	0.658	--	0.24 (ν_{20} = 492 cm^{-1})
para-dicyanobenzene	35,120[k] (-2,966)	36,427	1,516	0.0173	0.492	3.56	3.4 (ν_{17} = 519 cm^{-1})
para-diisocyanobenzene	35,566[l] (-2,520)	37,137	1,196	0.0012	0.533	5.1	0.03 (ν_{17} = 458 cm^{-1})

[a] Shift from benzene experimental S_0-S_1 origin is indicated in parentheses.
[b] This work. Optimization calculations were run using B3LYP/6-31+G(d) (TD-DFT).
[c] This work. Vertical calculations were run using B3LYP/6-31+G(d).
[d] Approximate induced transition dipole moment when displacing along the bending coordinate β in the ground state.
[e] Gruenloh, C.J., et al., J. Chem. Phys., 2000. 113(6): p. 2290-2303.
[f] Powers, D.E., J.B. Hopkins, and R.E. Smalley, J. Chem. Phys., 1981. 74(11): p. 5971-5976.
[g] Mordzinski, A., A.L. Sobolewski, and D.H. Levy, J. Phys. Chem. A, 1997. 101(44): p. 8221-8226.
[h] Muirhead, A.R., et al., J. Chem. Phys., 1972. 56(9): p. 4385-4393.
[i] Vertical/adiabatic B3LYP/6-31+G(d) calculations incorrectly predict S_1/S_2 order. S_1/S_2 have been swapped here to match experimental observations.
[j] Stearns, J.A. and T.S. Zwier, J. Phys. Chem. A, 2003. 107(49): p. 10717-10724.
[k] Fujita, K., et al., J. Phys. Chem., 1992. 96(26): p. 10693-10697.
[l] This work.

3.4.2. Comparison of Vibronic Spectroscopy of Isoelectronic Series

The present results on the vibronic spectroscopy of *p*DIB contribute to a series of studies of mono- and *para* di-substituted nitrile and isonitrile benzene derivatives.[14, 17, 28, 29] We are thus afforded an opportunity to compare and contrast the UV spectroscopy of the members of the series. Table 3.2 summarizes some of the key results. The table also includes data for the isoelectronic ethynyl-substituted analogs ethynylbenzene and *para*-diethynylbenzene.

Using the S_0-S_1 origin of benzene as the 'zero' for a relative wavenumber scale, the electronic frequency shifts of the S_0-S_1 electronic origins of cyanobenzene ($\Delta\nu$ = -1,570 cm^{-1}) and isocyanobenzene ($\Delta\nu$ = -1,380 cm^{-1}) are similar, with the shift for nitrile substitution about 10% greater than isonitrile. The analogous frequency shifts for the disubstituted pair fall into the order one would predict based on the monosubstituted pair, with $\Delta\nu$(*p*DCB)) > $\Delta\nu$(*p*DIB), and the magnitude of the shifts just less than twice that of the monosubstituted members.

*p*DIB has a sharp S_0-S_1 vibronic spectrum that extends over several thousand wavenumbers, with transitions having significant intensity out to almost 5,000 cm^{-1} above the S_1 origin. This vibronic structure contains transitions arising from Franck-Condon activity that reflect the change in geometry between ground and excited states and involving non-totally symmetric fundamentals that gain intensity from vibronic coupling between the S_1 and S_2 states.

One of the most striking aspects of the comparison between the four members of the nitrile/isonitrile series is the very different relative intensities of the dipole-allowed and Herzberg-Teller induced portions of the spectrum. Due to the high oscillator strength of the S_0-S_2 transitions in these molecules, even a small amount of vibronic coupling can mix in sufficient S_2 character to induce large transitions in the S_0-S_1 spectrum, as we see.

All four members of the nitrile/isonitrile series have in-plane NC/CN bending mode fundamentals of the right symmetry to vibronically couple S_1 and S_2 states, and in every case these bending modes are a principal means of doing so, with intensities larger than any other vibronically-induced transitions. The form of these bending modes for

*p*DIB is presented in Figure 3.12. Note that *p*DIB has a set of four in-plane bending fundamentals that come in two in-phase/out-of-phase pairs. In *p*DIB (Figure 3.12), the higher frequency pair involves bending the C(Ph)-N≡C angle ($\nu_{31}(b_{2u})$ = 453 cm^{-1}; $\nu_{17}(b_{3g})$ = 515 cm^{-1}), while the lower-frequency pair (not shown) involves bending the entire isonitrile group ($\nu_{32}(b_{2u})$ = 131 cm^{-1}, $\nu_{18}(b_{3g})$ = 183 cm^{-1}).

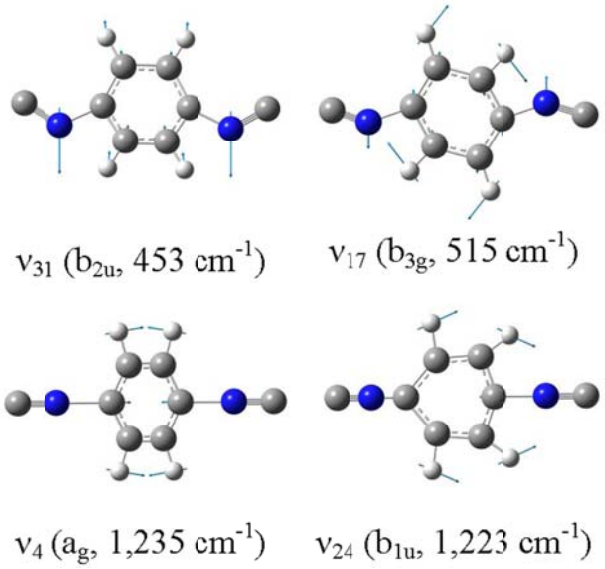

Figure 3.12. Form of the bending and C-X stretch modes of the isonitrile groups in *p*DIB.

Table 3.2 compares the intensity of the S_0-S_1 origin transition to that of the b_2/b_{3g} in-plane bending fundamental of the substituent(s), $I(0^0_0)/ I(\beta^1_0)$. Here we have chosen the generic label 'β' to signify the bending mode, with the mode number relevant to the particular molecule included in the table.

The singly- and disubstituted nitrile derivatives cyanobenzene[14] and *p*DCB [28] both have strong S_0-S_1 electronic origins, and vibronic structure dominated by Franck-Condon activity built off the electronic origin. This is what is observed for most aromatic derivatives with allowed S_0-S_1 transitions.[15] Franck-Condon activity involves several totally-symmetric in-plane ring modes (1, 6a, 12, 18 in Varsanyi notation) involving short progressions that reflect a modest geometry change associated with the $S_0(A_1)\rightarrow S_1(B_2)$

$\pi\pi^*$ transition. First-order vibronic coupling to the S_2 state occurs via non-totally symmetric fundamentals (b_2 in PhCN and b_{3g} in *p*DCB), and is comparatively weak. In particular, $I(0^0_0)/I(\beta^1_0) = 4.7$ and ~45 for PhCN and 3.4 for *p*DCB (Table 3.2).

By contrast, in *p*DIB, with its pair of *para*-substituted isonitrile groups, the S_0-S_1 electronic origin is very weak to the point of being barely discernible in the spectrum (Figure 3.3), with vibronic coupling accounting for the most intense transitions in the spectrum. In the Results and Analysis section, the most intense transition in the spectrum of *p*DIB, located 458 cm^{-1} above the origin, was assigned to the b_{3g} in-plane NC-bending fundamental 17^1_0 (Figure 3.6). As a result, the origin/β^1_0 intensity ratio is more than a factor of 110 times smaller (~0.03) than in PhCN and *p*DCB.

The final molecule, PhNC, which contains one isonitrile group, takes the middle ground, with intensity ratios $I(0^0_0)/I(\beta^1_0)$ of about 0.43 and 0.75 (Table 3.2). In the case of PhNC, studied by Muirhead et al., this ratio is estimated from the room temperature absorption spectrum shown in one of their figures.[17] Furthermore, the diethynyl analog *p*DEB also has a similar intensity ratio (Table 3.2), and so also appears to belong to this same sub-group.[22]

That this $I(0^0_0)/I(\beta^1_0)$ intensity ratio changes by more than a factor of 100 in the disubstituted nitrile/isonitrile (*p*DCB/*p*DIB) series is rather remarkable, given how similar the molecules in the series are in so many other ways. Within Herzberg-Teller theory,[30] the contribution to the transition moment due to vibronic coupling for a vibronic transition β^1_0 between S_0 and S_1 states due to vibronic coupling with S_2 is given by:

$$M_{01}^{HT} = M_{02} \cdot \left\langle \psi_2 \left| \frac{\partial H_{el}}{\partial Q_\beta} \right| \psi_1 \right\rangle \cdot \frac{\langle \chi^0_{v=0} | Q_\beta | \chi^1_{v=1} \rangle}{\Delta E_{12}} \qquad (1)$$

where M_{01} and M_{02} are electronic transition moments for the S_0-S_1 and S_0-S_2 transitions, respectively, ψ_1 and ψ_2 are the S_1 and S_2 excited state electronic wave functions, χ^0 and

χ^1 the vibrational wave functions in S_0 and S_1, and ΔE_{12} is the energy separation between the S_1 and S_2 states involved in vibronic coupling. If we define

$$\gamma_{12} = \left\langle \psi_2 \left| \frac{\partial H_{el}}{\partial Q_\beta} \right| \psi_1 \right\rangle \tag{2}$$

then the intensity ratio $I(0^0_0)$ / $I(\beta^1_0)$ is proportional to

$$\frac{I(0^0_0)}{I(\beta^1_0)} \propto \left[\frac{f_{01}}{f_{02}} \cdot \left(\frac{\Delta E_{12}}{\gamma_{12}} \right)^2 \right] \tag{3}$$

where we have subsumed the integral over χ into the constant of proportionality, recognizing that it accounts for the $\Delta v = \pm 1$ selection rules if the form of β is not changed significantly between S_0 and S_1 states. In eqn. (3) f_{01} and f_{02} are the oscillator strengths of the S_0-S_1 and S_0-S_2 transitions, respectively.

Equation (3) shows explicitly the terms that contribute to changes in the origin/β^1_0 intensity ratio, which are taken as representative of the ratio of dipole-allowed to vibronically induced contributions to the spectrum. This intensity ratio can vary due to (i) changes in the inherent oscillator strengths for the S_0-S_1 or S_0-S_2 transitions, (ii) the size of the Herzberg-Teller coupling matrix element between S_1 and S_2 (related to γ_{12}), and/or the energy separation ΔE_{12} between S_1 and S_2.

Table 3.2 includes calculated values for the factors contributing to the origin/β^1_0 intensity ratio from equation (3), for all members of the series. The vertical splittings ΔE_{12} are similar within the *p*DCB/*p*DIB series, as are the S_0-S_2 oscillator strengths. The column marked $\frac{\partial M_e}{\partial Q_\beta}$ lists calculated estimates of the relative transition moment derivatives along each of the indicated bending fundamentals. These were calculated by mapping out the transition moment vector $M_e(Q)$ for small displacements from equilibrium along each bending mode, and taking the slope at Q=0. As anticipated, the induced transition moment upon displacing along the bending coordinate is primarily along the 'a' axis, indicating mixing of S_1 (b-axis polarized) with S_2 (a-axis polarized).

However, these calculated transition moment derivatives in the disubstituted series differ by no more than a factor of two, and therefore cannot account for the greater than 100-fold increase in the $I(0^0_0)/I(\beta^1_0)$ intensity ratio.

What does change dramatically between *p*DIB and *p*DCB is the S_0-S_1 oscillator strength f_{01}. The variations in f_{01} identify the small intensity ratio $I(0^0_0)/I(\beta^1_0)$ in *p*DIB with the very small S_0-S_1 oscillator strength and correctly predicting *p*DCB largest, as observed experimentally. Thus, the dominant reason for the observed changes in the ratio of dipole-allowed to vibronically-induced components to the spectra is the changes in the oscillator strength in the S_0-S_1 transition.

In seeking an explanation for the dramatic changes in the inherent oscillator strengths of the S_0-S_1 transitions, TD-DFT calculations were carried out on the S_0-S_1 transitions of interest that identified the single-electron transitions responsible for them. As Table 3.3 shows, in all the S_0-S_1 transitions of interest, two single-electron transitions contribute. The molecular orbitals responsible for these transitions are shown in Figure 3.13 for *p*DIB, while the analogous orbitals for the whole set of molecules are included in Figures 3.14 and 3.15. As is apparent from Figure 3.13, the single electron transition between molecular orbitals 32 and 34 moves electron density from "off-axis" carbons onto the two isonitrile substituents, with transition dipole moment along the 'b' axis. For the 33→35 transition, the electron density moves in the opposite direction from the substituents to the off-axis carbons. Since the S_0-S_1 transition is a nearly equal mixture of 32→34 and 33→35 (with coefficients +0.519/-0.479), the resulting over-all TDM cancels nearly perfectly, resulting in a calculated oscillator strength very near zero (f_{01}(*p*DIB) = 0.0012), despite the fact that it is a dipole-allowed transition by symmetry. This is similar to the make-up calculated for *p*DEB (0.482/0.515), which also has an oscillator strength very near zero (f_{01} = 0.0010). In *p*DCB, the MOs are very similar in shape (Figure 3.15), but the contributions from the two one-electron transitions are no longer nearly equal, with values of +0.608/-0.358 in *p*DCB. The calculated oscillator strengths get increasingly large as this difference in the coefficients increases.

Table 3.3. Coefficients for single electron excitations in series of molecules

molecule	single electron excitations and coefficients in S_0-S_1 [a]	
ethynylbenzene	26 → 28	0.478
	27 → 29	0.518
cyanobenzene	26 → 28	0.578
	27 → 29	-0.404
isocyanobenzene	26 → 28	0.539
	27 → 29	-0.455
para-diethynylbenzene	32 → 34	0.482
	33 → 35	0.515
para-dicyanobenzene	32 → 34	0.608
	33 → 35	-0.358
para-diisocyanobenzene	32 → 34	0.519
	33 → 35	-0.479

[a] S_1 optimization calculations were run using B3LYP/6-31+G(d) (TD-DFT).

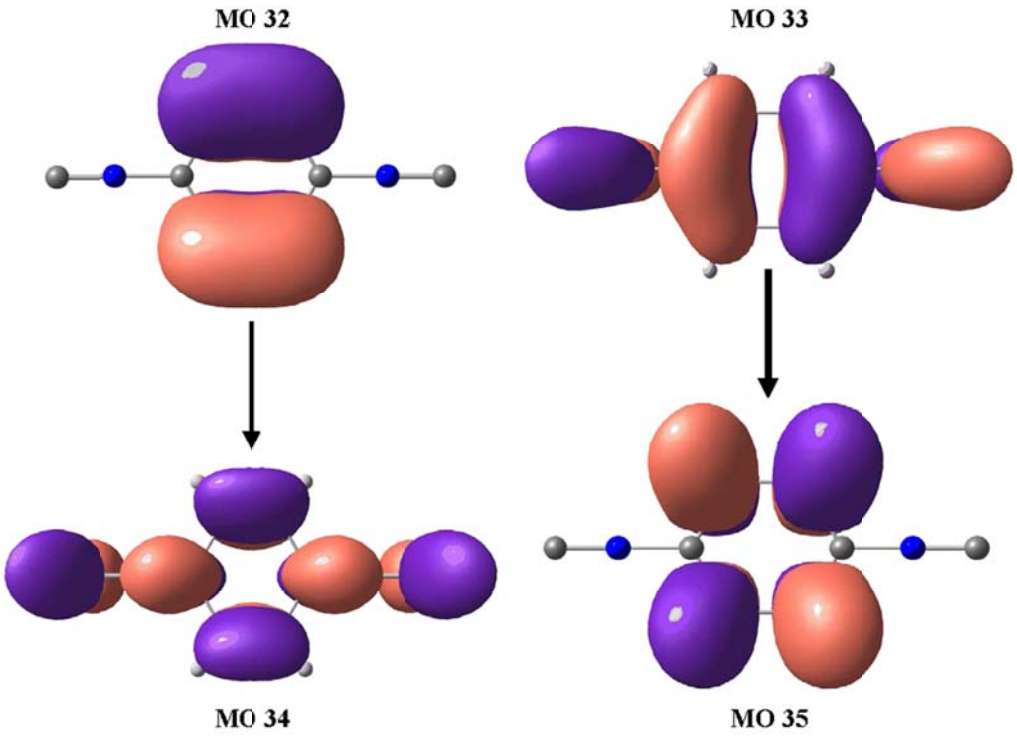

Figure 3.13. Pictorial representations of molecular orbitals (MOs) comprising S_0-S_1 of *p*DIB. Calculations were carried out at the DFT B3LYP/6-31+G(d) level of theory.

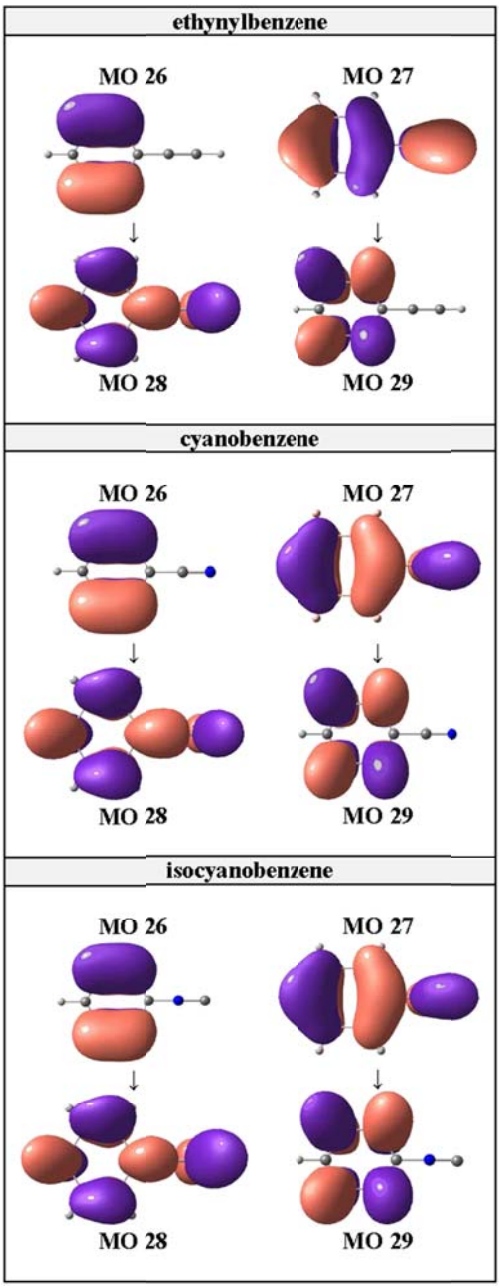

Figure 3.14. Pictorial representations of molecular orbitals (MOs) comprising S_0-S_1 transitions of the monosubstituted benzene species under investigation. The B3LYP functional and 6-31+G(d) basis set were used for calculations.

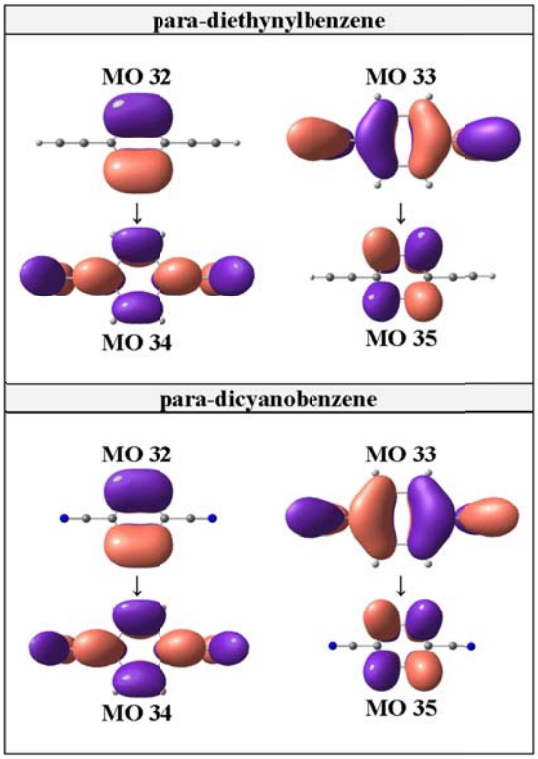

Figure 3.15. Pictorial representations of molecular orbitals (MOs) comprising S_0-S_1 transitions of the para disubstituted benzene species under investigation. The B3LYP functional and 6-31+G(d) basis set were used for calculations.

While differences in S_0-S_1 oscillator strength account for the qualitative change in the ratio of dipole-allowed to vibronically-induced portions of the spectrum, changes to f_{01} alone do not account quantitatively for the changes to the $I(0^0_0)/I(\beta^1_0)$ intensity ratios over the entire series. For instance, the calculated f_{01} oscillator strength for *p*DCB is a factor of 14 larger than that for *p*DIB, while the experimental intensity ratio $I(0^0_0)/I(\beta^1_0)$ jumps by more than a factor of 100. Similarly, the oscillator strength for f_{01} in PhCN is about a factor of 5 larger than in PhNC, but the experimental intensity ratio is about a factor of 11 or larger. Some of this discrepancy could arise from a sensitivity of the calculated oscillator strength in *p*DIB to the precise values of the mixing coefficients, since they nearly cancel one another.

3.4.3. Multi-mode Vibronic Coupling and Duschinsky Mixing

Up to this point, the focus has been on the bending fundamentals that dominate vibronic coupling between S_1 and S_2. These arguments, however, ignore the interference effects that can arise when multiple non-totally symmetric vibrations are involved in vibronic coupling. As Small has pointed out in his classic paper,[25] the presence of multiple non-totally symmetric modes vibronically coupled to the nearby S_2 state will necessarily result in Duschinsky mixing between the modes. This Duschinsky mixing is evident in $\nu_{16\text{-}17}$ in *p*DIB in the presence of cross-sequence bands in the DFL spectra from the $16^1_0/17^1_0$ levels of *p*DIB (Figure 3.9a,b). In addition to the 'pure' $\Delta v = +1$ transitions 16^1_2 (Figure 3.9b) and 17^1_2 (Figure 3.9a), transitions to the $16_1 17_1$ level are also clearly evident in both spectra.

Furthermore, Small also developed arguments that in the presence of multi-mode vibronic coupling, a lack of mirror symmetry should exist between the intensities of the vibronically-induced fundamentals in the excitation spectrum and origin DFL spectrum, due to interference effects.[25] These asymmetries are present in the spectra *p*DIB, sometimes in dramatic fashion. For example, modes 16 and 17 in *p*DIB are both b_{3g} symmetry and are engaged in vibronic coupling, with mode 16 a 6b-like in-plane ring distortion and mode 17 the isonitrile bend β. In excitation (Figure 3.3), their intensity ratio $\frac{I(17^1_0)}{I(16^1_0)} = 6.4$, while in emission from the S_1 origin (Figure 3.7), $\frac{I(17^0_1)}{I(16^0_1)} = 2.0$. Small[25] and Hollas and coworkers[31] have developed expressions for multi-mode vibronic coupling that show explicitly how these intensity asymmetries might arise. Their formulation shows that when $\nu_a < \nu_b$, $\frac{\mathrm{I}(a^1_0)}{\mathrm{I}(b^1_0)} > \frac{\mathrm{I}(a^0_1)}{\mathrm{I}(b^0_1)}$ when the vibronically-induced transition moment vectors m_a and m_b are antiparallel, and that the inequality of intensity ratios is reversed when m_a and m_b are parallel. Thus, the large asymmetry in the intensity ratios for these modes arises from their induced moments being anti-parallel, and similar in size, so that interference effects are large.

3.5. Conclusion

The vibronic excitation spectrum of *para*-diisocyanobenzene (*p*DIB) has been recorded under jet-cooled conditions over the 35,000 - 42,500 cm^{-1} region. *p*DIB is calculated to be 159 kJ/mol less stable than the *para*-dicyanobenzene isomer studied previously by Kaya and coworkers and Levy and coworkers.[28, 29] UV excitation of *p*DIB produces a sharp spectrum that reaches several thousand wavenumbers above the S_0-S_1 electronic origin. The major vibronic features in the spectrum were identified and assigned with the aid of dispersed fluorescence spectra, previous studies of analogous molecules, and the predictions of DFT calculations. The spectrum displays evidence for strong vibronic coupling of the S_1 state with S_2, mediated through bending mode fundamentals involving the isonitrile groups. Dispersed fluorescence spectra were recorded to aid in the assignments. In *p*DIB, the S_1 origin is extremely weak due to the near-equal but opposing contributions from two one-electron transitions, leading to a near-perfect cancellation of the S_0-S_1 transition dipole moment, despite its symmetry-allowed character ($\tilde{X}(A_{1g})\rightarrow\tilde{A}(B_{2u})$). The b_{3g} β_{NC} bending fundamental is responsible for much of the vibronic coupling to S_2, dominating the spectrum. Photoisomerization is postulated as a mechanism for conversion of *p*DIB to *p*DCB (via a *p*IBN intermediate), suggesting that, if *p*DIB is formed in Titan's atmosphere, it may interconvert by solar irradiation to the more stable nitrile counterparts.

3.6. Future Work

The characterization of *p*DIB in this work and the characterization of *p*IBN by Joseph Korn provides the necessary foundation to carry out experiments that test the *p*DIB→*p*IBN→*p*DCB photoisomerization pathway, which can be carried out utilizing ultraviolet population transfer spectroscopy.[32] In addition to these photochemistry experiments, the study of the molecules *para*-ethynylbenzonitrile ($HC\equiv C\text{-}C_6H_4\text{-}C\equiv N$, *p*EBN) and *para*-ethynylisocyanobenzene ($HC\equiv C\text{-}C_6H_4\text{-}N\equiv C$, *p*EIB) would round out the spectroscopic investigation of the isoelectronic series, in which *p*DIB, *p*IBN, *p*DEB, *p*DCB have been studied.

3.7. References

1. Raulin, F., et al., Chem. Soc. Rev., 2012. **41** (16): p. 5380-5393.
2. Moreno, R., et al., A&A, 2011. **536**: p. L12.
3. Waite, J.H., et al., Science, 2007. **316** (5826): p. 870-875.
4. Wilson, E.H. and S.K. Atreya, Journal of Geophysical Research-Planets, 2004. **109** (E6).
5. Yung, Y.L., Icarus, 1987. **72**: p. 468-472.
6. Krasnopolsky, V.A., Icarus, 2009. **201** (1): p. 226-256.
7. Krasnopolsky, V.A., Planetary and Space Science, 2010. **58** (12): p. 1507-1515.
8. Krasnopolsky, V.A., Planetary and Space Science, 2012. **73** (1): p. 318-326.
9. Banaszkiewicz, M., et al., Icarus, 2000. **147** (2): p. 386-404.
10. Cable, M.L., et al., Chem. Rev., 2012. **112** (3): p. 1882-1909.
11. Koizumi, H. and T. Baer, J. Phys. Chem. A, 2004. **108** (28): p. 5956-5961.
12. Faraday Discussions, 2010. **147** (0): p. 83-102.
13. Mironov, M.A., *General Aspects of Isocyanide Reactivity*, in *Isocyanide Chemistry*, 2012, Wiley-VCH Verlag GmbH & Co. KGaA. p. 35-73.
14. Mordzinski, A., A.L. Sobolewski, and D.H. Levy, J. Phys. Chem. A, 1997. **101** (44): p. 8221-8226.
15. Hickman, C.G., J.R. Gascooke, and W.D. Lawrance, J. Chem. Phys., 1996. **104** (13): p. 4887-4901.

16. Sakota, K., et al., Chemical Physics Letters, 2000. **322** (5): p. 407-411.

17. Muirhead, A.R., et al., J. Chem. Phys., 1972. **56** (9): p. 4385-4393.

18. Powers, D.E., J.B. Hopkins, and R.E. Smalley, J. Chem. Phys., 1981. **74** (11): p. 5971-5976.

19. Frisch, M.J.T., G. W.; Schlegel, H. B.; Scuseria, G. E.; Robb, M. A.; Cheeseman, J. R.; Scalmani, G.; Barone, V.; Mennucci, B.; Petersson, G. A.; et al.

20. Zhurko, G.A. *Chemcraft*. http://www.chemcraftprog.com; 1.6:[Available from: http://www.chemcraftprog.com.

21. Singh, U.C. and P.A. Kollman, J. Comput. Chem., 1984. **5** (2): p. 129-145.

22. Stearns, J.A. and T.S. Zwier, J. Phys. Chem. A, 2003. **107** (49): p. 10717-10724.

23. Mulliken, R.S., J. Chem. Phys., 1955. **23** (11): p. 1997-2011.

24. Varsanyi, G., *Assignments for Vibrational Spectra of 700 Benzene Derivatives*1974, New York: Wiley.

25. Small, G.J., J. Chem. Phys., 1971. **54** (8): p. 3300-&.

26. Merrick, J.P., D. Moran, and L. Radom, J. Phys. Chem. A, 2007. **111** (45): p. 11683-11700.

27. Leopold, D.G., et al., J. Chem. Phys., 1981. **75** (10): p. 4758-4769.

28. Fujita, K., et al., J. Phys. Chem., 1992. **96** (26): p. 10693-10697.

29. Jiang, S. and D.H. Levy, J. Phys. Chem. A, 2002. **106** (37): p. 8590-8598.

30. Struve, W.S., *Fundamentals of Molecular Spectroscopy*1989: Wiley. 245-248.

31. Bacon, A.R. and J.M. Hollas, Chemical Physics Letters, 1985. **120** (4–5): p. 477-480.

32. Newby, J.J., et al., J. Am. Chem. Soc., 2010. **132** (5): p. 1611-1620.

CHAPTER 4: SPECTROSCOPY AND IONIZATION THRESHOLD FOR THE DOUBLY RESONANCE-STABILIZED PHENYLCYANOMETHYL RADICAL

4.1. Introduction

Titan, the largest moon of Saturn, is regarded as a modern "laboratory" for the study of primordial Earth.[1, 2] Titan's atmosphere is dominantly comprised of molecular nitrogen, making it similar to the atmosphere of early Earth.[3, 4] A couple percent methane, and fractional percentages of CO, CO_2, HCN, C_2H_2, HC_3N, and other small organics are also present in Titan's atmosphere.[1, 3] With a methane cycle analogous to the water cycle on Earth,[1] and a reducing atmosphere similar to that of prebiotic Earth,[4, 5] Titan has many of the components that are deemed necessary for the onset of life on prebiotic Earth. As such, Titan's atmosphere is arguably well-suited for biologically pertinent chemistry.

Titan's prebiotic chemistry is thought to be endogenous in nature.[5] This chemistry is primarily initiated via the photochemistry of molecular nitrogen and methane and secondarily through bombardment of these gases with energetic particles, to produce ions and (open and closed shell) neutrals.[1] Reactions between these ions and neutrals lead to the formation of small organic compounds up to benzene, and ultimately tholins.[1, 6]

Of the neutral pathways of reaction, resonance-stabilized radicals (RSRs) are likely to be key intermediates in the formation of larger molecules.[7-9] Delocalization of the radical site into the π cloud of a neighboring conjugated functional group leads to longer lifetimes due to resonance stabilization. These longer lifetimes of the RSRs allow them to build up in concentration, and radical-radical recombination reactions with itself or other RSRs serve as the principal pathways for removal. As an example, the recombination of two resonance-stabilized propargyl radicals (C_3H_3) is among the

postulated pathways for benzene formation.[10-12] These results attest to the potentially important role of RSRs in the formation of larger molecules in the atmosphere.

Due to the presence of nitrile species on Titan,[1] nitrile and isonitrile RSRs could be especially important in the chemistry of Titan's atmosphere, leading to the formation of complex nitrogen-containing compounds and ultimately tholins.[13] One such RSR is the phenylcyanomethyl radical (PCM), whose structure is shown in Figure 4.1.

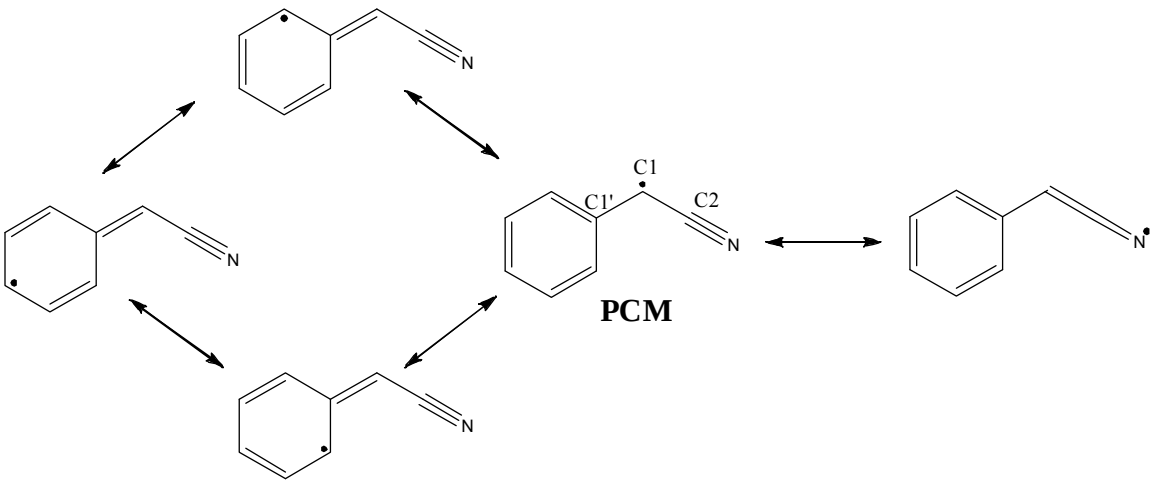

Figure 4.1. Structure of the phenylcyanomethyl radical (PCM). The radical site is doubly resonance-stabilized due to the ability to conjugate to the aromatic ring and nitrile group.

The phenylcyanomethyl radical is doubly resonance-stabilized through its conjugation to the neighboring phenyl ring and cyano functional groups on either side of the primary radical site on the bridging CH group. The PCM radical is the nitrogen-containing analog of the 1-phenylpropargyl radical (1PPR) that has been extensively studied by the Schmidt, Kable, and Gerber groups.[7, 8, 14, 15] In the body of 1PPR work, the ground (D_0) and first excited (D_1) doublet electronic states were characterized, and the excited state lifetime in D_1 and the ionization potential were determined. The D_0-D_1 origin transition of 1PPR lies in the visible region (21,007 cm^{-1}), with vibronic structure extending above the origin for 1,300 cm^{-1}. Due to its status as a doubly resonance-

stabilized radical, 1PPR is thought to be an important intermediate species in combustion chemistry, and to potentially play a role as intermediate in the formation of higher molecular weight species in the interstellar medium. This 1PPR work served as inspiration for the present study of the PCM radical as its nitrile analog, with principal application to Titan's atmosphere, where nitrile chemistry is pervasive.

In this work, we present the first detection of the nitrile analog of 1PPR, PCM. Spectroscopic characterization was achieved in the D_0-D_1 region, which like 1PPR also appears in the visible region. In a fashion similar to 1PPR, PCM may also serve as an important intermediate in the formation of nitrogen-containing heterocycles and larger molecules. Investigating the chemical intermediates and pathways leading to the incorporation of nitrogen into ring structures will help bring the community one step closer to understanding the processes leading toward biologically relevant molecules, many of which are composed of nitrogen heteroaromatics.

4.2. Methods

4.2.1. Experimental Methods

Studies on the phenylcyanomethyl radical were carried out in a vacuum chamber that has been described in detail elsewhere.[10] Benzyl cyanide was purchased at 98% purity from Sigma-Aldrich, and used as a precursor for the generation of the phenylcyanomethyl radical. After entraining benzyl cyanide into a total of 2.0 bar argon backing gas, the sample is introduced into a discharge tube (2 mm inner diameter, 17 mm long) via an R. M. Jordan pulsed valve. Gas pulses approximately 60 μs in duration at a total flow of 0.35 sccm are typically used. At the end of the discharge tube, an electrical discharge created between two electrodes (± 500 V) is timed to intersect a dense portion of the gas pulse such that the phenylcyanomethyl radical is generated, and cooled to its zero-point vibrational energy level in the ground state via supersonic expansion into the vacuum chamber.

Two-color resonant two-photon ionization (2C-R2PI) spectroscopy was used to ionize the phenylcyanomethyl radical prior to traversal in a Wiley-McLaren[16] type time-of-flight mass spectrometer for mass-selective detection. Mass-selective detection is particularly important in the case of discharge-based studies, where multiple absorbing species may be generated. As the name 2C-R2PI implies, two photons of different energy are used to ionize the species under study. The fundamental of a Nd:YAG pumped dye laser (visible) was used as a first photon to tune through the D_0-D_1 excitation spectrum of the phenylcyanomethyl radical; a second photon of 193 nm was used to ionize the phenylcyanomethyl radical out of its D_1 excited state. By collecting the integrated ion signal at m/z = 117 as a function of wavelength, the excitation spectrum was obtained. A wavemeter was used to obtain the vacuum corrected wavelengths of transitions in the excitation spectrum.

Photoionization efficiency scans were used to determine the ionization potential (IP) of the phenylcyanomethyl radical. The wavelength of the visible photon was fixed on the D_0-D_1 transition, and the wavelength of the ionizing photon was tuned until there was an onset of ionization signal. The sum of energy of the resonant photon and the ionizing photon at the onset of ion signal provides the ionization potential for the radical.

Rotational band contours (RBCs) were also collected to determine the direction of the transition dipole moment of the molecule under study. The RBCs were collected by obtaining a high resolution 2C-R2PI spectrum over a vibronic transition of interest. The dye laser used for the D_0-D_1 step has a resolution in the visible of 0.06 cm^{-1}, a resolution sufficient to obtain the shape of the rotational band contour, but insufficient to resolve individual rovibronic transitions.

The excited state lifetime was determined by monitoring the ion signal as a function of the temporal delay between the visible and ionizing photon. A fit of the ion signal decay profile to an exponential function provides the lifetime of the D_1 vibronic levels interrogated.

Dispersed fluorescence (DFL) data were collected in the laboratory of our collaborator, Dr. Timothy Schmidt at the University of New South Wales in Australia. His data will not be presented in this chapter, but will be available in a forthcoming

publication. The dispersed fluorescence data provide valuable insights in understanding the spectroscopy of the phenylcyanomethyl radical, and will be mentioned in summarized form in arguments presented in the Results and Discussion sections of this chapter.

4.2.2. Computational Methods

Ab initio calculations were carried out using Gaussian 09.[17] Ground state density functional theory (DFT) and excited state time-dependent density functional theory (TD-DFT) optimizations and harmonic frequency calculations were carried out using the unrestricted B3LYP functional[18] with the 6-311+G(d,p) basis set. Computed frequencies were used to aid in the process of assigning transitions in the excited state spectrum. Ionization potentials were calculated by taking the zero-point corrected energy difference between the S_0 radical ion and D_0 ground state of the radical, using the unrestricted B3LYP functional with the 6-31+G(d) basis set. The ROCBS-QB3 method[19] was used to predict the thermochemical data for radical stabilization energy (RSE) calculations. In a comparison of various computational methods for thermochemistry, ROCBS-QB3 is considered reliable and computationally efficient.[20]

The presence of two nearby excited electronic states D_1 and D_2 for the phenylcyanomethyl radical presents an interesting challenge for theory, particularly in predicting the correct ordering and properties between the two excited states. Our collaborators Professor Lyudmila Slipchenko (Purdue University) and Dr. Ben Nebgen are conducting an extensive on-going investigation of the theory associated with the phenylcyanomethyl radical, to confirm the state ordering and properties for the radical, as well as for additional reasons that will be addressed in the Discussion portion of this chapter. For this chapter, the unrestricted DFT B3LYP/6-311+G(d,p) and unrestricted TD-DFT B3LYP/6-311+G(d,p) calculation results will be used as a theoretical guide against which experimental results can be compared.

4.3. Results

4.3.1. 2C-R2PI Spectrum

Figure 4.2 presents the 2C-R2PI spectrum for the phenylcyanomethyl radical, in relative wavenumbers. The $D_1(^2A'')\leftarrow D_0(^2A'')$ origin transition for the phenylcyanomethyl radical is located at 21,402 cm^{-1}. Theory (UB3LYP/6-311+G(d,p)) predicts the first excited state of the phenylcyanomethyl radical to be a $\pi^*\leftarrow\pi$ transition in which the phenylcyanomethyl radical becomes more cumulenic in structure upon excitation. Both the D_0 ground state and D_1 excited state of the phenylcyanomethyl radical are predicted to be planar in geometry, therefore the radical belongs to the C_s point group in both the D_0 and D_1 states. Of PCM's 39 normal modes, 27 are totally symmetric, in-plane modes of a' symmetry, while the remaining 12 are out-of-plane modes of a" symmetry. If C_s symmetry is retained in the D_0 and D_1 states, Franck-Condon selection rules dictate that all in-plane vibrations can appear as fundamentals ($\Delta v_{ip} = \pm1, \pm2, \ldots$ allowed), while out-of-plane transitions can only appear as either combination bands or even overtones ($\Delta v_{oop} = \pm2, \pm4, \ldots$ allowed) for transitions arising out of the zero-point level in D_0. Because the electronic structure of the phenylcyanomethyl radical is closely similar to that of 1-phenylpropargyl radical,[7, 8] we use the assignments of the latter as a guide in the analysis that follows, alongside results from the DFT and TD-DFT UB3LYP/6-311+G(d,p) theoretical calculations. Modes are labeled using Mulliken[21] notation, with the Varsanyi[22] notation in parentheses wherever a close analog exists.

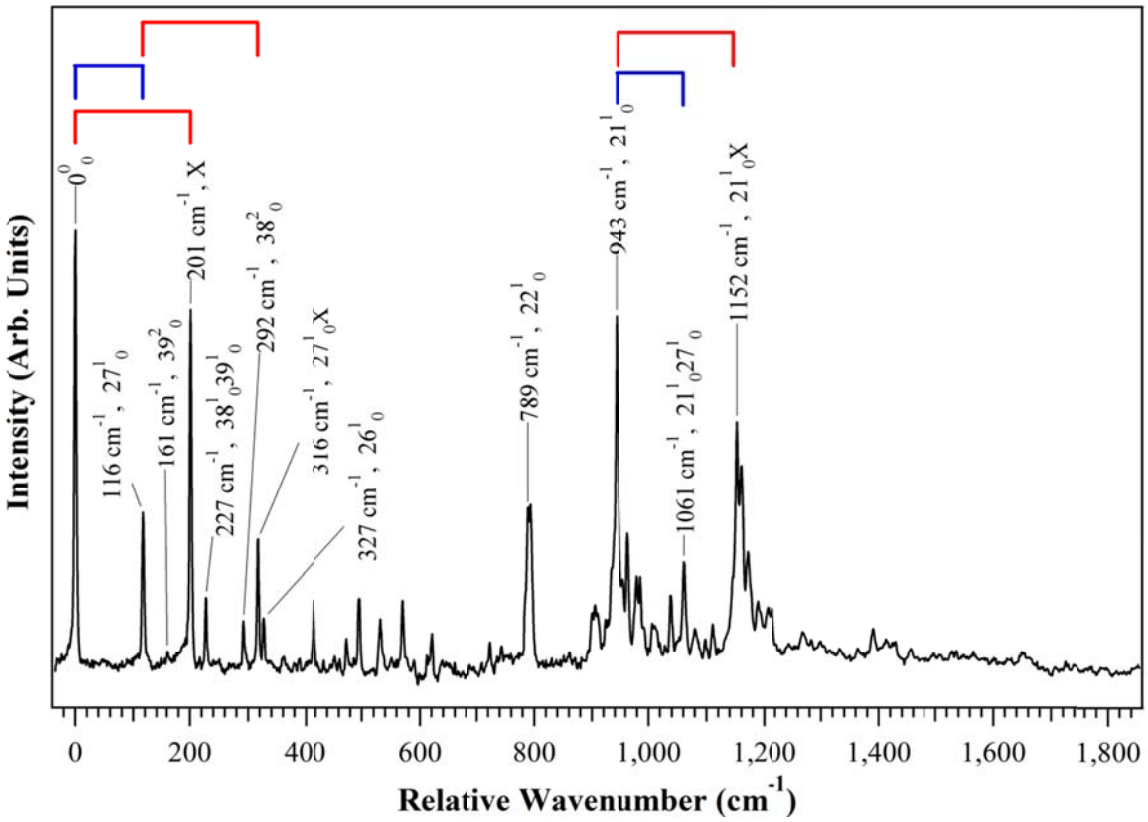

Figure 4.2. 2C-R2PI excitation spectrum of the phenylcyanomethyl radical in relative wavenumbers. The D_0-D_1 electronic origin is located at 21,402 cm^{-1}.

The transition appearing 116 cm^{-1} above the electronic origin is assigned to 27^1_0, involving the in-plane bend of the cyanomethyl substituent against the aromatic ring. The close analog of ν_{27} in PCM occurs at 117 cm^{-1} (ν_{29}) in 1PPR. Theory predicts the next in-plane fundamental to occur at 341 cm^{-1}, and thus the experimental transitions occurring at frequencies lower than 341 cm^{-1} likely involve combinations or even overtones of out-of-plane (a") vibrations. We assign the transitions at + 227 cm^{-1} and +292 cm^{-1} to $38^1_0 39^1_0$ and 38^2_0, respectively, by analogy to 1PPR. These assignments are confirmed in a slightly saturated laser induced fluorescence (LIF) spectrum (not shown) provided by our collaborator Dr. Timothy Schmidt. The LIF spectrum clearly shows a transition at 161 cm^{-1}, which can only be reasonably assigned to 39^2_0, and since the transition at 292 cm^{-1} is 38^2_0, it follows that the transition at 227 cm^{-1} is indeed $38^1_0 39^1_0$.

Provided these assignments for the 116 cm^{-1}, 227 cm^{-1}, and 292 cm^{-1} transitions, the assignment of the prominent transition at 201 cm^{-1} remains. This +201 cm^{-1} transition has no close analog in 1PPR, being far more intense than anything in this region in the spectrum of 1PPR. We will detail the potential assignments for the 201 cm^{-1} in the Discussion section of this chapter. In what follows, we refer to this transition as X. Other strong vibronic transitions at 789 and 943 cm^{-1} have counterparts in 1PPR at 770 and 917 cm^{-1}, and therefore can be assigned analogously as 22^1_0 (1) and 21^1_0 (12), respectively, and are two ring deformation modes. The transitions 201 and 207 cm^{-1} above the 27^1_0 and 21^1_0 transitions are tentatively assigned to 27^1_0X and 21^1_0X, and are connected by red tie lines in Figure 4.2 that highlight this possibility. Finally, by analogy to ν'_{28} in 1PPR, we assign the transition at 327 cm^{-1} to the in-plane fundamental 26^1_0. A summary of the assignments is provided in Table 4.1, alongside scaled[23] calculated frequencies.

Table 4.1. Assigned transitions for the phenylcyanomethyl radical 2C-R2PI spectrum

		D_1 State	
Mode[a]	Approximate description[b]	Expt[c]	Calc[d]
	a'		
ν_{21}	12	943	946
ν_{22}	1	789	797
ν_{26}	ρ (C1C2N)	327	322
ν_{27}	ρ (C1'C1C2)	116	116
	a"		
ν_{38}		146	133
ν_{39}		81	84

[a] Numbering according to Mulliken scheme.
[b] Approximate description of normal mode in excited state. ρ = rocking. Varsanyi notation used when applicable.
[c] Experimental frequencies (cm^{-1}), measured from the D_0-D_1 origin.
[d] TD-DFT UB3LYP/6-311+G(d,p) calculated excited state frequencies (cm^{-1}), scaled by 0.9688.

4.3.2. Photoionization Efficiency Scans

Just as the excitation spectrum provides the Franck-Condon factors between the D_0 zero-point vibrational energy level to different modes in the D_1 excited state, photoionization efficiency scans have intensity profiles dictated by Franck-Condon factors between the D_1 excited state of the radical and S_0 state of the radical ion. The ionization potential for the m/z = 117 PCM radical was found to be 7.935 ± 0.002 eV (Figure 4.3), with the error estimated from the field effect study of Duncan and coworkers.[24] The sharp onset of ion signal at 7.935 eV indicates that the radical undergoes little geometry change from D_1 to the S_0 of the ion, with strong $\Delta v = 0$ Franck-Condon factors governing the ionization threshold behavior.

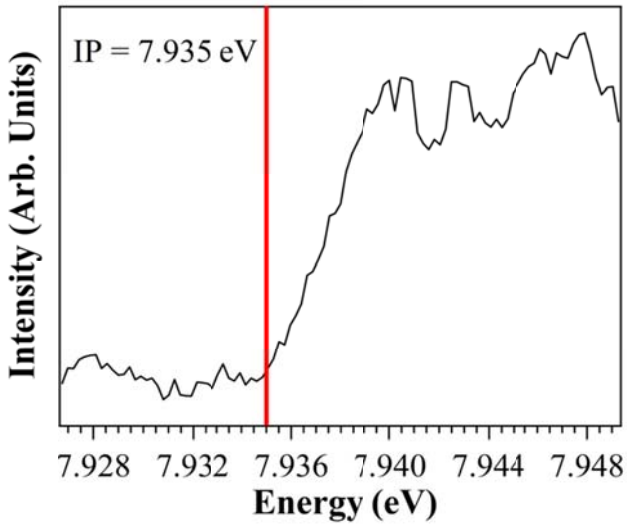

Figure 4.3. Photoionization efficiency scan of the phenylcyanomethyl radical at the D_0-D_1 origin in eV. The IP for the phenylcyanomethyl radical is 7.935 ± 0.002 eV.

As a check, the ionization potentials for the structural isomers of C_8H_6N (the phenylcyanomethyl radical, the phenylisocyanomethyl radical, and the indolyl radical) were calculated and are presented in Table 4.2. From the table, the phenylcyanomethyl radical and the indolyl radical are both candidates species with ionization potentials near the experimentally measured value of 7.935 eV for the m/z = 117 C_8H_6N radical in the

present study. However, the close correspondence between the spectrum of PCM and that for 1PPR argues for PCM as the carrier, since the electronic states of the indolyl radical are quite different than those of PCM. In addition, cursory excited state calculations for the indolyl radical (C_s point group) indicate that the lowest frequency in-plane fundamental is predicted at ~400 cm^{-1}, making the indolyl radical an unlikely candidate for the C_8H_6N radical in this study. With the vibronic spectroscopy presented in section 4.3.1, and the ionization potential data of this section, we assign the identity of the C_8H_6N radical of this work as the phenylcyanomethyl radical, which has an experimentally determined ionization potential of 7.935 ± 0.002 eV. Note that the ionization potential for PCM is about 0.5 eV higher than that for 1PPR (7.4 eV),[15] as expected for nitrile substitution in place of an ethynyl group.

Table 4.2. Calculated[a] and experimental IPs for C_8H_6N structural isomers

	Vertical Calc IP (eV)	Adiabatic Calc IP (eV)	Expt IP (eV)
Phenylcyanomethyl radical	7.947	7.866	7.935
Phenylisocyanomethyl	7.576	7.518	N/A
Indolyl radical	8.174	8.063	N/A

[a] IPs calculated using zero-point corrected energy differences between the S_0 radical ion state and the D_0 radical ground state using UB3LYP/6-31+G(d). Vertical IPs are calculated without optimizing S_0 radical ion structure, and adiabatic IPs are calculated with optimized S_0 radical ion structure.

4.3.3. Rotational Band Contours

As a nitrile substituted benzyl radical, the electronic excited states of PCM are anticipated to be similar to those of benzyl. The benzyl radical is known to have two close-lying doublet (D) excited states, a D_1 state with a transition dipole moment (TDM) from the ground state (D_0) pointing along the 'b' axis, and a D_2 state with an 'a-axis' polarized transition from D_0.[25] The analogous set of states is also identified by excited state calculations of PCM.

Figure 4.4 presents an experimental rotational band contour for the D_0-D_1 origin transition at 21,402 cm^{-1}, recorded at a resolution of ~0.06 cm^{-1}. Though the resolution of this scan is insufficient to resolve rotational substructure, we are able to obtain a band contour that reflects the direction of the transition dipole moment upon electronic excitation and thus able to identify the excited state associated with our spectral region. From our b-type experimental rotational band contour (Figure 4.4), which necessarily lacks the presence of a Q branch typical of a-type contours, we identify this excitation spectrum as belonging to the D_0-D_1 transition of the phenylcyanomethyl radical. As the phenylcyanomethyl radical belongs to the C_s point group, the b-type contour of the origin band indicates that the transition dipole moment corresponds to the horizontal plane of symmetry of the molecule (in-plane), a finding which is consistent with the $\pi^* \leftarrow \pi$ transition predicted by calculations.

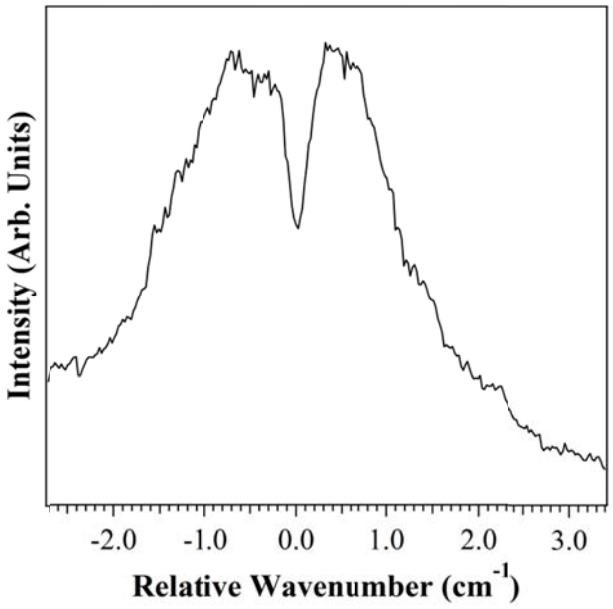

Figure 4.4. Rotational band contour of the phenylcyanomethyl radical at the D_0-D_1 origin in relative wavenumbers. The b-type contour of the vibrational envelope indicates an in-plane transition dipole moment, which is consistent with the predicted $\pi^* \leftarrow \pi$ transition.

4.3.4. Excited State Lifetime

For further characterization of the phenylcyanomethyl radical, the excited state lifetime at the D_0-D_1 origin (Figure 4.5) was obtained by scanning the delay between λ_1 (used for D_0-D_1) and λ_2 (used in the ionization step from the D_1 state). The experimental time profile can be fit to a single exponential, with a value of 455 ± 61 ns. This value is larger than the excited state lifetime of 1PPR, which is reported as 350 ns at the D_1 origin.[7] The long excited state lifetime for PCM reflects a weak oscillator strength for the D_0-D_1 transition, much like the case of the benzyl radical. The calculated oscillator strength for the D_0-D_1 transition is 0.0033.

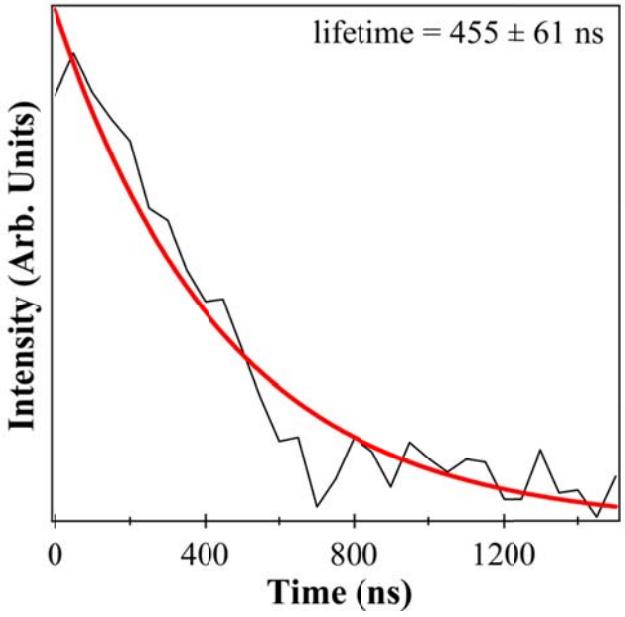

Figure 4.5. Excited state lifetime scan of the phenylcyanomethyl radical at the D_0-D_1 origin in nanoseconds. The excited state lifetime for the phenylcyanomethyl radical at the D_0-D_1 origin is 455 ± 61 ns.

4.4. Discussion

4.4.1. Vibronic Structure and Duschinsky Rotation

Since the PCM radical is the nitrogen-containing analog of the extensively studied 1PPR radical,[7, 8, 14, 15] it is only natural to make a comparison of the properties of the two radical species. The $D_1(^2A'')\leftarrow D_0(^2A'')$ origin transition for the PCM radical is located at 21,402 cm^{-1}, just 395 cm^{-1} to the blue of the $D_1(^2A'')\leftarrow D_0(^2A'')$ origin of the 1PPR radical at 21,007 cm^{-1}.[7, 8] This blue shift is consistent with the general trend in nitrile-substituted aromatics relative to their ethynyl counterparts. For example, the S_0-S_1 origin transition of benzonitrile is 635 cm^{-1} to the blue with respect to phenylacetylene.[26, 27]

Much of the vibronic activity in the spectrum of the PCM radical closely matches that of the 1PPR radical. Both the PCM and 1PPR radicals share a prominent origin indicating modest geometry change upon excitation, similar low frequency activity, and ring modes with significant Franck-Condon activity from approximately 700 to 1,200 cm^{-1}. The intense +201 cm^{-1} transition of PCM does not have a direct analog in the excitation spectrum of 1PPR. Since the lower frequency in-plane fundamental transitions (27^1_0 and 26^1_0) and the lower frequency even overtones of an out-of-plane transition (39^2_0 and 38^2_0) and their combination ($38^1_0 39^1_0$) have been accounted for, other assignments for the +201 cm^{-1} transition must be considered.

Alternate possibilities for the +201 cm^{-1} transition include a different structural isomer, a second excited state, or a transition appearing due to vibronic coupling with higher excited states. To explore the possibility that this transition could arise from a different structural isomer, vis-vis hole-burning experiments were attempted. However, the weak electronic transition of PCM and its long excited state lifetime prevented the acquisition of hole-burning spectra. A photoionization efficiency scan of the +201 cm^{-1} transition was also collected, and was found to be identical to that of the D_0-D_1 origin (7.935 eV) providing conclusive evidence that the transitions belonged to the same species.

Given the anticipated close proximity of the D_2 state relative to D_1, it is possible that the +201 cm^{-1} transition is the electronic origin of the D_2 state. Evidence against this possibility arises from its rotational band contour, which closely resembles the b-type rotational band contour corresponding to the D_0-D_1 origin of PCM, indicating that the +201 cm^{-1} transition gathers its oscillator strength from the D_1 state and not D_2 (which is calculated to have a primarily a-type band character). Evidence in favor of assignment of the +201 cm^{-1} transition to the D_0-D_2 origin comes from the dispersed fluorescence spectrum of this band. These spectra, recorded by the Schmidt group, show a dispersed fluorescence spectrum for the +201 cm^{-1} band that is origin-like in its emission, with emission bands involving ring fundamentals that are the same those from the D_1 origin, but differing in intensity.

A final intriguing possibility is that vibronic coupling is playing a role in inducing intensity in the +201 cm^{-1} band. Since the nitrile group has both in-plane and out-of-plane p orbitals, there are higher-lying electronic states (D_n) that could couple to D_1 via an out-of-plane fundamental(s), with out-of-plane D_0-D_1 transition dipole moments. Indeed, there is an out-of-plane vibration in D_1 with frequency near 200 cm^{-1}, which could in principle engage in first-order vibronic coupling to higher lying A' states. Such transitions with out-of-plane transition dipole moments would produce c-type RBCs and exhibit a strong Q branch however, counter to the b-type band contour observed for the 201 cm^{-1} transition in experiment. Furthermore, DFL spectra from Dr. Schmidt for the 201 cm^{-1} transition do not exhibit $\Delta v = \pm 1$ emission, arguing against the role of such vibronic coupling. Second-order vibronic coupling is also possible, leading to mixing of $v' = 2$ with $v' = 0$ in D_1 through an intermediate a' fundamental in an A" D_n state. These possibilities are being investigated by Dr. Slipchenko and Dr. Nebgen. The source of the +201 cm^{-1} will be reassessed upon completion of the vibronic coupling calculations.

Like in the case of the 1-phenylpropargyl radical, there is the potential for Duschinsky mixing[28] to also be present in the excited state of the phenylcyanomethyl radical. Duschinsky mixing was already considered in some detail in our studies of *para*-diisocyanobenzene (Chapter 3) (E)- and (Z)-phenylvinylnitrile (Chapter 5) of this thesis, and is often accompanied by large changes in the low frequency modes of the molecule

where the effect spectroscopically manifests itself via the appearance of cross-sequence bands. There is potential for Duschnisky mixing between ν_{38} and ν_{39}, which could be confirmed further by DFL spectra.

4.4.2. Radical Stabilization Energy

One of the most important attributes of the PCM radical is its doubly resonance-stabilized character, with the radical site conjugated with both phenyl and nitrile groups. The radical stabilization energy (RSE) is a useful measure to assess the relative stability between carbon-centered radicals. By definition, the generic formulation for the RSE of a multiply substituted carbon-centered radical ·CXYZ is:

$$RSE(\cdot CXYZ) = BDE(CH_4) - BDE(CHXYZ)$$

where BDE is the bond dissociation energy of a particular species and X, Y, and Z represent substituents.[29] As an example, the bond dissociation energy for CHXYZ is the energy change in the reaction:

$$CHXYZ \rightarrow \cdot H + \cdot CXYZ$$

When Y = Z = H atom, the carbon-centered radical is monosubstituted, and when Z = H atom, the radical is doubly substituted.[29]

Using the ROCBS-QB3 formulation,[19] the RSE for the PCM radical and 1PPR were found to be 95.9 kJ/mol and 108.1 kJ/mol, respectively. The positive value of the radical stabilization energy indicates the multiply-substituted radicals PCM and 1PPR are stabilized relative to the methyl radical.[29] Since the key difference between 1PPR and the PCM radical is that the PCM radical has a cyano group in place of an acetylenic group in the molecule, the lower stabilization energy of the PCM radical indicates that the nitrile substituent has a slight net destabilizing effect relative to the ethynyl substituent. Nonetheless, the RSE of PCM is still very large, as anticipated based on its double resonance stabilization from the neighboring cyano and phenyl groups to the primary radical site.

Put another way, the large RSE means that the reaction PCM + CH_4 → $C_6H_5CH_2CN$ + CH_3 is endothermic by 95.9 kJ/mol. This means that reactions of this radical in Titan's atmosphere with most saturated and unsaturated hydrocarbons will not occur at the temperatures in Titan, causing the concentration of the PCM radical to accumulate to larger steady-state concentrations relative to other radicals lacking the same large resonance stabilization energy.

4.5. Conclusion

In this work, we provide the first spectroscopic characterization of PCM, a radical with unusual stability due to its double resonance stabilization. The excitation spectrum for the phenylcyanomethyl radical has been collected and tentatively characterized, with its D_0-D_1 origin at 21,402 cm^{-1}. The ionization potential for PCM is 7.935 ± 0.002 eV and excited state lifetime at the D_0-D_1 origin is 455 ± 61 ns. Ground state spectroscopic signatures in the microwave and far-IR would be additionally useful for astronomical searches for the phenylcyanomethyl radical. PCM is anticipated to be a likely intermediate in neutral pathways leading towards PANH, including photochemical pathways of importance in Titan's atmosphere.

4.6. References

1. Raulin, F., et al., Chem. Soc. Rev., 2012. **41** (16): p. 5380-5393.
2. Raulin, F., Space Sci. Rev., 2008. **135** (1-4): p. 37-48.
3. Tobie, G., D. Gautier, and F. Hersant, The Astrophysical Journal, 2012. **752** (2): p. 125.
4. Kasting, J.F., Science, 1993. **259**: p. 920-926.
5. Balucani, N., Chem. Soc. Rev., 2012. **41** (16): p. 5473-5483.
6. Cable, M.L., et al., Chem. Rev., 2012. **112** (3): p. 1882-1909.
7. Reilly, N.J., et al., J. Am. Chem. Soc., 2008. **130** (10): p. 3137-3142.
8. Reilly, N.J., et al., J. Chem. Phys., 2009. **130** (14).
9. Selby, T.M., et al., J. Phys. Chem. A, 2008. **112** (39): p. 9366-9373.
10. Newby, J.J., et al., J. Phys. Chem. A, 2007. **111** (43): p. 10914-10927.
11. Miller, J.A. and S.J. Klippenstein, J. Phys. Chem. A, 2001. **105**: p. 7254-7266.
12. Krasnopolsky, V.A., Icarus, 2009. **201** (1): p. 226-256.
13. Gautier, T., et al., Icarus, 2011. **213** (2): p. 625-635.
14. Troy, T.P., et al., J. Phys. Chem. A, 2009. **113** (38): p. 10279-10283.
15. Hemberger, P., et al., J. Phys. Chem. A, 2010. **114** (14): p. 4698-4703.
16. Wiley, W.C. and I.H. McLaren, Review of Scientific Instruments, 1955. **26** (12): p. 1150-1157.
17. M. J. Frisch, G.W.T., H. B. Schlegel, G. E. Scuseria, , et al., Gaussian 09, Revision B.01,, Gaussian, Inc., Wallingford CT, 2010.
18. Becke, A.D., J. Chem. Phys., 1993. **98** (7): p. 5648-5652.
19. Wood, G.P.F., et al., J. Chem. Phys., 2006. **125** (9): p. 094106.
20. Menon, A.S., et al., J. Phys. Chem. A, 2007. **111** (51): p. 13638-13644.
21. Mulliken, R.S., J. Chem. Phys., 1955. **23** (11): p. 1997-2011.

22. Varsanyi, G., *Assignments for Vibrational Spectra of 700 Benzene Derivatives*1974, New York: Wiley.

23. Merrick, J.P., D. Moran, and L. Radom, J. Phys. Chem. A, 2007. **111** (45): p. 11683-11700.

24. Duncan, M.A., T.G. Dietz, and R.E. Smalley, J. Chem. Phys., 1981. **75** (5): p. 2118-2125.

25. Fukushima, M. and K. Obi, J. Chem. Phys., 1990. **93** (12): p. 8488-8497.

26. Ribblett, J.W., D.R. Borst, and D.W. Pratt, J. Chem. Phys., 1999. **111** (18): p. 8454-8461.

27. Kobayashi, T., et al., J. Chem. Phys., 1987. **86** (3): p. 1111-1117.

28. Duschinsky, F., Acta Physicochimica Urss, 1937. **7** (4): p. 551-566.

29. Menon, A.S., et al., Organic & Biomolecular Chemistry, 2011. **9** (10): p. 3636-3657.

CHAPTER 5: VIBRONIC SPECTROSCOPY AND PHOTOCHEMISTRY OF (E)- AND (Z)-PHENYLVINYLNITRILE

5.1. Introduction

Titan, one of the moons of Saturn, has a fascinating, photochemically driven atmosphere rich in organic constituents. One of the reasons Titan has garnered interest is the insight that it could provide about the chemistry that may have occurred in prebiotic Earth. Titan is a model system for the study for primordial Earth for its: (i) nitrogen-dominated atmosphere (> 95%) that contains trace organics such as methane, hydrocarbons, nitriles, and benzene derivatives, (ii) methane cycle that is analogous to the water cycle on Earth, and (iii) the presence of a reducing atmosphere, which is similar to the weakly reducing atmosphere that is hypothesized for prebiotic Earth.[1, 2]

The atmospheric chemistry on Titan occurs primarily via the absorption of solar radiation. N_2 is broken down in the upper atmosphere via the absorption of vacuum ultraviolet radiation at wavelengths of 100 nm or shorter.[3] A little lower in the atmosphere, methane is photoprocessed via the absorption of 150 nm or shorter wavelength radiation.[3] The products of N_2 and CH_4 photoirradiation react through a complicated set of reactions to generate small hydrocarbons, nitriles, and benzene.[4] Given the established presence of benzene and a variety of nitriles on Titan, it is likely that phenyl-based nitrile derivatives are present in the atmosphere. In fact, mass spectrometric data from the Cassini mission has shown the presence of molecules larger in mass than benzene in Titan's atmosphere, although the molecular composition of these large ions is yet to be determined.[5]

The final end product of this gas phase photochemistry is the production of tholins, a term used to describe the orange-colored aerosol particles that envelop Titan's surface in clouds. Tholins are thought to be polymeric in nature, and to incorporate

nitrogen into their chemical structure, potentially in nitrogen heteroaromatic structures.[4, 6, 7] In order to complement observational and mission-based data on the physical and chemical properties of tholins, laboratory studies are also needed to map out potential pathways to complex organics and to tholin formation. Such laboratory studies serve as necessary input for developing photochemical models of Titan's atmosphere. Photochemical models are still far from complete, especially in describing larger molecules that may be of more direct prebiotic relevance. Indeed, in many cases, the models identify molecules larger than benzene as polymer, listing them merely by type (hydrocarbon or nitrogen-containing).[8, 9] Thus, there is a pressing need to obtain laboratory data in order to: 1) establish an experimental database of spectral signatures for future observation missions, and 2) provide valuable input data to refine photochemical models of the atmosphere.[10] With this goal in mind, the laboratory studies of (E)- and (Z)- phenylvinylnitrile ((E)- and (Z)-PVN) were undertaken.

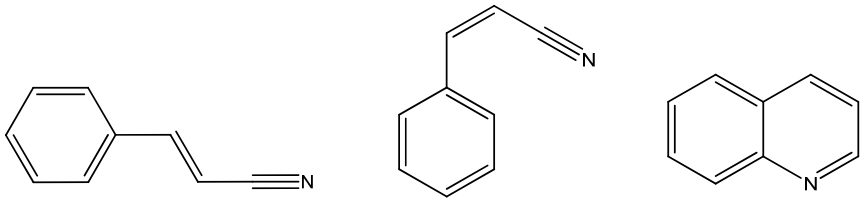

(E)-phenylvinylnitrile ((E)-PVN) (Z)-phenylvinylnitrile ((Z)-PVN) quinoline

Understanding pathways from first the aromatic ring to larger polycyclic aromatic hydrocarbons (PAH) and polyaromatic nitrogen heterocycles (PANH) is particularly important for prebiotic chemistry, since many of Earth's biological building blocks incorporate nitrogen into heterocyclic structures. Studying the formation pathways of nitrogen heterocycles is thus a necessary step to uncovering the chemical evolution that may have led to Earth's first biomolecules. It is also a meaningful step in exploring pathways that may be important in tholin formation. As such, (E)- and (Z)-PVN are particularly important to characterize and study photochemically, because they are structural isomers of the simplest PANH quinoline, with molecular formula C_9H_7N.

This chapter presents the isomer-specific vibronic spectroscopy of (E)- and (Z)-PVN, focusing attention on the S_0-S_1 region in the ultraviolet. Furthermore, the results of population transfer experiments and the test for a photoisomerization pathway that could

lead to the production of quinoline are shown. Similar spectroscopic and photoisomerization studies have been carried out on the hydrocarbon analog of (E)- and (Z)-phenylvinylnitrile; namely, (E)- and (Z)-phenylvinylacetylene ((E)- and (Z)-PVA).[11-14] The work on (E)- and (Z)-PVA thus forms an important point of comparison with the present study, probing the extent to which the nitrile substituent mimics or diverts from, its ethynyl analog, both in its spectroscopy and in its photochemical pathways.

5.2. Methods

5.2.1. Experimental Methods

(E)-PVN (cinnamonitrile, 97%) was purchased from Sigma-Aldrich and was used without further purification. No commercial sample of pure (Z)-PVN was available, but an (E)- and (Z)-PVN sample mixture was commercially available from Alfa Aesar (cis + trans cinnamonitrile, 97%), and was used as purchased. Isomer-specific spectroscopic techniques were used to distinguish between the two geometric isomers. Each sample was entrained in 3.8 bar backing pressure gas (helium) at ~ 60-70 ˚C and expanded through a small orifice of a Parker series 9 general valve to generate a supersonic expansion and cool the molecules down to their zero-point vibrational energy level.

In this work, the jet-cooled molecules were interrogated using laser induced fluorescence (LIF) and dispersed fluorescence (DFL). In LIF, the excitation spectrum of the molecule is collected by monitoring the total fluorescence of the molecules upon photon absorption as a function of laser excitation wavelength. DFL spectra map the emission from particular photoexcited levels in the excited electronic state onto vibrational levels in the ground electronic state. The tunable UV light for spectroscopy was generated by frequency doubling the visible output of a Nd:YAG pumped dye laser.

Isomer specific UV spectroscopy was carried out using two techniques: UV-UV hole-burning (UV-UV HB) spectroscopy, and UV depletion (UVD) spectroscopy. UV-UV HB is a double resonance technique that allows for isomer-specific detection. A 10

Hz hole-burn laser has its wavelength set on a transition of a particular isomer, and a 20 Hz probe laser is tuned through a spectral region of interest. The hole-burn and probe lasers are spatially overlapped but temporally separated such that the hole-burn laser precedes the probe laser by 200 ns. When the probe laser tunes through a transition that shares the same ground state as the hole-burn laser transition, a depletion is detected via active baseline subtraction in a gated integrator, such that an isomer-specific spectrum can be extracted.

UVD spectroscopy differs from UV-UV HB in that, in UVD, the hole-burn laser is tuned through the spectral region of interest, while the probe laser wavelength is fixed on a 'monitor' transition due to the particular isomer of interest. Though both UV-UV HB and UVD allow for isomer specific detection, UVD is capable of detecting transitions which do not fluoresce appreciably due to the presence of fast non-radiative processes. The sensitivity to detecting such transitions arises because, as long as the hole-burn laser removes population from a transition sharing the same ground state as the probe laser, a depletion in the fluorescence signal from the probe laser will be observed-- the depletion phenomenon is independent of whether or not the hole-burn laser tunes though a transition that itself can fluoresce.

Photochemistry experiments were carried out in a vacuum chamber outfitted with a linear time-of-flight mass spectrometer[15] that allowed mass-resolved detection of the photoproducts via resonant two-photon ionization (R2PI) spectroscopy. In the case of (E)- and (Z)-phenylvinylnitrile, the S_0-S_1 absorption requires a photon energy that is less than half way to the ionization potential, so one-color R2PI was not possible. Thus, (E)- and (Z)-PVN were characterized using two-color R2PI, with the second photon used to ionize the molecules provided by an ArF excimer laser (193 nm).

In order to conduct the photochemistry experiments, a reaction tube (1.7 cm length, 2 mm inner diameter) is affixed to the front of the valve face. The molecules in the pulsed valve undergo a pre-expansion into the reaction tube, where they get cooled down to a temperature of about 75-100 K,[16, 17] temperatures that are pertinent to the atmosphere of Titan.[3] The molecules can thereafter be selectively photoexcited, and if a viable pathway to photoisomerization exists, isomerize. Collisions with buffer gas during

the traversal of the reaction tube partially cool the excited population. Further collisional cooling of the photoexcited population to the zero-point levels of the reactant and the isomerization product occurs during the final supersonic expansion into the vacuum chamber from the end of the reaction tube. Photochemistry was initiated via UV hole-filling (UVHF) spectroscopy, a technique developed recently[13] as the UV analog of IR hole-filling techniques used to study ground state conformational isomerization.[18] In UVHF, a 10 Hz "pump" laser has its wavelength fixed on a strong transition of the photoreactant, and a 20 Hz probe laser is tuned through the spectral region of interest. In active baseline subtraction with a gated integrator, this should produce depletions in the transitions associated with the photoreactant, and gains in the transitions associated with the photoproduct.

5.2.2. Computational Methods

Assignment of the (E)- and (Z)-PVN spectra was aided by calculations. Density functional theory (DFT) and time-dependent density functional theory (TD-DFT) were used to computationally investigate the S_0 ground and S_1 excited states of (E)- and (Z)-PVN. Gaussian 09[19] was used to carry out S_0 and S_1 geometry optimizations and harmonic frequency calculations with the B3LYP functional and 6-311++G(d,p) basis set. Normal modes were visualized using ChemCraft software.[20]

Gaussian 09[19] was also used to map out stationary points along the ground state potential energy surface for (E)/(Z)-PVN → quinoline isomerization. QST3 calculations were run with the B3LYP/6-31G(d) functional and basis set to identify transition state structures. The intrinsic reaction coordinate from each transition state was followed in both the direction of the reactant and product using B3LYP/6-31G(d) in order to determine if the correct transition state was identified.[21-23] The energetics of the stationary points along the ground state potential energy surface were calculated using the G3B3 scheme.[24]

5.3. Results and Analysis

5.3.1. (E)-Phenylvinylvitrile

5.3.1.1. Computational Predictions

According to DFT and TD-DFT geometry optimizations conducted with B3LYP/6-311++G(d,p), (E)-PVN is predicted to be planar in both the S_0 ground and S_1 first excited electronic states. The presence of a true minimum was confirmed by the lack of imaginary frequencies in harmonic frequency calculations. With a planar geometry in both the S_0 and S_1 states, (E)-PVN contains a single horizontal mirror plane, and belongs to the C_s point group. Consequently, the 45 normal modes of (E)-PVN can be broken down into 31 totally symmetric (a', in-plane) vibrations and 14 non-totally symmetric (a", out-of-plane) vibrations. Electric dipole selection rules for transitions arising out of the zero-point vibrational energy level indicate that all transitions involving in-plane vibrations are symmetry-allowed, while out-of-plane vibrations will appear only as even overtones or combination bands of out-of-plane vibrations. In what follows, we describe the vibronic spectroscopy of (E)-PVN using Mulliken notation.[25] In order to connect more directly with the vibrations common to phenyl derivatives, we will at times also refer to specific transitions using Varsanyi notation for the vibrational modes, which stresses this commonality.[26]

5.3.1.2. LIF Excitation Spectrum, UV-UV HB, and UVD Spectroscopy

The LIF excitation spectrum of (E)-PVN from 33,600 - 35,850 cm^{-1} is presented in Figure 5.1a. The S_0-S_1 electronic origin was identified at 33,827 cm^{-1}, and was confirmed by UV-UV HB (Figure 5.1b), UVD (Figure 5.1c), and DFL spectroscopy (Figure 5.2b). Though the spectrum is congested over much of this region, the UV-UV HB spectrum above 35,500 cm^{-1} shows a sharp drop-off in intensity and broadening (Figure 5.1a,b), suggesting the onset of a non-radiative process. This is corroborated by

the UVD spectrum of (E)-PVN (Figure 5.1c), which shows intense, congested vibronic activity in this region, confirming that there are absorptions that carry significant oscillator strength in the region from 35,500 cm^{-1} onwards, but do not fluoresce.

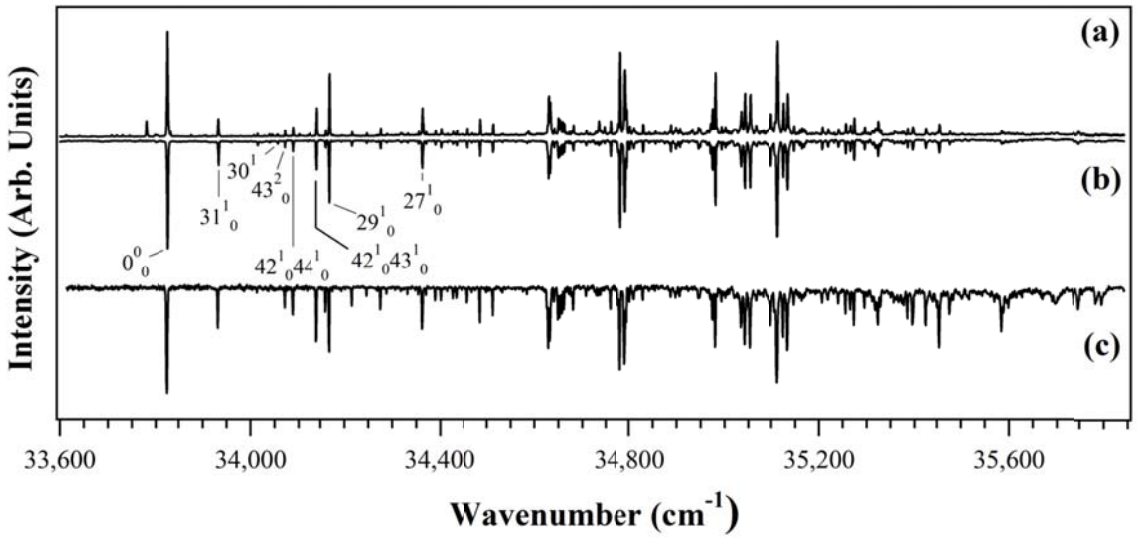

Figure 5.1. (a) LIF excitation, (b) UV-UV hole-burning, and (c) UV depletion spectra of (E)-PVN from 33,600-35,850 cm^{-1}.

Figure 5.1b contains labels for prominent assigned transitions in the first 800 cm^{-1} of the spectrum, while a more complete listing of the assigned modes and their frequencies is given in Table 5.1. Rationale for these assignments will be given in section 5.3.1.3, but a brief overview of the assignments is given here. The transitions at +106, +229, +343, and +536 cm^{-1} in the excited state are assigned to the in-plane fundamentals 31^1_0, 30^1_0, 29^1_0, and 27^1_0. The transitions at +246, +262, and +317 cm^{-1} are assigned to the 43^2_0, $42^1_0 44^1_0$, and $42^1_0 43^1_0$ transitions involving out-of-plane modes, on the basis of their extensive Duschinsky mixing and similarity to the vibronic spectroscopy of (E)-PVA. The transitions at higher energy in the excitation spectrum are harder to assign due to congestion in the spectrum, some of which arises from Fermi resonances and the loss of structure in the DFL spectra due to intramolecular vibrational energy redistribution (IVR), as will be explained in further detail in section 5.3.1.5.

Table 5.1. Experimental and calculated vibrational frequencies of (E)-phenylvinylnitrile

Mode[a]	Approximate description[b]	S_0 state		S_1 state	
		Expt.[c]	Calc.[d]	Expt.[c]	Calc.[e]
		a'			
ν_8	C≡N stretch	2,291	2,318		2,182
ν_9	C=C stretch	(1,810)	1,670		1,627
ν_{17}	C(1)-X stretch	1,279	1,295	1,155	1,238
ν_{22}	18a	(1,068)	1,050	(956)	1,045
ν_{25}	1	(890)	859	(804)	822
ν_{27}	6b	645	632	536	569
ν_{29}		386	383	343	375
ν_{30}		238	241	229	236
ν_{31}		110	109	106	109
		a"			
ν_{42}	16a	395	409	194	386
ν_{43}	10b analog	252	254	123	189
ν_{44}	C(1)-C(α) bend	92	94	68	99
ν_{45}	C(1)-C(α) torsion	48	63		41

[a] Numbering according to Mulliken numbering scheme.
[b] Approximate description of normal mode in ground state.
[c] Experimental frequency (cm^{-1}), measured from the S_0-S_1 origin. Tentative assignments are presented in parentheses.
[d] Ground state frequencies (cm^{-1}) calculated with B3LYP/6-311++G(d,p) without scaling.
[e] Excited state frequencies (cm^{-1}) calculated with TD-DFT: B3LYP/6-311++G(d,p) without scaling.

5.3.1.3. DFL Spectra in Low Frequency Region

The DFL spectrum of the (E)-PVN S_0-S_1 origin is presented in Figure 5.2b, and it is compared with first the 2,000 cm^{-1} of the UV-UV HB spectrum of (E)-PVN (Figure 5.2a). Much of the vibronic structure in the 0^0_0 DFL spectrum mirrors that in the excitation spectrum. Harmonic vibrational frequency calculations utilizing the B3LYP functional and 6-311++G(d,p) basis set aided the assignment of transitions in the ground state. The dispersed fluorescence of the S_0-S_1 origin shows Franck-Condon activity in

the in-plane fundamentals 31^0_1, 27^0_1 (6b), and 22^0_1 (18a), and 9^0_1 (-1,810 cm^{-1}, C(α)=C(β) stretch, tentative). These transitions reflect anticipated activity for a ππ* transition. Even overtones and combination bands of the out-of-plane modes are also observed as 45^0_2, $44^0_1 45^0_1$, and 43^0_2, as will be shown shortly. The exclusive presence of even overtones or combination bands of the out-of-plane modes confirms that (E)-PVN is planar in both the ground and electronic excited states, just as theory predicts.

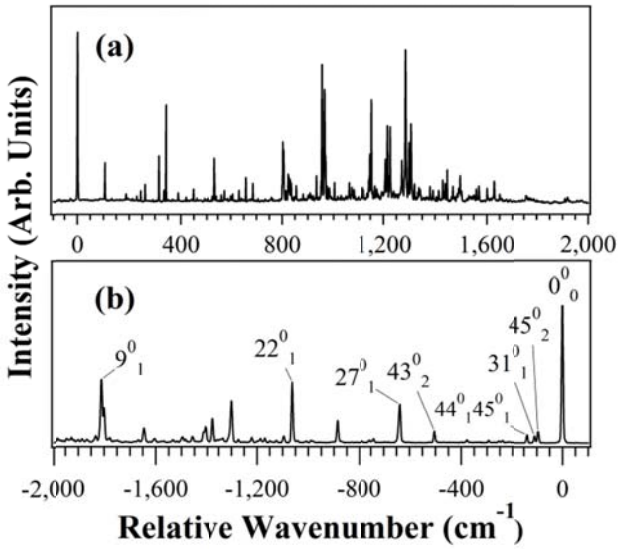

Figure 5.2. (a) UV-UV HB spectrum and (b) S_0-S_1 origin DFL spectrum of (E)-PVN.

The DFL spectra of several in-plane fundamentals are presented in Figure 5.3. The transitions at +106, +229, +343, and +536 cm^{-1} in the excited state can be affirmatively assigned to in-plane fundamentals 31^1_0, 30^1_0, 29^1_0, and 27^1_0 (6b) due to the presence of strong Δν = 0 Franck-Condon factors that serve as false origins in the respective DFL spectra. Table 5.1 shows good agreement between the experimental and calculated ground state frequencies for (E)-PVN, with the unscaled calculated harmonic frequencies matching experimental values closely.

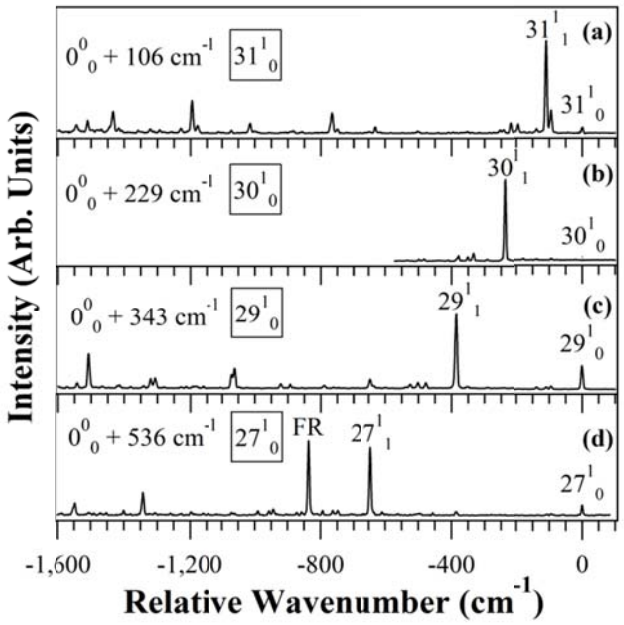

Figure 5.3. DFL spectra of low-frequency in-plane fundamentals in (E)-PVN: (a) 31^1_0, (b) 30^1_0, (c) 29^1_0, (d) 27^1_0.

DFL spectra from other transitions in the low-frequency region are much more congested. As Figure 5.4 shows, the 43^2_0 (+246 cm^{-1}), $42^1_0 44^1_0$ (+262 cm^{-1}), and $42^1_0 43^1_0$ (+317 cm^{-1}) transitions exhibit a pervasive presence of strong cross-sequence bands in their emission due to the presence of Duschinsky mixing, just as was the case in (E)-PVA.[11, 14] In Duschinsky mixing or rotation, the form of the normal modes changes between the ground and excited states, so that the normal modes in the excited state are represented as a linear combination of the ground state normal modes.[27, 28] For a C_s symmetry molecule such as (E)-PVN, the in-plane modes can displace along the normal mode coordinate upon electronic excitation, so that the normal mode coordinates can both shift and rotate between the ground and excited electronic states. For the out-of-plane modes, there is no displacement along the normal mode coordinate upon electronic excitation (if C_s symmetry is retained), but only rotation.

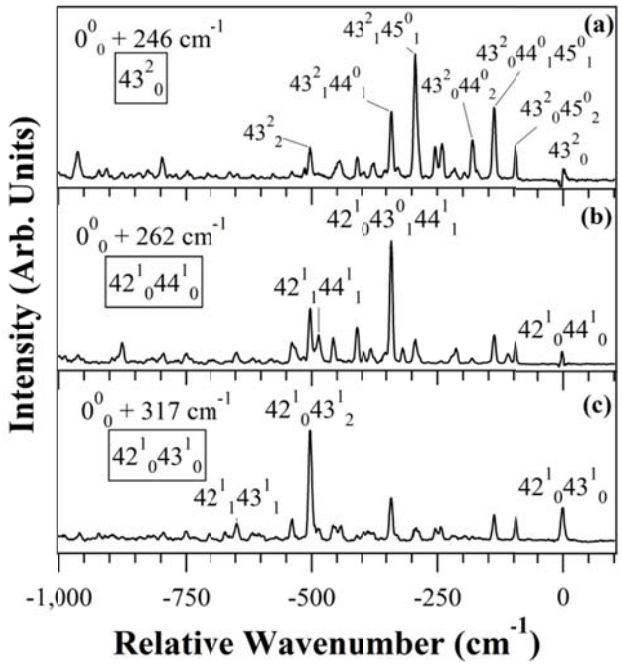

Figure 5.4. DFL spectra of transitions involving out-of-plane modes in (E)-PVN: (a) 43^2_0 (b) $42^1_0 44^1_0$ (c) $42^1_0 43^1_0$.

A characteristic signature of Duschinsky mixing is the presence of strong cross-sequence bands in the DFL spectra, which show directly that the upper state prepared by the laser has a mixed vibrational character when projected back onto the ground state. In looking at the highly Duschinsky mixed DFL spectra from 43^2_0, $42^1_0 44^1_0$, and $42^1_0 43^1_0$, it is difficult at first glance to identify the respective ground state emissions to 43^2_2, $42^1_1 44^1_1$, and $42^1_1 43^1_1$. This is due to the high degree of mode mixing in these low frequency out-of-plane modes. For example, in Figure 5.4a, when the transition 43^2_0 is probed, the most prominent emission occurs at $43^2_1 45^0_1$. Likewise, when $42^1_0 44^1_0$ (Figure 5.4b) and $42^1_0 43^1_0$ (Figure 5.4c) are pumped, emission primarily occurs to the $42^1_0 43^0_1 44^1_1$ and $42^1_0 43^1_2$ ground state levels, respectively.

Figure 5.5 shows the ground state forms of the normal modes $\nu_{42\text{-}45}$ which are involved in the Duschinsky mixing. These have close counterparts in (E)-PVA. Associating these modes with motion along specific internal coordinates is not possible. However, the dominant characters of the modes are as follows. Mode 42 involves out-of-

plane ring deformation (16a), mode 43 is a substituent-sensitive out-of-plane bend, mode 44 is predominantly the C(1)-C(α) bend, and mode 45 is the C(1)-C(α) torsion.

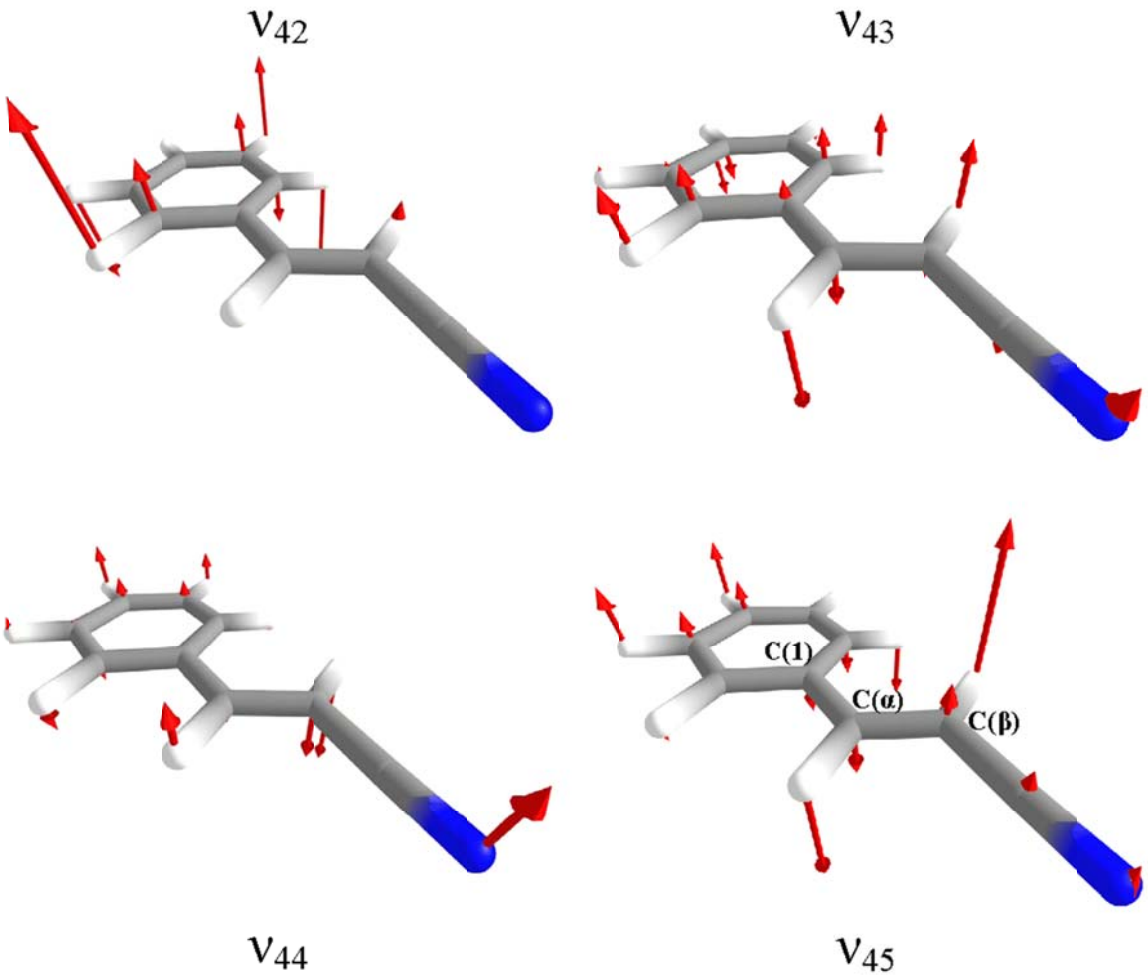

Figure 5.5. Ground state normal modes $\nu_{42\text{-}45}$ of (E)-PVN. Normal modes were calculated at the B3LYP/6-311++G(d,p) level of theory.

5.3.1.4. DFL Spectra of Hot Bands

Due to the complex nature of the emission involving out-of-plane modes, hot band studies were carried out. Since hot band transitions come from levels with v" = 1 in the lowest-frequency modes, the allowed transitions populate v' = 1 levels in the excited state. In the case of Duschinsky mixed vibrations, their hot bands help strengthen the assignments just made for the even overtones and combination bands.

Hot bands were generated by reducing the backing pressure of the supersonic expansion to 2.0 bar, and acquiring LIF spectra near the S_0-S_1 origin region at this reduced backing pressure. Figure 5.6a shows warm LIF spectrum of (E)-PVN near the S_0-S_1 origin region, with any hot bands generated identified. The cold LIF spectrum of (E)-PVN is presented in Figure 5.6b for reference. By comparing the LIF spectra in Figures 5.6a,b, hot bands were identified at -22, +22, +32, +77, and +152 cm^{-1}. The transition at -46 cm^{-1} in Figure 5.6b is attributed to a cluster (likely dimer) due to its disappearance when the expansion is warmed, and its absence in both the UV-UV HB (Figure 5.1b) and UVD (Figure 5.1c) spectra of (E)-PVN.

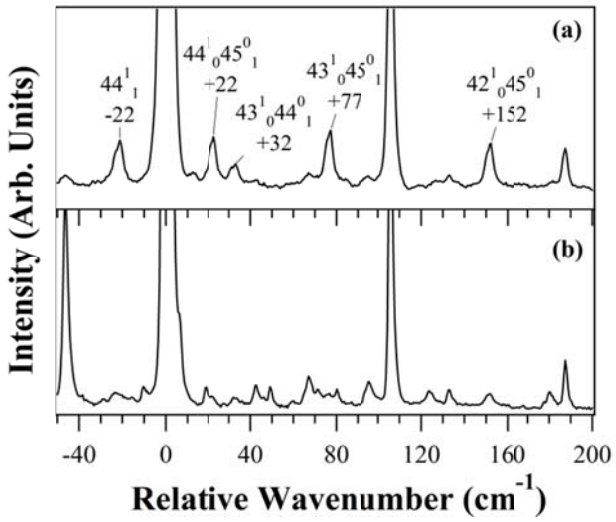

Figure 5.6. LIF excitation spectra recorded near the S_0-S_1 region of (E)-PVN as a function of backing pressure: (a) 2.0 bar and (b) 3.8 bar.

Figure 5.7 presents DFL spectra arising from the hot bands in Figure 5.6a. As described earlier, the DFL spectra and assignment of these hot bands helps determine frequency differences between modes in the ground state via combination differences. The DFL spectra of the -22 and +22 cm^{-1} hot bands (Figure 5.7a,b) serve as a case in point. These spectra are identical in their emission, but shifted, which indicates that they share the same upper level (say X^1), but originate from different ground state levels (X_1 and Y_1). Since the DFL spectrum at -22 cm^{-1} has the resonance fluorescence as the most intense transition, it is attributed to the $X^1{}_1$ transition, suggesting an assignment for the +22 cm^{-1} band as $X^1{}_0Y^0{}_1$. Within this construct, it follows that the difference in ground (ν") and excited (ν') frequency for mode X is -22 cm^{-1} ($\nu'_X - \nu''_X = -22\ cm^{-1}$), and that the difference in frequency between mode X in the excited state and mode Y in the ground state must be +22 cm^{-1} ($\nu'_X - \nu''_Y = 22\ cm^{-1}$). These two equations reveal that the difference in ground state frequency of mode X and Y as $\nu''_X - \nu''_Y = +44\ cm^{-1}$, and demonstrate that mode X is ν_{44}, and mode Y is ν_{45}.

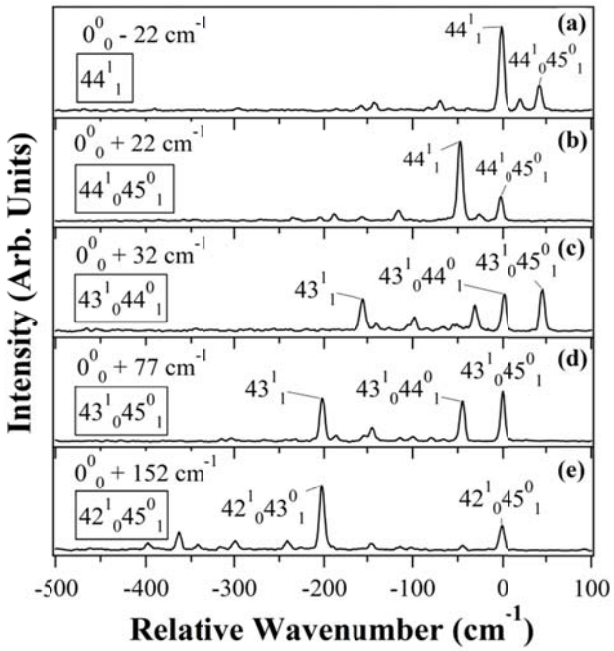

Figure 5.7. DFL spectra resulting from the excitation of hot bands in (E)-PVN: (a) $44^1{}_1$, (b) $44^1{}_0 45^0{}_1$, (c) $43^1{}_0 44^0{}_1$, (d) $43^1{}_0 45^0{}_1$, and (e) $42^1{}_0 45^0{}_1$.

Similarly, the hot bands at +32, +77, and +152 cm^{-1} are assigned to $43^1_0 44^0_1$, $43^1_0 45^0_1$, and $42^1_0 45^0_1$ respectively (Figure 5.7c-e). These (E)-PVN hot band spectra are nearly identical to the hot band spectra of (E)-PVA, indicating that Duschinsky mixing in both molecules is similar. Since a complete analysis of this mixing was given for (E)-PVA, the reader is referred there for further details.[14] It is important to note that 45^1_1 was not observed in the (E)-PVN hot band studies, similar to the absence of 48^1_1 (the analog of (E)-PVN's 45^1_1) in (E)-PVA.[11, 14] In (E)-PVA, ν'_{48} is predicted to be between the range of 230 and 350 cm^{-1}, and ν'_{45} of (E)-PVN is also likely in this range.

5.3.1.5. DFL Spectra in High Frequency Region

The DFL spectra of the higher energy portion of the LIF spectrum are presented in Figure 5.8. In the spectra of the +804 and + 956 cm^{-1} transitions, there are hints of IVR occurring due to the emergence of a broad background with superimposed sharp transitions. Fermi resonance and/or Duschinsky mixing is also evident in these spectra, which spreads intensity over a closely-spaced set of transitions spread over ~200 cm^{-1} about the nominal $\Delta v = 0$ transition. We tentatively ascribe the +804 cm^{-1} transition to 25^1_0 (1) and the +956 cm^{-1} transition to 22^1_0 (18a). Note that the latter DFL spectrum has strong transitions at -1,810 and -2,291 cm^{-1} which are assigned to $22^1_0 9^0_1$ (C=C stretch) and $22^1_0 8^0_1$ (C≡N stretch), respectively.

From 956 cm^{-1} onwards, the presence of IVR with its broadened origin-like emission is more obvious, with one glaring exception: the DFL spectrum of the +1,155 cm^{-1} transition. Though a transition just 6 cm^{-1} below at 1,149 cm^{-1} shows IVR, the transition at 1,155 cm^{-1} shows no signs of IVR. We infer that the transition at 1,155 cm^{-1} belongs to an in-plane fundamental, and that the neighboring transitions (at 1,149 cm^{-1}, etc) involve combinations of low frequency modes. The change in density of states over such a small energy change is negligible, so the differences in IVR efficiency are likely due to differences in the strength of anharmonic coupling of the initially prepared state to the background states. We assign the 1,155 cm^{-1} transition as 17^1_0, involving the C(1)-X stretch, where X represents the substituent side chain.

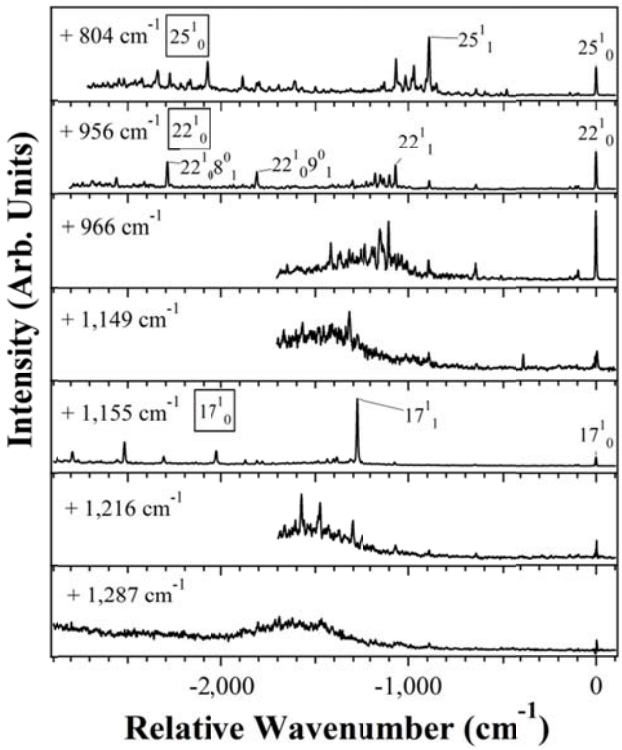

Figure 5.8. DFL spectra at the indicated wavenumber position above the S_0-S_1 origin of (E)-PVN.

5.3.2. (Z)-Phenylvinylnitrile

5.3.2.1. Computational Predictions

Ground state B3LYP/6-311++G(d,p) geometry optimizations predict that (Z)-PVN is planar in the S_0 state, and as such, (Z)-PVN belongs to the C_s point group. TD-DFT B3LYP/6-311++G(d,p) S_1 calculations fail to converge onto a C_s planar structure, though the spectroscopic analysis of (Z)-PVN data (section 5.3.2.3) indicates that (Z)-PVN retains (vibrationally-averaged) planarity in the excited state. Like its (E)-counterpart, (Z)-PVN has 45 normal modes, 31 of which are totally symmetric (a', in-plane) vibrations and 14 of which are non-totally symmetric (a", out-of-plane) vibrations.

The vibronic spectroscopy of (Z)-PVN was assigned using similar strategies as those used in (E)-PVN, once again using Mulliken notation as primary labels.[25]

5.3.2.2. LIF Excitation Spectrum and UVD Spectroscopy

(Z)-PVN was available in commercial form as a mixture of the (E)- and (Z)-isomers of PVN. Figure 5.9a shows the composite spectrum of (Z)- and (E)-PVN from 33,600 to 35,600 cm^{-1}, with the UVD spectrum of (Z)-PVN presented in Figure 5.9b. Though the UVD spectrum is a bit saturated, it allows for the clear identification of transitions resulting from (Z)-PVN even in the midst of the intense and congested transitions due to (E)-PVN. The S_0-S_1 origin of (Z)-PVN is identified at 33,707 cm^{-1}, 120 cm^{-1} to the red of the (E)-PVN origin at 33,827 cm^{-1}. Further details on the spectroscopic assignments are presented in section 5.3.2.3, but a summary of the assignments is presented here (Table 5.2). The transitions at +124, +221, +377, and +538 cm^{-1} are assigned to the in-plane fundamentals 31^1_0, 30^1_0, 29^1_0, and 27^1_0 respectively. The transitions at +99 and +189 cm^{-1} are even overtones of the two lowest-frequency out-of-plane modes 45^2_0 and 44^2_0, respectively. Theoretical calculations (section 5.3.2.1) and the previously established spectroscopy of (Z)-PVA were used as guides for analysis.[11, 12]

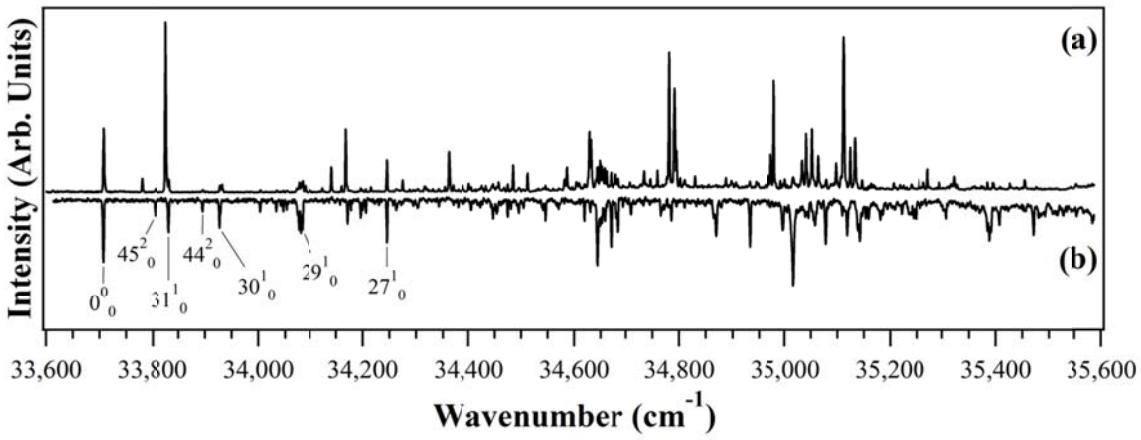

Figure 5.9. (a) Composite LIF excitation spectrum of (Z)- and (E)-PVN , and (b) UVD spectrum of (Z)-PVN from 33,600 to 35,600 cm^{-1}.

Table 5.2. Experimental and calculated vibrational frequencies of (Z)-phenylvinylnitrile

Mode[a]	Approximate description	S_0 state		S_1 state
		Expt.[c]	Calc.[d]	Expt.[c]
		a'		
ν_9	C=C stretch	1,627	1,657	
ν_{23}	12	1,007	1,016	
ν_{27}	6b	620	631	538
ν_{28}	6a + substituent motion	(554)	525	(370)
ν_{29}		388	400	377
ν_{30}		227	235	221
ν_{31}		126	123	124
		a''		
ν_{44}	C(1)-C(α) bend	154.3	157	94.5
ν_{45}	C(1)-C(α) torsion	18.5	35	49.5

[a] Numbering according to Mulliken numbering scheme
[b] Approximate description of normal mode in ground state.
[c] Experimental frequency (cm^{-1}), measured from the S_0-S_1 origin. Tentative assignments are presented in parentheses.
[d] Ground state frequencies (cm^{-1}) calculated with B3LYP/6-311++G(d,p) without scaling.

5.3.2.3. DFL Spectra in Low Frequency Region

The DFL spectrum of the S_0-S_1 origin for (Z)-PVN is presented in Figure 5.10b, with the UVD spectrum of (Z)-PVN shown in Figure 5.10a for comparison. Due to saturation effects in the UVD spectrum, it is more difficult to ascertain clearly the degree to which reflection symmetry is broken in (Z)-PVN. The DFL spectrum of the S_0-S_1 origin contains the in-plane fundamentals 31^0_1, 30^0_1, 29^0_1, 27^0_1, 23^0_1, and 9^0_1 (Table 5.2). Even overtones of the lowest frequency out-of-plane mode (45^0_2 and 45^0_4) are also discernible in the spectrum. The presence of even overtones of out-of-plane modes confirms that (Z)-PVN is planar in the ground and excited states.

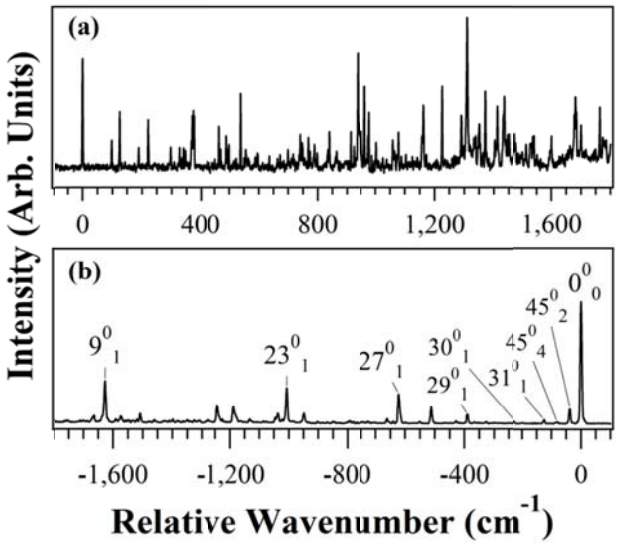

Figure 5.10. (a) UVD spectrum and (b) S_0-S_1 origin DFL spectrum of (Z)-PVN.

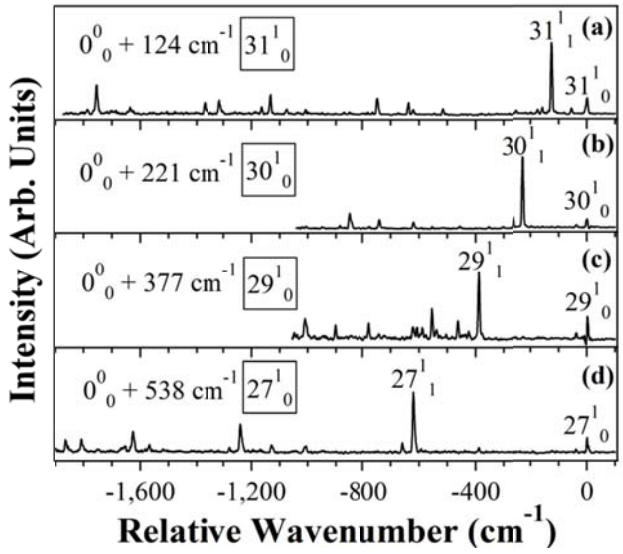

Figure 5.11. DFL spectra of in-plane fundamentals in (Z)-PVN: (a) 31^1_0, (b) 30^1_0, (c) 29^1_0, (d) 27^1_0.

The DFL spectra of (Z)-PVN in-plane fundamentals are presented in Figure 5.11. The transitions at +124, +221, +377, and +538 cm^{-1} were readily assigned to the in-plane fundamentals 31^1_0, 30^1_0, 29^1_0, and 27^1_0 due to the presence of prominent $\Delta v = 0$ emission

back to the corresponding v" = 1 levels in the ground state. The DFL spectra of even overtones of out-of-plane transitions and hot bands are presented in Figure 5.12. The transition at +99 cm^{-1} is assigned to 45^2_0, with the DFL spectrum (Figure 5.12b) displaying a torsional progression out to n = 8 with negative anharmonicity: 45^2_0, 45^2_2 (37 cm^{-1}), 45^2_4 (79 cm^{-1}), 45^2_6 (126 cm^{-1}), 45^2_8 (175 cm^{-1}), much like as was in the case of (Z)-PVA.[12] This assignment was confirmed by identification of the 45^1_1 hot band at +31 cm^{-1}, which appeared at lower backing pressure (1.7 bar). The DFL spectrum of this hot band (Figure 5.12a), shows a progression involving 45^1_n with n = 1, 3, and 5. The transition at +189 cm^{-1} is assigned to 44^2_0 and the DFL spectrum (Figure 12c) contains a prominent transition back down to 44^2_2.

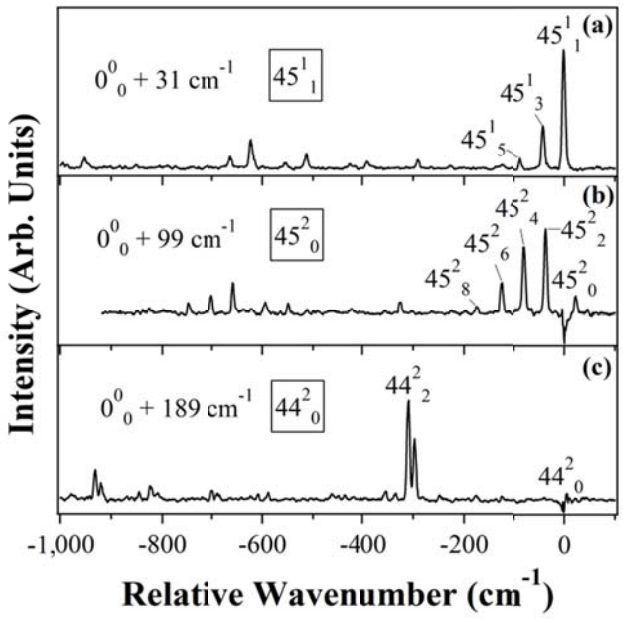

Figure 5.12. DFL spectra of (a) hot band 45^1_1 and even overtones (b) 45^2_0 and (c) 44^2_0 in (Z)-PVN.

5.3.3. Photochemistry of (E)- and (Z)-Phenylvinylnitrile

The characterization of (E)- and (Z)-PVN in sections 5.3.1-2. identified isomer-specific spectral transitions that are necessary for the photochemistry studies described in

this section. The (E)- and (Z)-PVN photoisomerization studies carried out here utilize the previously established methods of UVHF, in which selective excitation of one isomer is followed by supersonic expansion cooling to funnel population into the reactant and product zero-point levels prior to isomer-specific detection via R2PI spectroscopy.[13]

5.3.3.1. UVHF Spectroscopy

UVHF spectroscopy was used to follow the photo-induced isomerization of (E)↔(Z)-PVN. Figure 5.13a shows a UVHF spectrum of (E)→(Z)-PVN isomerization (black trace) starting from a pure sample of (E)-PVN. In order to obtain the UVHF spectrum, the origin of (E)-PVN was photoexcited with the "pump" laser (10 Hz), and a spectral region encompassing transitions both from the photoreactant ((E)-PVN) and the photoproduct ((Z)-PVN) was interrogated with the probe laser (20 Hz). Active baseline subtraction was used to record difference signals that reflect the change in population induced by the UV pump laser used to initiate photoisomerization. Following selective excitation of (E)-PVN in the reaction tube, transitions from (E)-PVN appeared downstream as depletions due to its loss as a photoreactant, while transitions from (Z)-PVN appeared as gains due to its formation as a photoproduct. Likewise, when the (Z)→(E)-PVN photoisomerization was investigated (black trace in Figure 5.13b) by pumping the (Z)-PVN origin, transitions of (Z)-PVN appeared as depletions, and transitions from (E)-PVN appeared as gains. This experiment was more challenging because the sample was an (E)/(Z) mixture, and therefore the difference signal at the (E)-PVN transitions was against a steady-state background signal.

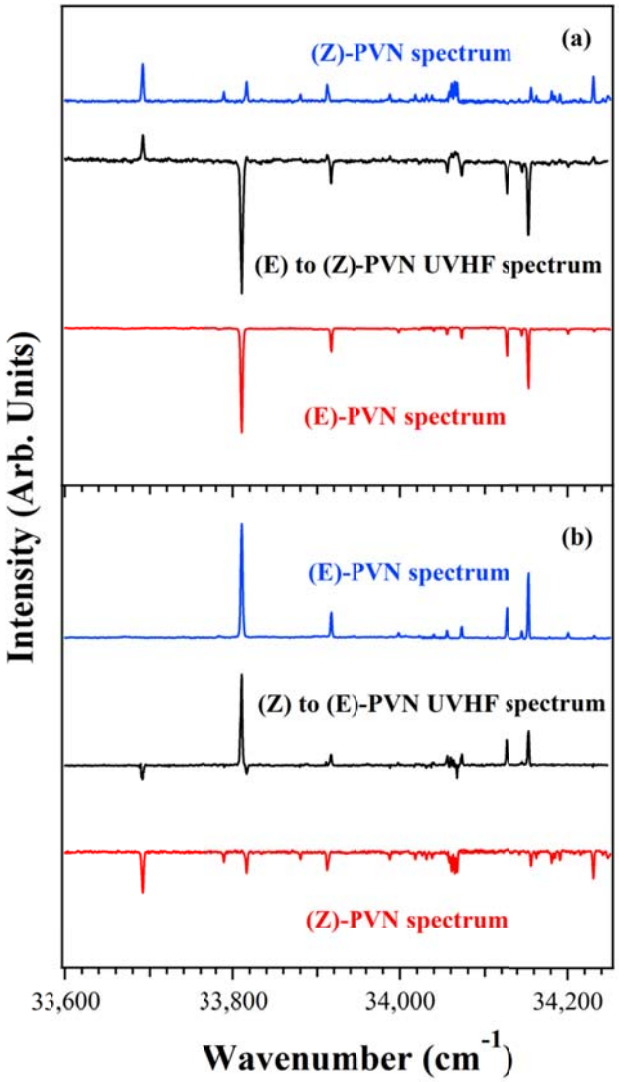

Figure 5.13. UVHF spectra demonstrating (a) (E)→(Z)-PVN isomerization (black) with the (E)-PVN (red) and (Z)-PVN (blue) spectra for comparison, and (b) (Z)→(E)-PVN isomerization (black) with the (Z)-PVN (red) and (E)-PVN (blue) spectra for comparison.

To further explore the parameter space associated with the photoisomerization experiments, two dimensional plots were generated (Figure 5.14). These two dimensional plots were collected as a function of the time delay between photoexcitation and ionization lasers (changing the reaction timescale of molecules excited in the reaction tube) and the time between the pulsed valve and ionization steps (mapping out where in the gas pulse we interrogate with the ionization lasers). The timing scans monitor either

the loss in photoreactant or gain in photoproduct. When monitoring the gain of (Z)-PVN, a bimodal distribution occurred with (Z)-PVN generated at short photoexcitation/ionization delays (130-140 μs, detecting photoproducts produced by photoexcitation near the end of the tube) and longer delays (150-165 μs, probing products formed by excitation of molecules near the beginning of the tube). It is important to note that at longer times between photoexcitation and ionization, wavelength selective photochemistry was not possible because the warmer temperature of the gas mixture in the beginning of the reaction tube prevented selective excitation of one isomer. However, at smaller time differences between photoexcitation and ionization (i.e. at the end of the reaction tube), wavelength selective photochemistry was possible. It is in this region that UVHF spectroscopy was carried out. The UVHF spectra not only show that (E)↔(Z)-PVN is possible, but also help provide confirmation that appropriate conditions are set up for the search for quinoline upon photoexcitation of (E)- and (Z)-PVN.

Note that the difference signals produced in the UVHF scans (Figure 5.13) were much larger in (E)-PVN than in (Z)-PVN, independent of the direction of photoisomerization ((E)→(Z) or (Z)→(E)). If the (E)↔(Z) isomerization is the only photochemical reaction that is occurring, then the loss in (Z)-PVN molecules equals the gain in (E)-PVN molecules and vice versa; that is, $\Delta N(Z) = -\Delta N(E)$. Under this assumption, it implies that the R2PI detection scheme at the respective S_0-S_1 origins is more sensitive in detecting (E)-PVN than (Z)-PVN by about a factor of 5, based on the ratio of their S_0-S_1 origin intensities in Figure 5.13. Since this ratio is similar for isomerization in both directions, it suggests that other photochemical products would be small. However, the formation of quinoline as a fused-ring heteroaromatic is such an important product that its formation as a minor product would nevertheless be significant. As a result, attention was turned next to searching specifically for quinoline as a photochemical product.

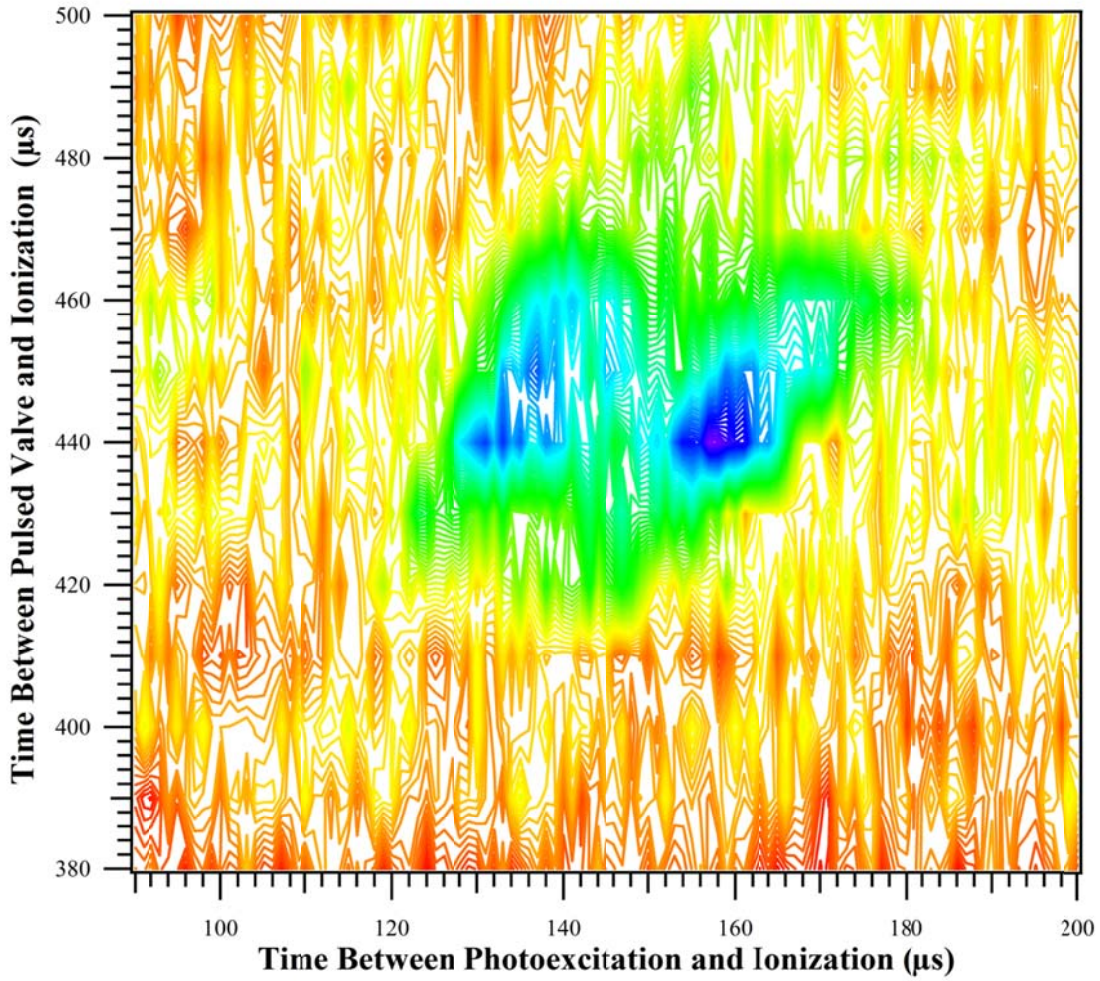

Figure 5.14. Two dimensional plot of (Z)-PVN gain as a function of the time between photoexcitation and ionization, and the time between the pulsed valve and ionization.

5.3.3.2. Search for Quinoline

After successfully demonstrating (E)↔(Z)-PVN photoisomerization, experiments were carried to test for the formation of quinoline from (E)- and (Z)-PVN photoexcitation. A combination of UVHF spectroscopy and 2D timing diagrams were used to test for the formation of quinoline upon the selective excitation of (E)- and (Z)-PVN at their S_0-S_1 origins. Quinoline was probed in the S_0-S_2 region (~310 nm), which is known to carry higher oscillator strength than the lower energy S_0-S_1 transition.[29] Prior to the photochemical experiments, a sample of quinoline was introduced into the chamber

so that its characteristic wavelengths could be accurately identified. Quinoline was then removed from the chamber, and the valve was purged until no detectable signal from quinoline was found, in order to prevent the presence of a false positive. Despite careful searches, no quinoline R2PI signal could be detected in our short timescale experiments following photoexcitation of either (E)- or (Z)-PVN. While potential differences in the detection sensitivities prevents us from making a quantitative determination of an upper bound for the quantum yield for quinoline formation, quinoline appears to be at most a very minor product. In the Appendix, we develop equations for determining the photochemical product yield that can assist those carrying out future photochemical experiments via these methods.

5.4. Discussion

5.4.1. Comparing the UV Spectroscopy Amongst (E)/(Z)-PVN and (E)/(Z)-PVA

The results and analyses in section 5.3.1,2 provide a thorough basis for the comparison of (E)/(Z)-PVN spectroscopy, and this comparison can naturally be extended to the ethynyl counterparts, (E)/(Z)-PVA. We start out with the comparison of (E)- and (Z)-PVN, a summary of which is provided in Table 5.3. The S_0-S_1 origin of (E)-PVN occurs at 33,827 cm^{-1}, 120 cm^{-1} to the blue of the origin of (Z)-PVN at 33,707 cm^{-1}. Both molecules have an excitation spectrum typical of a $\pi\pi^*$ excitation, with Franck-Condon activity present in several ring modes. While the anticipated 'mirror symmetry' between excitation and 0^0_0 DFL spectra is present in large measure in (E)-PVN, with transitions carrying large Franck-Condon intensity in the excitation spectrum also present with similar frequencies and intensities in the DFL spectrum, there are some noticeable differences. For instance, while the 31^1_0 and 29^1_0 transitions at +106 cm^{-1} and +343 cm^{-1} are large in the excitation spectrum are large, their counterparts in the 0^0_0 DFL spectrum (at -110 cm^{-1} and -386 cm^{-1}) are extremely weak. Similarly, strong transitions near 950 cm^{-1} in the excitation spectrum are without an obvious counterpart in the DFL spectrum. These differences highlight the likely presence of vibronic coupling between S_1 and a

higher S_n excited state of the same symmetry, turning on intensity in certain in-plane fundamentals in the excitation spectrum.[30] A deviation from the overall mirror symmetry in (E)-PVN also occurs due to the presence of a transition near -1,810 cm^{-1} (tentatively 9^0_1) in the 0^0_0 DFL spectrum, to which there is no analog in the excitation spectrum owing to the onset of non-radiative processes above 1,600 cm^{-1}. The saturation effects in the UVD spectrum of (Z)-PVN make it difficult to comment on the degree of mirror symmetry between the excited and 0^0_0 emission spectra, as well as locate the onset of non-radiative transitions.

Table 5.3. Comparison of (E)-PVN and (Z)-PVN

	(E)-PVN	(Z)-PVN
S_0-S_1 0^0_0 (cm^{-1})	33,827 cm^{-1}	33,707 cm^{-1}
non-radiative turn-on	1,600 cm^{-1}	N/A
Duschinky mixing	strong	weak
S_0 C(1)-C(α) bend	92 cm^{-1}	154.3 cm^{-1}
S_0 C(1)-C(α) torsion	48 cm^{-1}	18.5 cm^{-1}

A striking aspect of the (E)- and (Z)-PVN spectroscopy is that though Duschinsky mixing is prominent in (E)-PVN, it seems to play a minor role in the (Z)-PVN spectroscopy. Duschinsky mixing and frequency shifts are so prevalent in (E)-PVN that ν'_{45} is not observed in S_1, but is estimated to have a value of 230 - 350 cm^{-1}, near that in (E)-PVA. Unlike (E)-PVN, ν'_{45} is identified for (Z)-PVN. In the S_1 state, the 45^2_0 transition is clearly observed at +99 cm^{-1}, leading to an excited state torsional frequency of 49.5 cm^{-1}, much lower than in (E)-PVN. Thus, the C(1)-C(α) torsional barrier is much lower in the S_1 state of (Z)-PVN than in (E)-PVN. It is noteworthy that the ground state frequency of ν_{45} decreases from 48 cm^{-1} in (E)-PVN to 18.5 cm^{-1} in (Z)-PVN, indicating a softening of the C(1)-C(α) torsional potential in the (Z)- isomer relative to the (E)-isomer. This lower barrier torsional for (Z)-PVN may in part be due to the alleviation of steric strain upon C(1)-C(α) torsion.

A comparison of the spectroscopy of (E)-PVN and (E)-PVA[11-14] reveals how remarkably similar these two molecules are. Table 5.4 provides a summary of the properties of (E)-PVN and (E)-PVA. (E)-PVN has its S_0-S_1 (33,827 cm^{-1}) origin 250 cm^{-1} to the blue of the origin of (E)-PVA, which occurs at 33,578 cm^{-1}.[11] This blue shift while going from the nitrile to ethynyl versions is in qualitative agreement with the blue-shifted S_0-S_1 origin of benzonitrile (36,512 cm^{-1})[31] relative to phenylacetylene (35,879 cm^{-1}).[32] Non-radiative processes are present in both (E)-PVN and (E)-PVA, with onsets at 1,600 cm^{-1} and 1,000 cm^{-1} respectively.[13] Much like (E)-PVN, reflection symmetry between the excitation spectrum and 0^0_0 DFL spectrum is generally present in (E)-PVA, with deviations in modes 31, 28, 23, and 19.[11] These deviations suggest that these modes in (E)-PVA may be coupling to a higher electronic state S_n and producing these anomalies in mirror symmetry, analogous to what is proposed for (E)-PVN.[30] A region of intermediate IVR, such as that presented in Figure 5.8 for (E)-PVN, is also present in (E)-PVA, where some transitions appear to couple better to background states and undergo IVR more efficiently than other nearby transitions.[11] The Duschinsky mixing in (E)-PVN and (E)-PVA is also comparable, with many of the low frequency out-of-plane modes having similar values (Table 5.4) in both molecules, indicating analogous structural changes upon electronic excitation from S_0 to S_1 state.[11, 14]

Table 5.4. Comparison of (E)-PVN and (E)-PVA

	(E)-PVN	(E)-PVA
S_0-S_1 0^0_0	33,827 cm^{-1}	33,578 cm^{-1}
non-radiative turn-on	1,600 cm^{-1}	1,000 cm^{-1}
Duschinsky mixing	strong	strong
S_0 16a	395 cm^{-1}	398 cm^{-1}
S_0 PVN X sens. oop bend, oop C-C=C bend PVA	252 cm^{-1}	238 cm^{-1}
S_0 C(1)-C(α) bend	92 cm^{-1}	88 cm^{-1}
S_0 C(1)-C(α) torsion	48 cm^{-1}	43 cm^{-1}

A comparison of the properties of (Z)-PVN and (Z)-PVA[11, 12] is presented in Table 5.5. Unlike the trend observed for (E)-PVN/PVA, the S_0-S_1 origin of (Z)-PVN occurs to the red of the S_0-S_1 origin of (Z)-PVA, at 33,707 cm^{-1} and 33,838 cm^{-1} respectively.[11] In (Z)-PVA, mirror symmetry of the excitation and the 0^0_0 DFL spectra is broken, and the onset of non-radiative processes occurs at 600 cm^{-1} above the S_0-S_1 origin.[12, 13] It is less easy to gauge the reflection symmetry and a turn-on for potential non-radiative processes in (Z)-PVN, due to the saturation effects in its UVD spectrum coupled with the difficulty associated with identifying the pure (Z)-PVN transitions which are small relative to the larger (E)-PVN transitions in Figure 5.9a. Nonetheless, the DFL spectra of (Z)-PVN and (Z)-PVA clearly show that Duschinsky mixing is not as prevalent in these molecules relative to their (E)- isomer analogs.[12] The S_0 frequency for the C(1)-C(α) torsion and bend of (Z)-PVN/PVA are alike (Table 5), and the C(1)-C(α) torsional progression in (Z)-PVN (ν_{45}) has similar corresponding progression values in (Z)-PVA (ν_{48}).[12] As a result, we anticipate a similar S_0 torsional barrier height about the C(1)-C(α) bond of approximately 760 cm^{-1}.[12]

Table 5.5. Comparison of (Z)-PVN and (Z)-PVA

	(Z)-PVN	(Z)-PVA
S_0-S_1 0^0_0	33,707 cm^{-1}	33,838 cm^{-1}
non-radiative turn-on	N/A	600 cm^{-1}
Duschinky mixing	weak	weak
S_0 C(1)-C(α) bend	154.3 cm^{-1}	154 cm^{-1}
S_0 C(1)-C(α) torsion	18.5 cm^{-1}	17 cm^{-1}

5.4.2. Photoisomerization Pathways to Nitrogen Heteroaromatics

The central hypothesis motivating the present studies is that photoisomerization could offer a facile last step to PANH formation, following formation of non-cyclic structural isomers by preceding reactions. In the case of quinoline formation, a likely

pathway could involve addition of CN to styrene,[33] or acrylonitrile to phenyl to form (E)- and (Z)-PVN, which can potentially photoisomerize to quinoline:

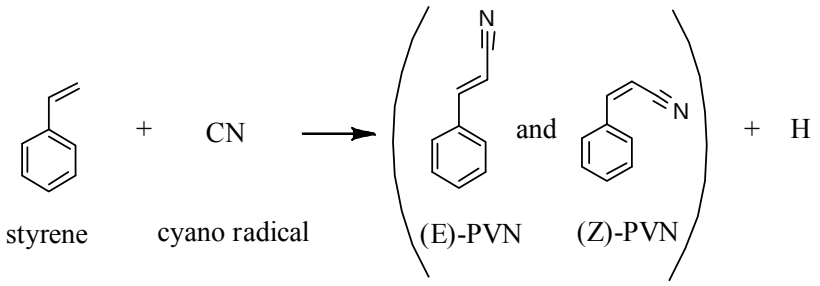

(1)

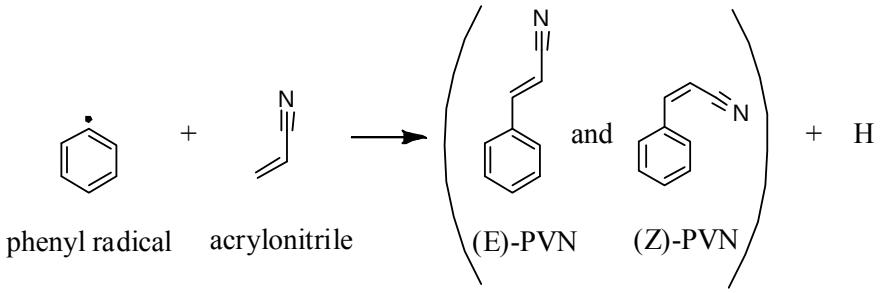

(2)

$$\text{(E)-PVN} + h\nu \rightarrow \text{(Z)-PVN} \rightarrow \text{quinoline}$$

$$\text{(Z)-PVN} + h\nu \rightarrow \text{quinoline}$$

Reaction (1) is calculated to be barrierless, and to lead, following attack at the terminal C of styrene, to the two PVN isomers, with an anticipated (E)/(Z) ratio of ~3:1.[33]

In section 5.3.3, we used UV hole-filling spectroscopy to demonstrate efficient (E)/(Z) photoisomerization that interconverted the two PVN isomers:

$$\text{(E)-PVN} + h\nu \rightarrow \text{(Z)-PVN}$$

and

$$\text{(Z)-PVN} + h\nu \rightarrow \text{(E)-PVN}$$

In order for this (E)↔(Z) isomerization to occur, a significant fraction of the excited population must cross over to the ground state surface, since the population recollects into the ground-state zero-point level of the (E)/(Z) isomerization product prior to isomer-specific detection. However, despite careful searches for quinoline under identical conditions, no evidence for its formation could be found. Potential causes for the absence of quinoline formation are considered below.

One possible reason for the lack of quinoline formation could be that an alternative pathway, such as photodissociation, could successfully compete with isomerization to quinoline. However, the long lifetimes of the S_1 state levels being probed, and the presence of facile (E)↔(Z) isomerization argue against this possibility.

An alternative reason for the lack of quinoline formation could be that an energetic barrier prevents formation of quinoline at the UV excitation energies used. The photoisomerization of cis-cis cyanobutadiene to form pyridine, one of the simplest nitrogen heteroaromatics, is analogous to the photoisomerization of (Z)-PVN to quinoline. The (cis-cis) cyanobutadiene + hν → pyridine reaction is calculated (G3 theory) to be a single step ring closing reaction that has a 70 kcal/mol barrier in the ground state.[34] One might anticipate a similar barrier to quinoline formation from (Z)-PVN, which would be well below the 96 kcal/mol available to (Z)-PVN following UV photoexcitation in the S_0-S_1 origin region. In another analogous case, the photoisomerization of (Z)-PVA to naphthalene is predicted to be a two step process, with calculated (DFT B3LYP/6-311+G(d,p)) barrier of about 55 kcal/mol,[13] which is also significantly lower than energy provided by a photon (96 kcal/mol) at the (Z)-PVN S_0-S_1 origin. With these relatively low energy barriers in mind, the photoisomerization

experiments probing the formation of quinoline from (E)/(Z)-PVN were undertaken, which were unable to detect quinoline. To seek a greater understanding of this result, we conducted theoretical calculations of the stationary points on the ground state potential energy surface leading from (E)/(Z)-PVN to quinoline.

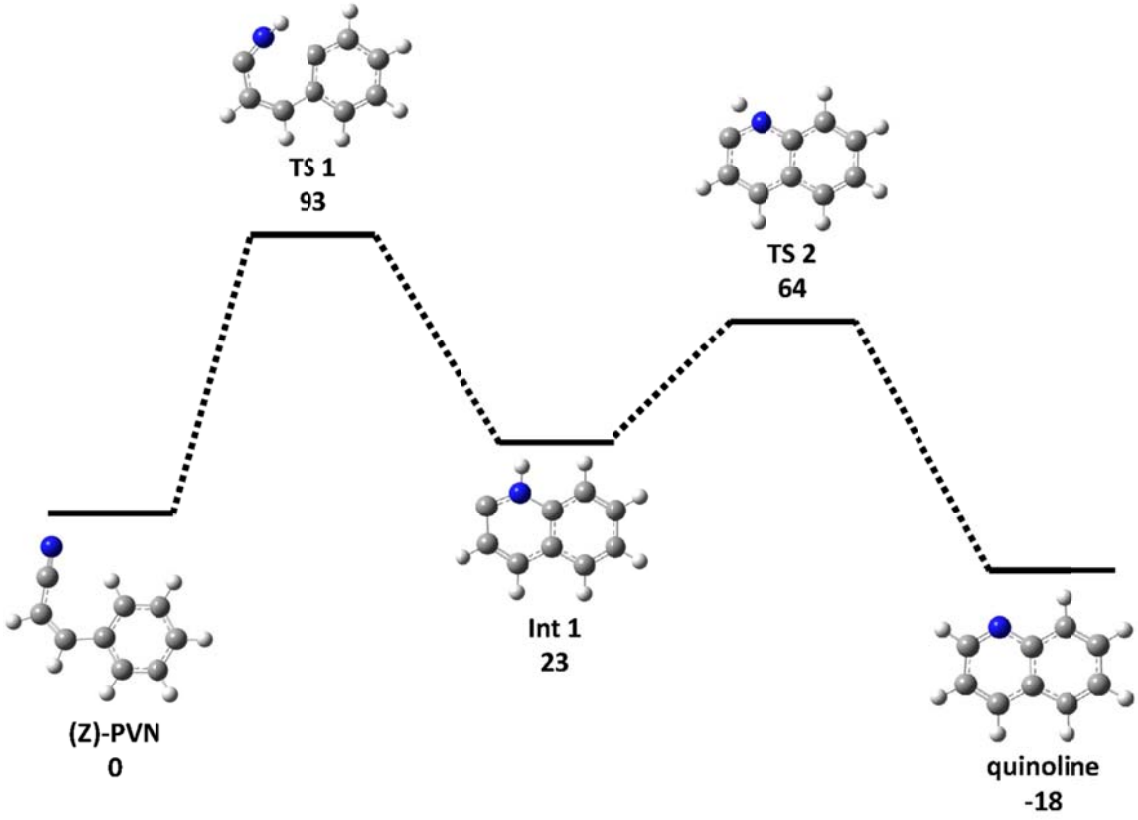

Figure 5.15. Stationary points along the ground state potential energy surface of (Z)-PVN to quinoline isomerization. Units are in kcal/mol.

Figure 5.15 summarizes this pathway, with energies calculated using the G3B3 scheme.[24] (E)-PVN is calculated to be approximately 1 kcal/mol lower in energy than (Z)-PVN (not shown in Figure 5.15). Theory predicts that the (Z)-PVN → quinoline isomerization pathway is a two step process. In the first step, (Z)-PVN isomerizes to an intermediate structure (Int 1) via an initial transition state (TS 1) that is 93 kcal/mol

higher in energy. In the second step, the intermediate structure (Int 1) overcomes a second energy barrier of 41 kcal/mol to lead to quinoline product formation. A surprising aspect of these calculations is the high activation (93 kcal/mol) energy associated with the first step in the isomerization process, which is just below the energy supplied (96 kcal/mol) by a photon at the (Z)-PVN S_0-S_1 origin. This predicted energy barrier is uniquely large, especially in light of the previous calculations on the (cis-cis) cyanobutadiene + hν → pyridine and (Z)-PVA + hν → naphthalene systems, which were calculated to have barriers of 70 kcal/mol and 55 kcal/mol, respectively.[13, 34] The high energy barrier predicted has far-reaching consequences for the absence of quinoline formation. If the multi-step unimolecular reactions are statistical, Rice-Ramsperger-Kassel-Marcus (RRKM) theory[35] can be applied to gain insight into the lack of quinoline photoproduct upon (Z)-PVN photoexcitation. According to RRKM theory, the rate constant of a unimolecular reaction k_a is given by:

$$k_a(E^*) = \frac{W(E^+)}{hN^*(E^*)} \tag{3}$$

where $W(E^+)$ is the number of energy levels available to the transition state at energy E^+, counting from the zero-point level of the transition state to E^+, the excess energy above the transition state zero-point level (supplied by the isomerization photon). $N^*(E^*)$ is the density of states (in states/cm^{-1}) of the reactant at energy E* (determined by the UV photon energy), and h is Planck's constant (in cm^{-1}·sec).

Applying equation (3) to the first step ((Z)-PVN → Int 1) of the reaction pathway provides a likely explanation for the lack of quinoline formation upon (Z)-PVN photoexcitation. The energy barrier in going from (Z)-PVN to Int 1 is quite high at 93 kcal/mol, such that the excess energy imparted by the photon is merely 3 kcal/mol. The number of energy levels of the transition state $W(E^+)$ is very small at 3 kcal/mol of additional energy, whereas the density of states of the reactant is very large. Consequently, the ratio of $\frac{W(E^+)}{N^*(E^*)}$ is quite small, thereby leading to a small value for the rate constant. Thus, the first step in the isomerization pathway, where (Z)-PVN

transforms to Int 1, is likely the rate determining step for the isomerization reaction. Since isomerization pathway to quinoline is multi-step, with relatively high barriers, the slow kinetics likely prevents its formation on the timescale of the present experiment. Indeed, one of the signatures of the present reaction tube studies is that they probe early-time photochemical events, with laser excitation initiating reaction, and expansion into vacuum at the end of the reaction tube quenching reaction tens of microseconds later. As such, the multi-step isomerization may be unlikely on these short timescales, with the formation of quinoline by exciting the S_0-S_1 origin of (E)-PVN even less probable due to the multiple steps needed to form quinoline: 1) (E)-PVN → (Z)-PVN, 2) (Z)-PVN → Int 1, and 3) Int 1 → quinoline. It would be very useful to test for quinoline formation from higher vibronic levels of S_1 in (E)- and (Z)-PVN, and on longer timescales in either bulb or flow conditions. These tasks are left for future work.

In Titan's atmosphere, the collision frequency changes dramatically as a function of altitude. Under these conditions, the photoisomerization of (E)- and (Z)-PVN to quinoline may occur with higher efficiency. Nonetheless, the characterization of (E)- and (Z)-PVN presented here provides spectral signatures for their search in planetary atmospheres, as well as for other photochemical studies where they may be a byproduct or precursor.

5.5. Conclusion

The spectroscopy of (E)- and (Z)-PVN were characterized using LIF and DFL studies. The S_0-S_1 origins for (E)- and (Z)-PVN have been identified at 33,827 cm^{-1} and 33,707 cm^{-1}, respectively. (E)-PVN displays extensive Duschinsky mixing in its four lowest frequency out-of plane modes $\nu_{42\text{-}45}$, the assignment of which was greatly facilitated via DFL studies from hot bands. DFL spectra from the higher energy portion of the excitation spectrum show evidence for an intermediate regime of IVR onset, where some transitions are found to couple more efficiently to background states than others, resulting in varying degrees of IVR. UV-UV HB and UVD depletion spectra have been collected for (E)-PVN, and they demonstrate the onset of non-radiative processes from

1,600 cm^{-1} above the S_0-S_1 origin. In stark contrast to (E)-PVN, results from the characterization of (Z)-PVN indicate Duschinsky mixing is minimal. Both (E)- and (Z)-PVN are similar in their spectroscopy to their respective ethynyl counterparts, (E)- and (Z)-PVA.

Photochemical studies of (E)- and (Z)-PVN were also carried out in this work via R2PI, UVHF spectroscopy, and 2D timing diagrams. UVHF studies demonstrated facile (E)↔(Z)-PVN isomerization. Photoexcitation of (E)- and (Z)-PVN failed to produce quinoline on the microsecond timescale of our experiment. The characterization of (E)- and (Z)-PVN provide the UV spectral signatures for these molecules, which can be used to conduct and monitor other photochemical experiments where these molecules are thought to play a role, as well as probe for their presence in planetary atmospheres.

5.6. References

1. Cable, M.L., et al., Chem. Rev., 2012. **112** (3): p. 1882-1909.
2. Kasting, J., Science, 1993. **259** (5097): p. 920-926.
3. Raulin, F., et al., Chem. Soc. Rev., 2012. **41** (16): p. 5380-5393.
4. Kemsley, Y., Chemical & Engineering News Archive, 2007. **85** (20): p. 11.
5. Waite, J.H., et al., Science, 2007. **316** (5826): p. 870-875.
6. Cable, M.L., et al., Chem. Rev., 2012. **112** (3): p. 1882-1909.
7. Raulin, F., Space Sci. Rev., 2008. **135** (1-4): p. 37-48.
8. Krasnopolsky, V.A., Icarus, 2009. **201** (1): p. 226-256.
9. Yung, Y.L., Icarus, 1987. **72**: p. 468-472.
10. Seebach, D. and J. Gardiner, Accounts of Chemical Research, 2008. **41** (10): p. 1366–1375.
11. Liu, C.P., et al., J. Phys. Chem. A, 2008. **112** (39): p. 9454-9466.
12. Newby, J.J., et al., J. Phys. Chem. A, 2010. **114** (9): p. 3190-3198.
13. Newby, J.J., et al., J. Am. Chem. Soc., 2010. **132** (5): p. 1611-1620.
14. Muller, C.W., et al., Physical Chemistry Chemical Physics, 2010. **12** (10): p. 2331-2343.
15. Wiley, W.C. and I.H. McLaren, Rev. Sci. Instrum., 1955. **26** (12): p. 1150-1157.
16. Newby, J.J., et al., J. Phys. Chem. A, 2007. **111** (43): p. 10914-10927.
17. Stearns, J.A., et al., Physical Chemistry Chemical Physics, 2006. **8** (45): p. 5317-5327.
18. Dian, B.C., J.R. Clarkson, and T.S. Zwier, Science, 2004. **303** (5661): p. 1169-1173.

19. Gaussian 09, R.B., D.01, M. J. Frisch, G. W. Trucks, H. B. Schlegel, G. E. Scuseria, M. A. Robb, J. R. Cheeseman, G. Scalmani, V. Barone, B. Mennucci, G. A. Petersson, H. Nakatsuji, M. Caricato, X. Li, H. P. Hratchian, A. F. Izmaylov, J. Bloino, G. Zheng, J. L. Sonnenberg, M. Hada, M. Ehara, K. Toyota, R. Fukuda, J. Hasegawa, M. Ishida, T. Nakajima, Y. Honda, O. Kitao, H. Nakai, T. Vreven, J. A. Montgomery, Jr., J. E. Peralta, F. Ogliaro, M. Bearpark, J. J. Heyd, E. Brothers, K. N. Kudin, V. N. Staroverov, T. Keith, R. Kobayashi, J. Normand, K. Raghavachari, A. Rendell, J. C. Burant, S. S. Iyengar, J. Tomasi, M. Cossi, N. Rega, J. M. Millam, M. Klene, J. E. Knox, J. B. Cross, V. Bakken, C. Adamo, J. Jaramillo, R. Gomperts, R. E. Stratmann, O. Yazyev, A. J. Austin, R. Cammi, C. Pomelli, J. W. Ochterski, R. L. Martin, K. Morokuma, V. G. Zakrzewski, G. A. Voth, P. Salvador, J. J. Dannenberg, S. Dapprich, A. D. Daniels, O. Farkas, J. B. Foresman, J. V. Ortiz, J. Cioslowski, and D. J. Fox, Gaussian, Inc., Wallingford CT, 2010, 2013.

20. Zhurko, G.A. *Chemcraft*. http://www.chemcraftprog.com; 1.6:[Available from: http://www.chemcraftprog.com.

21. Hratchian, H.P. and H.B. Schlegel, J. Chem. Phys., 2004. **120** (21): p. 9918-9924.

22. Hratchian, H.P. and H.B. Schlegel, *Chapter 10 - Finding minima, transition states, and following reaction pathways on ab initio potential energy surfaces*, in *Theory and Applications of Computational Chemistry*, C.E.D.F.S.K.E. Scuseria, Editor 2005, Elsevier: Amsterdam. p. 195-249.

23. Hratchian, H.P. and H.B. Schlegel, Journal of Chemical Theory and Computation, 2005. **1** (1): p. 61-69.

24. Baboul, A.G., et al., J. Chem. Phys., 1999. **110** (16): p. 7650-7657.

25. Mulliken, R.S., J. Chem. Phys., 1955. **23** (11): p. 1997-2011.

26. Varsanyi, G., *Assignments for Vibrational Spectra of 700 Benzene Derivatives*1974, New York: Wiley.

27. Duschinsky, F., Acta Physicochimica Urss, 1937. **7** (4): p. 551-566.

28. English translation of the original article by F. Duschinsky (translated by C. W. Mueller), available from http://www.chem.purdue.edu.edu/zwier/pubs/Duschinsky.pdf.

29. Hiraya, A., et al., J. Chem. Phys., 1984. **81** (7): p. 3345-3347.

30. Small, G.J., J. Chem. Phys., 1971. **54** (8): p. 3300-&.

31. Kobayashi, T., et al., J. Chem. Phys., 1987. **86** (3): p. 1111-1117.

32. Powers, D.E., J.B. Hopkins, and R.E. Smalley, J. Chem. Phys., 1981. **74** (11): p. 5971-5976.

33. Landera, A. and A.M. Mebel, J. Am. Chem. Soc., 2013. **135** (19): p. 7251-7263.

34. Lin, M.F., et al., J. Chem. Phys., 2005. **123** (5).

35. Houston, P.L., in *Chemical Kinetics and Reaction Dynamics*, 2006, Dover Publications, Inc.: Mineola. p. 233-239.

CHAPTER 6: MICROWAVE SPECTROSCOPY OF ASTROCHEMICALLY RELEVANT MOLECULES: 4-PENTENENITRILE, 4-PENTYNENITRILE, AND GLUTARONITRILE

6.1. Introduction

Nitriles and isonitriles are important organic functionalities in molecules found throughout space. Of the 180 plus molecules that have been identified in the interstellar medium and circumstellar shells, at least 66 contain nitrogen.[1-3] Many of these nitrogen-containing molecules are nitriles and isonitriles, and their identification has oftentimes been facilitated via rotational spectroscopy.[1-3]

An important attribute of nitriles/isonitriles that facilitate their detection via rotational spectroscopy is their large dipole moments. For example, the prototypical nitrile/isonitrile HCN and HNC have dipole moments of 2.98 and 3.05 D, respectively.[4,5] Since the intensity of a rotational transition is proportional to the modulus squared of the dipole moment,[6] nitriles and isonitriles are ideal molecules for microwave-based detection, provided that a permanent dipole exists. The high resolution afforded by rotational spectroscopy is also advantageous for its ability to firmly identify these molecules in space.

Apart from circumstellar and interstellar regions, nitriles and isontriles are also important molecules in planetary bodies where the atmospheres are nitrogen-rich. A prime example of a nitrogen-rich planetary body is Titan, a moon of Saturn. Titan is considered a model system for the study of primordial Earth, and its atmosphere is comprised of about 95% or more of N_2.[7-9] The next most abundant species in Titan's atmosphere is CH_4, and when combined, the photochemistry of N_2 and CH_4 lead to a rich variety of organic molecules ranging from small hydrocarbons, nitriles/isonitriles, and benzene, to tholins, a large aerosol-like substance that envelops the atmosphere.[8, 10] This

complex chemistry occurs via ion and neutral reactions,[11-16] and in the case of neutrals, resonance-stabilized radicals (RSRs)[17-19] are thought to be important candidates in pathways leading to the formation of larger molecules.

The search for molecules in space relies heavily on laboratory data that establish spectral signatures for key candidate molecules. In some cases, however, such laboratory data is not yet available. To this end, this work characterizes the microwave spectroscopy of three molecules that are thought to be prime candidates for detection in planetary atmospheres and elsewhere in space: 4-pentenenitrile, 4-pentynenitrile, and glutaronitrile.

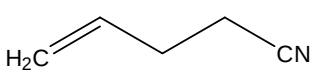

4-pentenenitrile

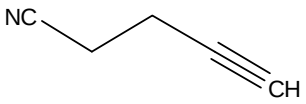

4-pentynenitrile

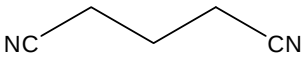

glutaronitrile

4-pentenenitrile represents an important recombination product of the allyl and cyanomethyl radicals, which are both RSRs.[19, 20] The ability of RSRs to adopt multiple resonance structures makes them more stable relative to other radical species, and consequently, RSRs can build up in concentration.[19] Therefore, radical recombination reactions involving two RSRs are likely to constitute significant pathways towards the formation of more complex radicals in space. As such, it is particularly important to study not only these RSR species, but also the candidate end products of their reaction, so that these molecules can be identified in space. The microwave spectroscopy of 4-pentenenitrile provides the characterization of one such likely RSR recombination product.

In a similar way, 4-pentynenitrile is the anticipated product of propargyl and cyanomethyl RSR recombination. Furthermore, 4-pentynenitrile shares the same molecular formula as pyridine (C_5H_5N), the simplest nitrogen heterocycle. Studying the formation pathways to nitrogen heterocycles may be key to understanding how Earth's first biomolecules may have formed, since many of them contain nitrogen in ring

structures.[21] Thus we characterize 4-pentynenitrile not only to provide spectral signatures for its search in space, but also as a first step towards photochemical studies of 4-pentynenitrile + hν → pyridine isomerization.

Glutaronitrile is an interesting long-chain dinitrile that has an intriguing conformational landscape, and it may be formed upon the reaction of the cyanomethyl and cyanoethyl radicals. All three of these molecules have been formed in Titan tholin simulation experiments, albeit in small quantities due to a rich mixture of reaction products formed.[22, 23] By providing the spectral signatures of these molecules, we hope to lay the foundation for photochemical experiments as well as enable the search for these molecules in Titan's atmosphere, as well as in space.

6.2. Methods

6.2.1. Experimental Methods

Samples of 4-pentenenitrile (97% purity), 4-pentynenitrile (97%), and glutaronitrile (99%) were purchased from Sigma-Aldrich and used without further purification. 4-pentenenitrile, 4-pentynenitrile, and glutaronitrile were heated to 70 ˚C, 50 ˚C, and 150 ˚C respectively. All samples were entrained in a total of 1.4 bar backing pressure Ar and expanded through a 1 mm orifice general valve to generate a supersonic expansion and cool the molecules down to the zero-point level.

A broadband chirped pulse Fourier transform microwave (CP-FTMW)[24] spectrometer was used to study the rotational spectroscopy of these molecules. Two detection schemes were used to collect their microwave spectra. The setup of the traditional CP-FTMW spectrometer has been described in detail elsewhere[25] and in Chapter 2 of this thesis, and therefore will only be described briefly here. A 7.5 to 18.5 GHz chirped pulse is generated from a combination of an arbitrary waveform generator and microwave electronics. The supersonically cooled molecules are exposed to this 7.5 - 18.5 GHz polarizing pulse (1 μs) and undergo a free induction decay (FID). In the

traditional detection setup, the molecular signals are down-converted by mixing with an 18.9 GHz local oscillator, and the signals are monitored with a 12 GHz, 40 Gs/s oscilloscope. With the new detection setup, the down-converted molecular signals are collected with a fast digitizer. The principal advantage of this fast digitizer is that it allows multi-FID detection, with the ability to collect up to 20 FIDs per gas pulse. This requires generation of a series of 20 chirped pulses, with the beginning of each consecutive chirp separated by 50 μs, and their detection via segmented averaging in the Guzik digitizer. This greatly improves the rate at which signal averaging can be accomplished. However, the fast digitizer does not allow for the monitoring of frequency domain data in real-time, a task which is possible with the traditional detector setup. Thus, the traditional setup is a useful tool to optimize molecular transitions in real-time, and the digitizer is invaluable in providing efficient data averaging and collection.

For each molecules studied in this work, a 4 μs long FID was detected. One million averages were collected and corresponding background spectra were collected for the three molecules, in order to help identify and remove noise peaks in the raw microwave data. These background noise peaks are from narrow resonances produced by reflections of the chirped pulses in the stainless steel vacuum chamber. Their frequencies and amplitudes are sensitive to the exact position of the pulsed valve assembly in the vacuum chamber. An additional source of noise is from electrical components. These background noise peaks are independent of the presence of the gas pulse, and can thus be identified through a spectrum acquired without gas pulses present. Their narrow width makes them difficult to distinguish from molecular resonances, but also minimizes their overlap with molecular signals. As a means of ensuring that molecular resonances are not removed from consideration by an automated process, the spectra were manually processed for the removal of these background noise peaks.

6.2.2. Computational Methods

Stable conformations with energies less than 50 kJ/mol were identified by running Amber force field calculations via MacroModel[26] (10,000 iterations, 0.0001 convergence

threshold). Five stable conformations for 4-pentenenitrile, two stable conformations of 4-pentynenitrile, and four stable conformations of glutaronitrile were found in the initial force field search. Gaussian 09[27] was used to optimize these structures and calculate harmonic vibrational frequencies (for zero-point correction) with the M052X functional and 6-31+G(d) basis set. Optimized structures within 500 cm^{-1} of the global minimum were considered during the assignment process.

6.3. Results

6.3.1. 4-Pentenenitrile

6.3.1.1. Theoretical Predictions

Five conformations of 4-pentenenitrile were predicted to have relative energies within 500 cm^{-1} of the global minimum at the M052X/6-31+G(d) level of theory. The five structures of 4-pentenenitrile are presented in Figure 6.1.

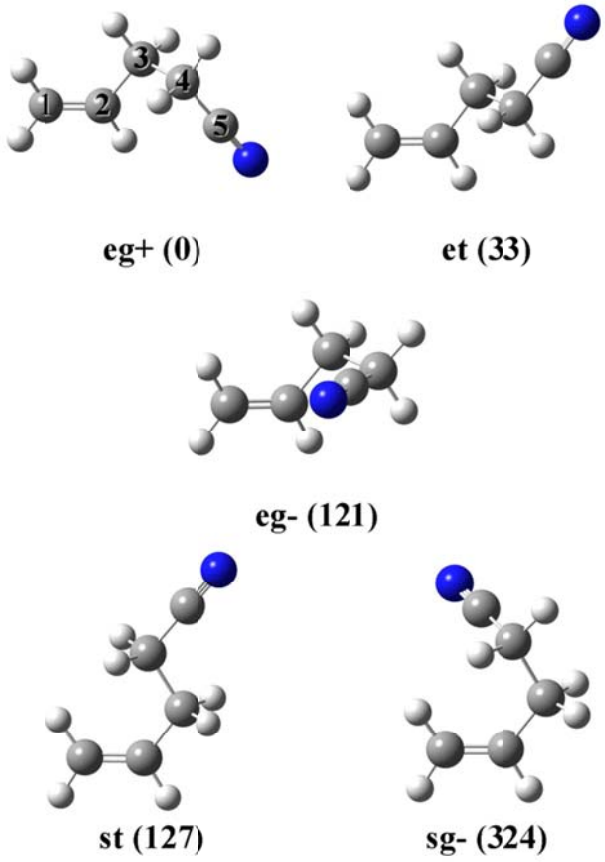

Figure 6.1. Five most stable conformations of 4-pentenenitrile calculated at the M052X/6-31+G(d) level of theory. See **t**ext for details on nomenclature of conformations. Zero-point corrected M052X/6-31+G(d) relative energies (cm^{-1}) are included in parentheses next to each structure.

There are two dihedral angles, ∠ C1-C2-C3-C4 and ∠ C2-C3-C4-C5, that lead to the various conformations of 4-pentenenitrile, the atom numbering of which is defined in the eg+ structure of Figure 6.1. Structures are labeled by the letters e, s, t, and g, representing **e**clipsed, **s**yn, **t**rans, and **g**auche respectively. Eclipsed structures contain a dihedral angle that is near 120.0 ˚ (± 7.0 ˚), syn structures (which are a special eclipsed case) contain a dihedral angle of 0.0 ˚, and trans structures contain a dihedral angle of 180.0 ˚ (± 2.0 ˚). Gauche structures contain a dihedral angle that is nominally 60.0 ˚ (± 8.0) in magnitude, with + and - denoting **p**ositive and negative dihedral angles,

respectively. Names are ascribed by listing the type of the dihedral angle connecting C1-C2-C3-C4 followed by the type of the dihedral angle connecting C2-C3-C4-C5. For example, the structure labeled eg+ consists of a C1-C2-C3-C4 dihedral angle of 118.2 ° which is eclipsed (e), and a C2-C3-C4-C5 dihedral angle of +61.6 ° (g+). Table 6.1 provides the predicted properties of the 4-pentenenitrile structures. In all cases, the structures of 4-pentenenitrile are all near prolate asymmetric rotors.

Table 6.1. Summary of predicted properties for 4-pentenenitrile.

	4-pentenenitrile structures[a]				
	eg+	et	eg-	st	sg-
A (MHz)	8,164	17,578	5,760	14,869	5,928
B (MHz)	1,973	1,431	2,523	1,606	2,604
C (MHz)	1,712	1,405	1,909	1,476	2,046
∠ C1-C2-C3-C4	118.2	116.9	113.2	0.0	0.0
∠ C2-C3-C4-C5	61.6	178.0	-65.1	180.0	-68.0
κ[b]	-0.92	-1.00	-0.68	-0.98	-0.71
$\lvert\mu_a\rvert$[c] (D)	2.8	3.9	2.3	4.0	-2.9
$\lvert\mu_b\rvert$[c] (D)	2.9	1.3	3.4	0.4	2.8
$\lvert\mu_c\rvert$[c] (D)	0.5	0.1	-0.2	0.0	1.1
$\lvert\mu_T\rvert$[c] (D)	4.1	4.1	4.1	4.0	4.2
χ_{aa}[d] (MHz)	0.35	2.93	-1.07	3.56	0.16
χ_{bb}[d] (MHz)	1.37	-1.14	2.93	-1.69	0.90
χ_{cc}[d] (MHz)	-1.72	-1.79	-1.86	-1.87	-1.06
ΔE[e] (cm^{-1})	0	33	121	127	324

[a] M052X/6-31+G(d)
[b] Ray's asymmetry parameter, $\kappa = (2B - A - C) / (A - C)$
[c] $|\mu_a|$, $|\mu_b|$, $|\mu_c|$, and $|\mu_T|$ are the absolute values of the dipole moment components along the a, b, and c axes, and the total dipole moment.
[d] χ_{aa}, χ_{bb}, and χ_{cc} are ^{14}N nuclear quadrupole coupling constants.
[e] M052X/6-31+G(d) relative energies including zero-point correction.

6.3.1.2. Microwave Spectrum

Figure 6.2a shows the total experimental microwave spectrum of 4-pentenenitrile over the 7.5 - 18.5 GHz region. The spectrum shows moderate congestion, suggesting the potential for the presence of multiple conformations. *Ab initio* calculations were used to

predict the unique rotational constants associated with each conformational isomer, and JB95[28] was used to simulate a microwave spectrum of each conformation via the rigid rotor approximation. Once a simulation was generated for each conformation, the experimental peaks were fit in order to determine the assignments for the various structures. From this process, the eg+, et, and st conformations of 4-pentenenitrile were found in the experimental spectrum (Figure 6.2b). Table 6.2 provides a summary of results from the fit.

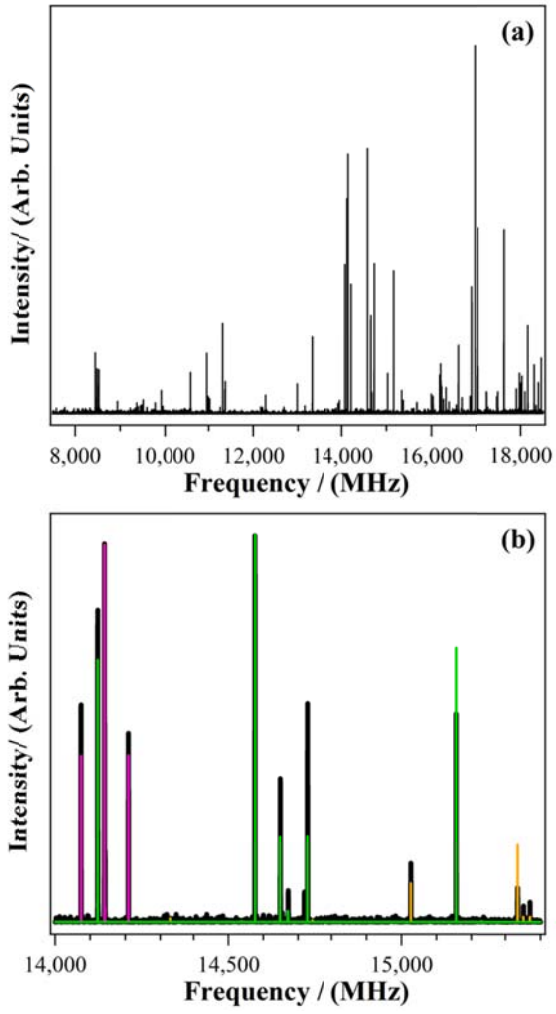

Figure 6.2. (a) Total experimental microwave spectrum of 4-pentenenitrile from 7.5 - 18.5 GHz. (b) Magnified view experimental microwave spectrum of 4-pentenenitrile (black trace) from 14,000 - 15,400 MHz. The simulated spectra for the eg+, et, and st structures are overlaid in green, magenta, and orange, respectively.

Table 6.2. Experimental rotational constants for observed conformations of 4-pentenenitrile

	4-pentenenitrile structures		
	eg+	et	st
A (MHz)	8,210.562	[17,578.289][a]	[14868.640][a]
B (MHz)	1,961.225	1,427.654	1,599.922
C (MHz)	1,702.378	1,400.662	1,470.762

[a] Fixed to the *ab initio* (M052X/6-31+G(d)) value. See text for details.

For the et and st structures, it was only possible to assign a-type transitions. Since there is little dependence of a-type transitions on the A rotational constant for low J values, it was not possible to obtain a reliable fit for the A rotational constant. The B and C rotational constants of et and st 4-pentenenitrile were fit, while fixing the A rotational constant to the *ab initio* predicted value. A total of 21, 16, and 8 lines were fit for the eg+, et, and st structures, respectively. A summary of the assigned transitions is provided in Table 6.3.

Due to the presence of a nitrogen atom in the structure of 4-pentenenitrile, a careful search for ^{14}N nuclear quadrupole splittings was conducted. Nuclear quadruple splittings occur due to the coupling of the nuclear spin angular momentum (**I**) to the rotational angular momentum of the molecule (**J**).[29] The coupling of **I** and **J** arises out of the interaction of their magnetic fields, which are induced via the movement of atomic and molecular charge.[29] The total angular momentum of the molecule is described by **F**, where $\mathbf{F} = \mathbf{I} + \mathbf{J}$.[29] Atoms with a nuclear spin quantum number I larger than 1/2 will have a electric quadrupole moment (and an associated magnetic moment), which can interact with the electric (magnetic) field of the surrounding molecule, leading to nuclear quadrupole splittings.[29] I is 1 for ^{14}N, and therefore there is a potential to observe nuclear quadrupole hyperfine splittings.[29] Transitions where ΔJ and ΔF are equal are generally more intense, and when there are multiple splittings where $\Delta J = \Delta F$, the transition with higher value of F will be more intense.[29] For a couple of transitions, hints of nuclear

quadrupole splitting were observed; however the nuclear quadrupole splittings were primarily too small to be resolved and it was not possible to conduct a fit to determine experimental values for the nuclear quadrupole coupling constants. The theoretical nuclear quadrupole coupling constants (Table 6.1) and experimental rotational constants (Table 6.2) were put into the SPCAT program[30] to predict hyperfine splittings for experimentally observed transitions in each of the structures. The prediction results indicated average quadrupole splittings of 0.29, 0.13, and 0.12 MHz for the most intense splitting transitions of eg+, et, and st. The resolution bandwidth of the processed data for a 10 μs FID is 172 kHz,[31] and since the resolution bandwidth is inversely proportional to the FID collection time, the resolution bandwidth associated with the 4 μs FIDs collected in this work is higher, explaining why it is difficult to resolve the predicted nuclear quadrupole splittings of 0.29, 0.13, and 0.12 MHz.

The experimental observation of the eg+, et, and st structures of 4-pentenenitrile are in accordance with the theoretical predictions, since they are low energy structures. However, the absence of an assignment for the eg- structure is surprising, since the M052X/6-31+G(d) level of theory predicts this conformation to be only 121 cm^{-1} above the global minimum eg+ structure, and just 6 cm^{-1} below the st structure, which was observed experimentally. The energies predicted by these calculations may be sensitive to the level of theory utilized. In addition, inaccuracies in the calculated low frequency modes could affect the zero-point energy corrections. An alternative possibility, is that the absence of the eg- conformation could occur if collisional cooling over a small energy barrier led to removal of population from this minimum in the supersonic expansion. To test this possibility, potential energy scans from eg- to eg+ and et were calculated with M052X/6-31+G(d). However, the barriers in going from eg- to eg+ and eg- to et were found to be prohibitively high, at 1,427 and 1,117 cm^{-1}, respectively, suggesting that collision-induced isomerization is not likely to occur.

Table 6.3. Summary of assigned transitions for 4-pentenenitrile

4-pentenenitrile structures								
eg+			et			st		
ν_{obs} (MHz)	Assignment ($J'_{Ka'Kc'}$-$J''_{Ka''Kc''}$)	OMC[a] (MHz)	ν_{obs} (MHz)	Assignment ($J'_{Ka'Kc'}$-$J''_{Ka''Kc''}$)	OMC[a] (MHz)	ν_{obs} (MHz)	Assignment ($J'_{Ka'Kc'}$-$J''_{Ka''Kc''}$)	OMC[a] (MHz)
7,319.369	2_{02}-1_{01}	0.039	8,444.401	3_{13}-2_{12}	-0.039	12,273.369	4_{04}-3_{03}	0.015
7,769.580	4_{13}-4_{04}	0.147	8,484.760	3_{03}-2_{02}	-0.053	15,026.476	5_{15}-4_{14}	0.019
8,535.954	5_{14}-5_{05}	0.112	8,525.387	3_{12}-2_{11}	-0.028	15,334.666	5_{05}-4_{04}	0.000
8,939.320	4_{04}-3_{13}	-0.074	11,259.116	4_{14}-3_{13}	-0.097	15,351.413	5_{24}-4_{23}	0.080
9,512.860	6_{15}-6_{06}	-0.169	11,312.789	4_{04}-3_{03}	-0.137	15,370.105	5_{23}-4_{22}	0.019
9,912.794	1_{11}-0_{00}	-0.147	11,367.148	4_{13}-3_{12}	-0.031	15,672.153	5_{14}-4_{13}	-0.016
10,597.799	3_{13}-2_{12}	0.110	14,073.869	5_{15}-4_{14}	-0.084	18,029.218	6_{16}-5_{15}	-0.015
10,959.281	3_{03}-2_{02}	-0.075	14,140.665	5_{05}-4_{04}	-0.240	18,391.233	6_{06}-5_{05}	-0.081
10,991.171	3_{22}-2_{21}	0.362	14,141.847	5_{24}-4_{23}	0.342			
11,022.605	3_{21}-2_{20}	0.342	14,142.496	5_{23}-4_{22}	0.315			
11,374.015	3_{12}-2_{11}	-0.065	14,208.795	5_{14}-4_{13}	-0.116			
13,317.681	2_{12}-1_{01}	-0.015	16,888.508	6_{16}-5_{15}	-0.143			
14,121.439	4_{14}-3_{13}	0.031	16,968.388	6_{06}-5_{05}	-0.325			
14,575.884	4_{04}-3_{03}	-0.210	16,970.143	6_{25}-5_{24}	0.399			
14,726.984	4_{22}-3_{21}	0.383	16,971.249	6_{24}-5_{23}	0.322			
15,155.680	4_{13}-3_{12}	-0.216	17,050.404	6_{15}-5_{14}	-0.196			
16,596.226	3_{13}-2_{02}	0.171						
17,501.493	5_{23}-5_{14}	-0.051						
17,637.868	5_{15}-4_{14}	-0.114						
18,162.199	5_{05}-4_{04}	-0.468						
18,456.007	5_{23}-4_{22}	0.163						

[a] OMC = ν_{obs} - ν_{calc}

6.3.2. 4-Pentynenitrile

6.3.2.1. Theoretical Predictions

Two structures of 4-pentynenitrile, *trans* and *gauche*, are predicted to be within 500 cm^{-1} of each other at the M052X/6-31+G(d) level of theory (Figure 6.3). The conformational variability between these two low energy structures arises from the rotation along the central C-C bond of the H_2C-CH_2 unit bridging the cyano and ethynyl substituents. In the *trans* structure, the cyano and ethynyl substituents are nominally 180 ˚ from each other and in the *gauche* structure, the cyano and ethynyl substituents are rotated about 60 ˚ from each other, with respect to the central C-C bond. A summary of the predicted properties for 4-pentynenitrile is presented in Table 6.4.

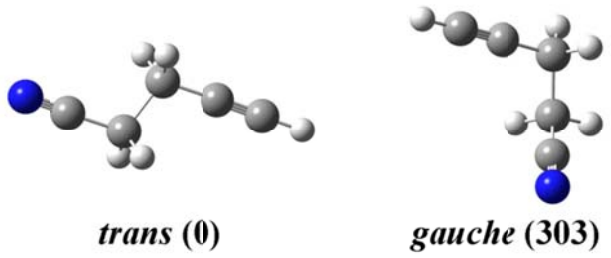

Figure 6.3. Two most stable conformations of 4-pentynenitrile calculated at the M052X/6-31+G(d) level of theory. Zero-point corrected M052X/6-31+G(d) relative energies (cm^{-1}) are included in parentheses next to each structure.

Table 6.4. Summary of predicted properties of 4-pentynenitrile

	4-pentynenitrile structures[a]	
	trans	gauche
A (MHz)	25,236	6,550
B (MHz)	1,475	2,414
C (MHz)	1,418	1,894
κ[b]	-1.00	-0.78
$\lvert\mu_a\rvert$ (D)	3.5	2.2
$\lvert\mu_b\rvert$ (D)	0.9	3.4
$\lvert\mu_c\rvert$ (D)	0.0	0.8
$\lvert\mu_T\rvert$ (D)	3.6	4.1
χ_{aa} (MHz)	3.33	-0.48
χ_{bb} (MHz)	-1.48	2.02
χ_{cc} (MHz)	-1.85	-1.54
ΔE (cm^{-1})	0	303

[a] M052X/6-31+G(d)
[b] Ray's asymmetry parameter, $\kappa = (2B - A - C) / (A - C)$
[c] $\lvert\mu_a\rvert$, $\lvert\mu_b\rvert$, $\lvert\mu_c\rvert$, and $\lvert\mu_T\rvert$ are the absolute values of the dipole moment components along the a, b, and c axes, and the total dipole moment.
[d] χ_{aa}, χ_{bb}, and χ_{cc} are ^{14}N nuclear quadrupole coupling constants.
[e] M052X/6-31+G(d) relative energies including zero-point correction.

6.3.2.2. Microwave Spectrum

Figure 6.4 shows the experimental microwave spectrum of 4-pentynenitrile over the 7.5 to 18.5 GHz region. Following an analogous fitting process to that of 4-pentenenitrile, the *trans* conformation of 4-pentynenitrile was fit. During the fitting process, 15 purely a-type transitions could be fit for the *trans* conformer, and therefore an experimental value for the A rotational constant could not be derived. A summary of the experimentally determined rotational constants is presented in Table 6.5.

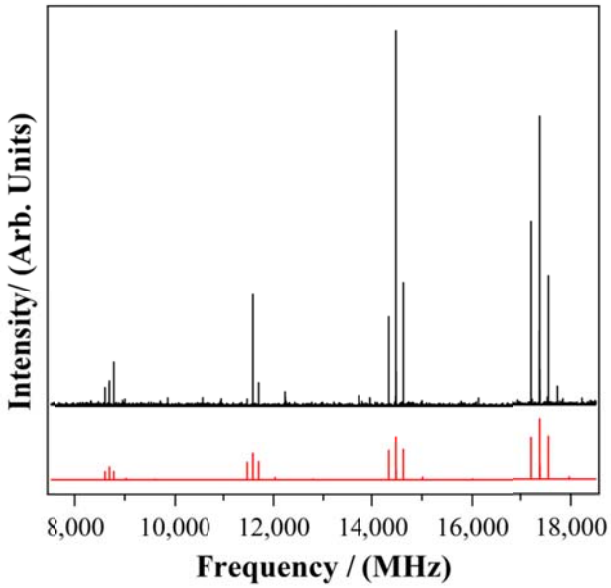

Figure 6.4. Total experimental microwave spectrum of 4-pentynenitrile from 7.5 - 18.5 GHz (black trace). The simulated spectrum of *trans* 4-pentynenitrile is presented in red, below the experimental rotational spectrum.

Table 6.5. Experimental rotational constants for trans 4-pentynenitrile

	4-pentynenitrile
	trans
A (MHz)	[25,236.218][a]
B (MHz)	1,477.087
C (MHz)	1,419.382

[a] Fixed to the *ab initio* (M052X/6-31+G(d)) value. See text for details.

Once again, no clearly identifiable nuclear quadrupole splittings were observed in the experimental spectra. An SPCAT prediction based on the calculated nuclear quadrupole coupling constants and experimental rotational constants resulted in an average predicted splitting of 0.19 MHz for the most intense hyperfine splitting components of experimentally observed transitions, which could not be resolved. Table

6.6 lists a summary of the assigned transitions of *trans* 4-pentynenitrile. Despite searches, no assignment for the *gauche* structure of 4-pentynenitrile could be determined.

Table 6.6. Summary of assigned transitions of 4-pentynenitrile

4-pentynenitrile		
trans		
	Assignment	
ν_{obs} (MHz)	($J'_{Ka'Kc'}$-$J''_{Ka''Kc''}$)	OMC[a] (MHz)
8,602.787	3_{13}-2_{12}	0.002
8,688.999	3_{03}-2_{02}	0.011
8,775.898	3_{12}-2_{11}	-0.002
11,470.107	4_{14}-3_{13}	-0.151
11,584.815	4_{04}-3_{03}	-0.013
11,585.740	4_{23}-3_{22}	-0.056
11,586.822	4_{22}-3_{21}	-0.024
11,701.202	4_{13}-3_{12}	0.124
14,337.694	5_{15}-4_{14}	0.067
14,480.173	5_{05}-4_{04}	-0.075
14,484.522	5_{23}-4_{22}	0.308
14,626.124	5_{14}-4_{13}	-0.026
17,204.900	6_{16}-5_{15}	0.035
17,375.035	6_{06}-5_{05}	-0.108
17,551.007	6_{15}-5_{14}	-0.082

[a] OMC = ν_{obs} - ν_{calc}

6.3.3. Glutaronitrile

6.3.3.1. Theoretical Predictions

Two conformations of glutaronitrile (gg and gt) were calculated to be the lowest energy structures, within the 500 cm^{-1} cutoff after optimization at the M052X/6-31+G(d) level. These structures are presented in Figure 6.5, and the differences between them can be understood by the dihedral angles made up by C1-C2-C3-C4 and C2-C3-C4-C5, which are labeled in the gg structure of Figure 6.5. Structures are labeled by the letters g and t, representing **g**auche and **t**rans. Gauche structures contain a dihedral angle that is nominally 60.0 ˚ (± 1.3), and trans structures contain a dihedral angle of 180.0 ˚ (± 3.2 ˚). Names are derived by listing the type of the dihedral angle connecting C1-C2-C3-C4 followed by the type of the dihedral angle connecting C2-C3-C4-C5. For example, the structure labeled gg consists of a C1-C2-C3-C4 dihedral angle of 61.3 ˚ which is gauche (g), and a C2-C3-C4-C5 dihedral angle of 61.2 ˚, which is also gauche (g).

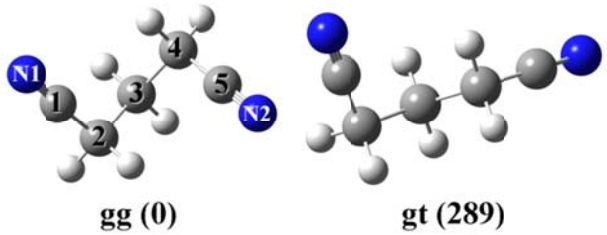

Figure 6.5. Two most stable conformations of glutaronitrile calculated at the M052X/6-31+G(d) level of theory. Zero-point corrected M052X/6-31+G(d) relative energies (cm^{-1}) are included in parentheses next to each structure.

In addition to the gg and gt structures of glutaronitrile, two additional structures, tt and g+g-, were found in the initial MacroModel force field search to have predicted energies below 50 kJ/mol of the global minimum. In the tt structure, the dihedral angles C1-C2-C3-C4 and C2-C3-C4-C5 are both nominally 180 ˚, with the long dinitrile chain

fully extended such that many atoms overlap (eclipse) each other. In the g+g- structure, the dihedral angles C1-C2-C3-C4 and C2-C3-C4-C5 are approximately +61 ˚ and -61˚, and the atoms are completely eclipsed with respect to each other with the exception of the central CH_2 group (of atom 3). The tt and g+g- structures are calculated to be 641 and 1,464 cm^{-1} higher in energy than the global minimum with M052X/6-31+G(d). The higher energy of the tt and g+g- structures may be due to the increase in unfavorable steric interactions associated with the overlap (eclipse) of many atoms within the structures.

M052X/6-31+G(d) was used to calculated the properties of the lowest energy conformations of glutaronitrile, gg and gt. Table 6.7 summarizes the predicted properties of these glutaronitrile structures.

Table 6.7. Predicted properties for the candidate glutaronitrile structures

	glutaronitrile structures[a]	
	gg	gt
A (MHz)	4,714	7,389
B (MHz)	1,599	1,209
C (MHz)	1,462	1,091
∠ C1-C2-C3-C4	61.3	59.3
∠ C2-C3-C4-C5	61.2	176.8
κ[b]	-0.92	-0.96
$\lvert\mu_a\rvert$[c] (D)	0.0	1.8
$\lvert\mu_b\rvert$[c] (D)	4.6	3.7
$\lvert\mu_c\rvert$[c] (D)	0.0	1.3
$\lvert\mu_T\rvert$[c] (D)	4.6	4.3
χ_{aa}[d] (MHz), N1	0.19	-0.66
χ_{bb}[d] (MHz), N1	-0.08	2.42
χ_{cc}[d] (MHz), N1	-0.11	-1.77
χ_{aa}[d] (MHz), N2	0.19	3.41
χ_{bb}[d] (MHz), N2	-0.08	-1.92
χ_{cc}[d] (MHz), N2	-0.11	-1.49
ΔE[e] (cm^{-1})	0	289

[a] M052X/6-31+G(d)
[b] Ray's asymmetry parameter, $\kappa = (2B - A - C) / (A - C)$
[c] $|\mu_a|$, $|\mu_b|$, $|\mu_c|$, and $|\mu_T|$ are the absolute values of the dipole moment components along the a, b, and c axes, and the total dipole moment.
[d] χ_{aa}, χ_{bb},, and χ_{cc} are ^{14}N nuclear quadrupole coupling constants, for N1 and N2.
[e] M052X/6-31+G(d) relative energies including zero-point correction.

6.3.3.2. Microwave Spectrum

Figure 6.6a shows the experimental microwave spectrum of glutaronitrile over the 7.5 to 18.5 GHz region. Following an analogous fitting process to the molecules described above, a fit for the gg structure of glutaronitrile was found. Since this structure is calculated to have its dipole moment exclusively along the 'b' rotational axis, its spectrum is predicted to be composed purely of b-type transitions. Indeed, during the

fitting process, 33 purely b-type transitions were assigned for the gg structure, with centrifugal distortion corrections increasing the accuracy of the fit. A summary of the experimentally determined rotational constants and centrifugal distortion constants is presented in Table 6.8.

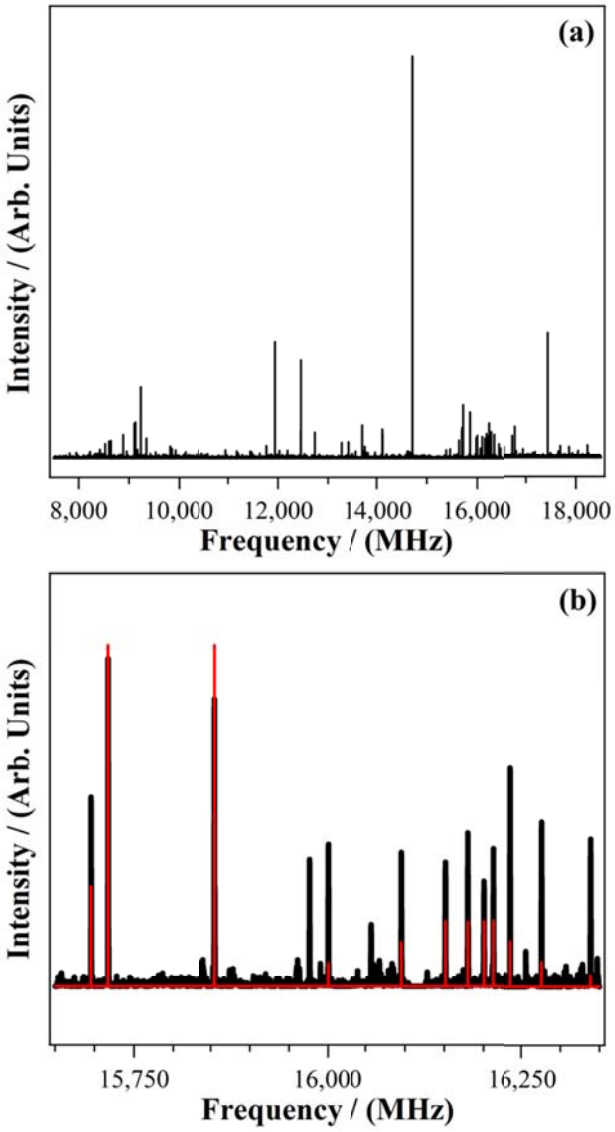

Figure 6.6. (a) Overview experimental microwave spectrum of glutaronitrile from 7.5 - 18.5 GHz. (b) Magnified view experimental microwave spectrum of glutaronitrile (black trace) from 15,650 - 16,350 MHz. The simulated spectrum for the gg structure is overlaid in red.

Table 6.8. Experimental rotational and centrifugal distortion constants for glutaronitrile

	glutaronitrile
	gg
A (MHz)	4,756.049
B (MHz)	1,582.727
C (MHz)	1,449.369
D_J (kHz)	0.00254
D_{JK} (kHz)	-0.01860
D_K (kHz)	0.04857

Nuclear quadrupole splittings were not resolved in the microwave spectrum of gg glutaronitrile. SPCAT was used to predict nuclear quadrupole hyperfine splittings. Glutaronitrile is unique amongst all of the molecules studied in this work, since it contains two ^{14}N atoms, N1 and N2 (Figure 6.5). Each ^{14}N atom has associated nuclear quadrupole coupling constants χ_{aa} χ_{bb}, and χ_{cc} (Table 6.7), which led to a complex pattern for the nuclear quadrupole splittings. When all splittings (weak and intense) were considered for experimentally observed transitions, the average nuclear quadrupole splitting was predicted to be 0.20 MHz with SPCAT, which could not be resolved in the study. Table 6.9 provides a summary of the assigned transitions of gg glutaronitrile.

It was not possible to assign the gt structure of glutaronitrile. It was possible to assign 16 a-type lines and two b-type lines based on the predicted rotational constants of gt glutaronitrile; however theory predicts that b-type lines should be more intense than a-type lines in the gt structure (Table 6.7), due to a larger component of the dipole moment along the b axis. Upon close inspection, many of the most intense b-type lines were missing from the spectrum, indicating that the fit generated cannot be confidently assigned to the gt glutaronitrile structure. These unassigned transitions are excellent candidates for future studies using two-dimensional CP-FTMW spectroscopy to identify transitions that share rotational energy levels and are thus associated with the same conformation.[32]

Table 6.9. Summary of assigned transitions for gg glutaronitrile

glutaronitrile		
gg		
ν_{obs} (MHz)	Assignment ($J'_{Ka'Kc'}$-$J''_{Ka''Kc''}$)	OMC (MHz)
8,417.850	7_{25}-7_{16}	0.236
8,638.073	6_{24}-6_{15}	0.034
8,880.879	5_{23}-5_{14}	-0.070
9,104.077	2_{12}-1_{01}	-0.060
9,122.807	4_{22}-4_{13}	-0.146
9,228.818	4_{04}-3_{13}	0.122
9,342.954	3_{21}-3_{12}	-0.082
9,523.580	2_{20}-2_{11}	-0.109
9,817.059	6_{15}-5_{24}	-0.076
9,920.003	2_{21}-2_{12}	0.357
10,122.717	3_{22}-3_{13}	0.165
10,394.934	4_{23}-4_{14}	0.424
11,937.484	3_{13}-2_{02}	-0.212
12,190.895	8_{27}-8_{18}	-0.310
12,453.804	5_{05}-4_{14}	0.202
13,273.278	7_{16}-6_{25}	-0.189
14,711.039	4_{14}-3_{03}	-0.248
15,695.613	6_{06}-5_{15}	0.306
15,717.204	2_{21}-1_{10}	0.090
15,854.572	2_{20}-1_{11}	-0.016
16,000.331	6_{33}-6_{24}	0.163
16,095.508	5_{32}-5_{23}	0.033
16,151.432	4_{31}-4_{22}	-0.101
16,179.889	3_{30}-3_{21}	-0.138
16,200.298	3_{31}-3_{22}	-0.201
16,212.353	4_{32}-4_{23}	-0.090
16,235.889	5_{33}-5_{24}	0.043
16,276.058	6_{34}-6_{25}	0.128
16,338.695	7_{35}-7_{26}	0.149
16,430.058	8_{36}-8_{27}	0.080
16,556.515	9_{37}-9_{28}	-0.196
16,775.975	8_{17}-7_{26}	-0.037
17,433.095	5_{15}-4_{04}	-0.188

6.4. Discussion

The microwave spectroscopy of the isonitrile counterparts to 4-pentenenitrile and 4-pentynenitrile have been studied by Møllendal and coworkers.[33, 34] The isocyano analog of 4-pentenenitrile is 4-isocyano-1-butene,[34] and the isocyano counterpart to 4-pentynenitrile is 4-isocyano-1-butyne.[33] These isocyano isomers form interesting points of comparison, because they are isoelectronic structural isomers of the molecules studied in this work. The spectroscopic characterization of these sets of isoelectronic structural isomers is important, because isomers can vary in their reactivity, potentially leading to different reaction products.

First we begin with a comparison between the microwave spectroscopy of 4-pentenenitrile and 4-isocyano-1-butene. In the 4-isocyano-1-butyne study, Møllendal and coworkers observed three stable conformations.[34] A comparison of the dihedral angles of the observed structures of 4-pentenenitrile (eg+, et, and st) and 4-isocyano-1-butene shows that the same stable conformations were observed in both molecules, indicating that the structural preferences are largely independent of whether the terminal groups are nitrile or isonitrile. For example, the eg+, et, and st structures of 4-pentenenitrile correspond to structures III, I, and IV of 4-isocyano-1-butene. In the case of 4-isocyano-1-butene, Møllendal and coworkers also did not observe any nuclear quadrupole splittings, much like the lack of such splittings in this work.

The present microwave data on 4-pentynenitrile can be compared with the gas cell data on 4-isocyano-1-butyne.[33] Møllendal and coworkers observed both the trans and gauche conformations of 4-isocyano-1-butyne.[33] This is in contrast to our work, where no transitions due to the *gauche* conformer could be confidently assigned. The difference in observed conformations is likely explained by the fact that Møllendal and coworkers obtained microwave spectra in a cell cooled to about 253 K,[33] whereas the microwave spectroscopy in this work was carried out under jet-cooled conditions, with rotational temperatures of a few K, where collisional cooling can remove population from higher-lying conformational wells. It would be interesting to test this hypothesis directly by recording spectra in a gas cell at room temperature.

Glutaronitrile incorporates nitrile groups at either end of a propyl chain, and is therefore prototypical of (α,γ)-disubstituted alkyl chains. We observe only the gg isomer (Figure 6.5). This structure is calculated to be ~300 cm^{-1} more stable than the gt structure that is second in energy, and not observed in our jet-cooled experiment. The dipole moment of the gg structure is purely along the b-axis of the conformation, which can be understood when the three dimensional orientation of the gg structure with respect to the rotational axes is considered. The b-axis goes (only) through carbon atom 3 (Figure 6.5), and carbon atoms 2, 3, and 4 lie in the same plane. The nitrile groups are oriented ~120 ^{o} from one another in relation to the plane containing atoms 2, 3 and 4. Furthermore, the plane where atoms 2, 3, and 4 lie bisects the a and c rotational axes, so that both the a and c axes are each approximately 45 $^{\circ}$ away from the plane, with the a-axis closely associated with the nitrile substituents. Given the symmetry of the gg structure, particularly with respect to plane containing atoms 2, 3, and 4, it becomes apparent that the bond dipoles for the molecule cancel out in the direction of the a and c rotational axes, such that bond dipoles (and consequently a permanent dipole) remains along the b-axis.

6.5. Conclusion

The microwave spectroscopy of 4-pentenenitrile, 4-pentynenitrile, and glutaronitrile has been characterized in this work. The eg+, et, and st conformations of 4-pentenenitrile were observed, and the trans conformation of 4-pentynenitrile was observed. In the case of glutaronitrile, the gg conformation was observed. In all cases, it was not possible to fully resolve and assign nuclear quadrupole splittings. All three molecules may be formed via the combination reactions of resonance-stabilized radicals, and thus they are important candidate species for formation in planetary atmospheres and elsewhere in space. The characterization of these molecules provides the necessary spectroscopic signatures for their search in space, as well as lays the foundation for future photochemistry experiments of these molecules.

6.6. References

1. Müller, H.S.P., et al., A&A, 2001. **370** (3): p. L49-L52.
2. Müller, H.S.P., et al., J. Mol. Struct., 2005. **742** (1–3): p. 215-227.
3. *The Colgne Database for Molecular Spectroscopy*. Available from: http://www.astro.uni-koeln.de/cdms/catalog.
4. Maki, A.G., Journal of Physical and Chemical Reference Data, 1974. **3** (1): p. 221-244.
5. Blackman, G.L., et al., Nature, 1976. **261** (5559): p. 395-396.
6. Hollas, J.M., *Intensities*, in *High Resolution Spectroscopy,* 1998, John Wiley & Sons: Chichester. p. 100-102.
7. Raulin, F., et al., *Titan's Astrobiology*. Titan from Cassini-Huygens, ed. R.H. Brown, J.P. Lebreton, and J.H. Waite2009, Dordrecht: Springer. 215-233.
8. Raulin, F., et al., Chem. Soc. Rev., 2012. **41** (16): p. 5380-5393.
9. Raulin, F., Space Sci. Rev., 2008. **135** (1-4): p. 37-48.
10. Cable, M.L., et al., Chem. Rev., 2012. **112** (3): p. 1882-1909.
11. Yung, Y.L., Icarus, 1987. **72**: p. 468-472.
12. Krasnopolsky, V.A., Icarus, 2009. **201** (1): p. 226-256.
13. Krasnopolsky, V.A., Planetary and Space Science, 2010. **58** (12): p. 1507-1515.
14. Krasnopolsky, V.A., Icarus, 2014. **236** (0): p. 83-91.
15. Banaszkiewicz, M., et al., Icarus, 2000. **147** (2): p. 386-404.
16. Loison, J.C., et al., Icarus, 2015. **247** (0): p. 218-247.
17. Reilly, N.J., et al., J. Am. Chem. Soc., 2008. **130** (10): p. 3137-3142.
18. Reilly, N.J., et al., J. Chem. Phys., 2009. **131** (2).
19. Selby, T.M., et al., J. Phys. Chem. A, 2008. **112** (39): p. 9366-9373.
20. Gautier, T., et al., Icarus, 2011. **213** (2): p. 625-635.

21. Balucani, N., Chem. Soc. Rev., 2012. **41** (16): p. 5473-5483.

22. Molina-Cuberos, G.J., et al., Journal of Geophysical Research-Planets, 2002. **107** (E11).

23. Coll, P., et al., Planetary and Space Science, 1999. **47** (10–11): p. 1331-1340.

24. Brown, G.G., et al., Rev. Sci. Instrum., 2008. **79** (5): p. 053103.

25. Shirar, A.J., et al., J. Phys. Chem. A, 2010. **114** (46): p. 12187-12194.

26. Mohamadi, F., et al., J. Comput. Chem., 1990. **11** (4): p. 440-467.

27. Gaussian 09, R.C., D.01, M. J. Frisch, G. W. Trucks, H. B. Schlegel, G. E. Scuseria, M. A. Robb, J. R. Cheeseman, G. Scalmani, V. Barone, B. Mennucci, G. A. Petersson, H. Nakatsuji, M. Caricato, X. Li, H. P. Hratchian, A. F. Izmaylov, J. Bloino, G. Zheng, J. L. Sonnenberg, M. Hada, M. Ehara, K. Toyota, R. Fukuda, J. Hasegawa, M. Ishida, T. Nakajima, Y. Honda, O. Kitao, H. Nakai, T. Vreven, J. A. Montgomery, Jr., J. E. Peralta, F. Ogliaro, M. Bearpark, J. J. Heyd, E. Brothers, K. N. Kudin, V. N. Staroverov, T. Keith, R. Kobayashi, J. Normand, K. Raghavachari, A. Rendell, J. C. Burant, S. S. Iyengar, J. Tomasi, M. Cossi, N. Rega, J. M. Millam, M. Klene, J. E. Knox, J. B. Cross, V. Bakken, C. Adamo, J. Jaramillo, R. Gomperts, R. E. Stratmann, O. Yazyev, A. J. Austin, R. Cammi, C. Pomelli, J. W. Ochterski, R. L. Martin, K. Morokuma, V. G. Zakrzewski, G. A. Voth, P. Salvador, J. J. Dannenberg, S. Dapprich, A. D. Daniels, O. Farkas, J. B. Foresman, J. V. Ortiz, J. Cioslowski, and D. J. Fox, Gaussian, Inc., Wallingford CT, 2010, 2013.

28. Plusquellic, D.F., et al., J. Chem. Phys., 2001. **115**: p. 3057.

29. Hollas, J.M., *Nuclear Hyperfine Splitting*, in *High Resolution Spectroscopy,* 1998, John Wiley & Sons: Chichester. p. 104-105.

30. Pickett, H.M. *SPFIT/SPCAT*. Available from: http://spec.jpl.nasa.gov.

31. Shirar, A., PhD Thesis, Chemistry Department, Purdue University, 2011.

32. Wilcox, D.S., K.M. Hotopp, and B.C. Dian, J. Phys. Chem. A, 2011. **115** (32): p. 8895-8905.

33. Samdal, S., H. Møllendal, and J.-C. Guillemin, J. Phys. Chem. A, 2013. **117** (40): p. 10304-10310.

34. Samdal, S., et al., J. Phys. Chem. A, 2014. **118** (8): p. 1413-1419.

APPENDIX

APPENDIX

Product Quantum Yield In A Uv Hole-Filling Experiment

The goal of this appendix is to provide some guidance for carrying out product quantum yield calculations in a UV hole-filling experiment. This guide is specifically written with respect to the (E)/(Z)-PVN→quinoline hole-filling experiment, but similar equations can be considered for other photochemical systems. Hereafter, (Z)-PVN, (E)-PVN, and quinoline will be referred to as Z, E, and Q respectively. Photoexcited Z is denoted as Z*.

Upon the photoexcitation of Z, Z* is formed. In the case of the Z→Q photochemistry experiment described in Chapter 5 of this thesis, the S_0-S_1 origin of Z was pumped to initiate photochemistry, imparting 33,707 cm^{-1} of energy to Z, and forming Z*. Z* can take three pathways, as shown below:

$$Z + h\nu \rightarrow Z^*$$

$$Z^* \rightarrow Z$$

$$\rightarrow E$$

$$\rightarrow Q$$

In the first pathway, Z* refills back to ground state Z. In the second pathway, Z* can isomerize to E, and in a third scenario, Z* can lead to Q formation. The kinetic scheme says nothing explicitly about whether the isomerization occurs on the ground or excited state surfaces, but internal conversion to the ground state surface must occur prior to vibrational cooling to the final products. These three pathways from Z* are formulated

barring dissociation on the ground state surface as an alternative competing reaction pathway. Addition of such photodissociation pathways to the kinetic scheme is a straight-forward process and will not be considered further here. However, we have reason to believe that this formulation is valid, since two experimental factors argue against the possibility of dissociation (i) the long excited state lifetimes of E and Z and (ii) facile E↔Z isomerization.

The quantum yield for Q product formation following photoexcitation of reactant Z, is just the ratio of the number of products Q formed per photon absorbed by Z:

$$\Phi_Q = \frac{N_Q}{N_Z^{exc}} \qquad (1)$$

Here N_Z^{exc} equals the number of molecules of Z excited by the UV laser. Unfortunately, we do not know N_Z^{exc}, since all we measure is the net depletion of Z in the hole-filling experiment, which measures Z molecules that did not refill back to the ground state of Z. In lieu of this, we can estimate an upper bound to Q product formed in the photochemistry experiment relative to the number of excited molecules Z* that react in total, N^{react} (from the fractional depletion of Z, I_Z^{dep}):

$$\frac{N_Q^{photochem}}{N^{react}} = \frac{N_Q^{photochem}}{\Delta N_Z} = \frac{N_Q^{photochem}}{\left(\frac{\Delta N_Z}{N_Z}\right)\cdot N_Z} = \frac{N_Q^{photochem}}{\left(I_Z^{dep}\right)\cdot N_Z} \qquad (2)$$

In order use Equation (2), we need to be able to relate signal size I(volts) to the number density of molecules N. Equation (3) demonstrates the relationship between I and N, for the case of Z.

$$I_Z(\text{volts}) = \sigma_Z(\lambda_1)\cdot N_{ph}(\lambda_1)\cdot f_{ion}\cdot N_Z\cdot \ell\cdot V_z \qquad (3)$$

where $\sigma_z(\lambda_1)$ = absorption cross section at the wavelength λ_1. Units of "cm^2/molecule"

N_{ph} = # of photons intersecting sample at λ_1, the wavelength used in the first step of resonant two-photon ionization (R2PI).

f_{ion} = fraction of excited molecules ionized at λ_2, the wavelength used to ionize.

In 1 color R2PI, $\lambda_1 = \lambda_2$, and in 2 color R2PI $\lambda_1 \neq \lambda_2$.

N_Z = # density of molecules in the ion source region (in molecules/cm^3)

ℓ = path length. Units of "cm"

V_Z = signal in voltage (V) at microchannel plate (MCP) gain setting used.

Similarly, we can relate the number density for Q to its observed signal:

$$I_Q(\text{volts}) = \sigma_Q(\lambda_1) \cdot N_{ph}(\lambda_1) \cdot f_{ion} \cdot N_Q \cdot \ell \cdot V_Q \qquad (4)$$

Since no Q formation was detected in the hole-filling photochemistry experiment, $I_Q^{photochem} < 3 \cdot I_Q^{noise}$. With this, an upper bound for Q formation and Φ_Q can be approximated. The following must hold for the signal of Q in the photochemistry experiment:

$$I_Q^{photochem}(\text{volts}) = \sigma_Q(\lambda_1) \cdot N_{ph}(\lambda_1) \cdot f_{ion} \cdot N_Q^{photochem} \cdot \ell \cdot V_Q < 3 \cdot I_Q^{noise}$$

$$N_Q^{photochem} < \frac{3I_Q^{noise}}{\sigma_Q(\lambda_1) N_{ph}(\lambda_1) f_{ion} \ell V_Q} = \frac{3I_Q^{noise}}{f_{Q,det}^{photochem}} \qquad (5)$$

Normally, we could rearrange Equation (3) for Nz, and use equation (5) for N_Q and plug them into Equation (2) along with the fractional depletion of Z in the hole-filling experiment. However, in order to sidestep our lack of knowledge about the $\sigma(\lambda_1)$s, $N_{ph}(\lambda_1)$, f_{ion}'s, etc., we can calibrate the signals due to the Q and Z using original samples based on the R2PI signals starting from known number densities of each molecule behind the nozzle:

$$\frac{I_Q^{sample}}{N_Q^{sample}} = \sigma_Q(\lambda_Q) \cdot N_{ph}(\lambda_Q) \cdot f_{ion}^{Q} \cdot \ell \cdot V_Q = f_{Q,det}^{sample} \qquad (6)$$

$$\frac{I_Z^{sample}}{N_Z^{sample}} = \sigma_Z(\lambda_Z) \cdot N_{ph}(\lambda_Z) \cdot f_{ion}^{Z} \cdot \ell \cdot V_Z = f_{Z,det}^{sample} \qquad (7)$$

In Equations (6) and (7), $f_{Q,det}^{sample}$ and $f_{Z,det}^{sample}$ are the detection sensitivities of each molecule, as a signal voltage/# density. Still, Equations (6) and (7) do not eliminate the dependency on $\sigma(\lambda_1)$s, $N_{ph}(\lambda_1)$, f_{ion}'s, etc., for which we have no information. Therefore, it is useful to relate the number density and corresponding signal sizes back to one species, say Q, thereby eliminating differences in associated with $\sigma(\lambda_1)$s, f_{ion}'s, etc. We can achieve this by knowing the relationship between the number densities of Q and Z behind the nozzle in the authentic samples of each used for calibration.

According to predictions from SciFinder,[1] the vapor pressure of Q is about eight times higher than the vapor pressure of Z at 25 ˚C, such that $N_Q^{sample} = 8 \cdot N_Z^{sample}$. To compensate for the difference in vapor pressures for Q and Z, the Z sample was heated. Q was detected at ~44 ˚C, and Z was detected at ~61 ˚C. In general, a factor of two increase in vapor pressure for every 10 ˚C increase in vapor pressure is a reasonable approximation, such that $N_Q^{sample} = 2 \cdot N_Z^{sample}$ (or equivalently $N_Q^{sample}/N_Z^{sample} = 2$). It follows that:

$$\frac{I_Q^{sample}}{I_Z^{sample}} = \left(\frac{f_{Q,det}^{sample}}{f_{Z,det}^{sample}}\right)\left(\frac{N_Q^{sample}}{N_Z^{sample}}\right) = \left(\frac{f_{Q,det}^{sample}}{f_{Z,det}^{sample}}\right) \cdot 2 \qquad (8)$$

It is useful to keep Equation (8) in mind for subsequent steps. Plugging in rearranged forms of Equations (6) and (7) and I_Z^{dep} into Equation (2) allows us to arrive at an equation for the upper bound of the formation of Q:

$$\frac{N_Q^{photochem}}{N^{react}} < \frac{\left(\frac{3I_Q^{noise}}{f_{Q,det}^{photochem}}\right)}{\left(I_Z^{dep}\right)\cdot\frac{I_Z^{sample}}{f_{Z,det}^{sample}}} = \left(\frac{3I_Q^{noise}}{I_Z^{dep}\cdot I_Z^{sample}}\right)\left(\frac{f_{Z,det}^{sample}}{f_{Q,det}^{photochem}}\right) \qquad (9)$$

In Equation (9), we remember that since no Q was detected, $I_Q^{photochem} < 3 \cdot I_Q^{noise}$, and consequently make the substitution of $3 \cdot I_Q^{noise}$ in place for $I_Q^{photochem}$. We then rearrange Equation (9) to restate it in terms of Q and I_z^{dep} by multiplying and dividing by $f_{Q,det}^{sample}$, and substituting equation (8) into the result:

$$\frac{N_Q^{photochem}}{N^{react}} < \left(\frac{3I_Q^{noise}}{I_Z^{dep} \cdot I_Z^{sample}}\right)\left(\frac{f_{Z,det}^{sample}}{f_{Q,det}^{sample}}\right)\left(\frac{f_{Q,det}^{sample}}{f_{Q,det}^{photochem}}\right)$$

$$\frac{N_Q^{photochem}}{N^{react}} < \left(\frac{3I_Q^{noise}}{I_Z^{dep} \cdot I_Z^{sample}}\right)\left(2 \cdot \frac{I_Z^{sample}}{I_Q^{sample}}\right)\left(\frac{f_{Q,det}^{sample}}{f_{Q,det}^{photochem}}\right)$$

$$= \left(\frac{6I_Q^{noise}}{I_Z^{dep} \cdot I_Q^{sample}}\right)\left(\frac{f_{Q,det}^{sample}}{f_{Q,det}^{photochem}}\right) \quad (10)$$

Equation (10) is the final result, where I_Z^{dep} is the fractional depletion (no units) from the hole-filling experiment, I_Q^{noise} is the noise in the hole-filling experiment, and I_Q^{sample} is the signal in the pure Q sample. $f_{Q,det}^{sample}/f_{Q,det}^{photochem}$ is the ratio of the detection sensitivities for when the pure sample of Q was detected, to the detector sensitivity towards Q in the hole-filling experiment. This ratio would incorporate differences in microchannel plate voltages and laser powers.

New microchannel plates were installed in between the signal measurements of the Q and the UVHF experiment in search of Q. While potential differences in the detection sensitivities prevents us from making an accurate quantitative determination of an upper bound for the quantum yield for quinoline formation, we provide a crude approximation for the Q product quantum yield below.

The values of I_Q^{noise}, I_Z^{dep}, and I_Q^{sample} are 0.0063 V, 0.0423, and 0.2924 V respectively. In order to obtain a value for the $f_{Q,det}^{sample}/f_{Q,det}^{photochem}$ ratio, we need to account for the differences in detection sensitivities associated with the measurement of the pure Q sample, as well as for Q during the photochemistry experiment.

Q sample was measured at a MCP voltage of -2,800 V, with three divide by two neutral density filters and one transmit 75% neutral density filter. Q was searched for in the UVHF photochemistry experiment using a MCP voltage of -2,050 V and three divide by two neutral density filters. In general, for every 100 V gain on the MCP, the signal increases by a factor of two. $f_{Q,det}^{photochem}$ needs to account for the following factors:

- 2^8, to account for the differences in sensitivity for the different MCP voltages used when measuring the Q sample and looking for Q in photochemistry.
- 0.75, to account for the extra neutral density filter in Q sample measurements (to roughly equalize laser powers)

This means $\frac{f_{Q,det}^{sample}}{f_{Q,det}^{photochem}} = \frac{1}{2^8 \cdot 0.75} = \frac{1}{192}$

We can take our known values of I_Q^{noise}, I_Z^{dep}, I_Q^{sample} and the $f_{Q,det}^{sample}/f_{Q,det}^{photochem}$ ratio and place them into Equation (10) in order to estimate an upper bound to the Q product formation in the UVHF photochemistry experiment. In doing this, our upper bound to Q formation in the UVHF photochemistry experiment is approximately 1.6 %.

References:

1. SciFinder, Calculated using Advanced Chemistry Development (ACD/Labs) Software V11.02 (© 1994-2015 ACD/Labs).

VITA

VITA

Deepali Mehta-Hurt was born in Ahmedabad, Gujarat, in India on October 6th, 1987. In 1993, Deepali's family relocated to Southern California, with the help of Deepali's paternal uncle, aunt, and cousin. When Deepali took chemistry classes in high school, her chemistry teacher Ms. Cassandra Whitsett showed her how chemistry can be fun, challenging, and filled with problem-solving. Deepali began her undergraduate studies as a chemistry major at California State University, Fullerton (CSUF) in 2005 after graduating from John F. Kennedy High School in La Palma, CA. While studying at CSUF, Deepali did undergraduate research in the lab of Dr. Zhuangjie Li. Her research involved measuring the pressure and temperature dependence of rate constants for the reaction of the hydroxyl radical with common atmospheric pollutants. Deepali was also able to get involved on a project related to the real-time identification of water contaminants via attenuated total reflectance-Fourier transform infrared spectroscopy. Deepali realized she enjoyed research, and with the encouragement of Dr. Mark Filowitz, Dr. Zhuangjie Li, and her family, Deepali decided to go to graduate school for physical chemistry at Purdue University. After graduating from CSUF in May, 2009, Deepali did a "Zero Year" in the Zwier group. She enjoyed the research and officially joined Dr. Zwier's research group in the Fall of 2009. In the years thereafter, Deepali primarily spent her time doing research, and in 2012 married Matthew Robert Hurt, a fellow graduate student in the department. Deepali completed her PhD in May, 2015.

PUBLICATION

THE JOURNAL OF PHYSICAL CHEMISTRY A

Article

pubs.acs.org/JPCA

Vibronic Spectroscopy of a Nitrile/Isonitrile Isoelectronic Pair: *para*-Diisocyanobenzene and *para*-Isocyanobenzonitrile

Deepali N. Mehta-Hurt, Joseph A. Korn, Anna K. Gutberlet, and Timothy S. Zwier*

Department of Chemistry, Purdue University, West Lafayette, Indiana 47907-2084, United States

Supporting Information

ABSTRACT: The ultraviolet spectroscopy of isoelectronic pair *para*-diisocyanobenzene (*p*DIB) and *para*-isocyanobenzonitrile (*p*IBN) has been studied under gas-phase, jet-cooled conditions. These molecules complete a sequence of mono and disubstituted nitrile/isonitrile benzene derivatives, enabling a comparison of the electronic effects of such substitution. Utilizing laser-induced fluorescence (LIF) and resonant two-photon ionization (R2PI) spectroscopy, the S_0-S_1 electronic origins of *p*DIB and *p*IBN have been identified at 35566 and 35 443 cm^{-1}, respectively. In *p*DIB, the S_0-S_1 origin is very weak, with b_{3g} fundamentals induced by vibronic coupling to the S_2 state dominating the spectrum at 501 cm^{-1} (ν_{19}, isocyano bend) and 650 cm^{-1} (ν_{16}, ring distortion). The spectrum extends over 5000 cm^{-1}, remaining sharp and relatively uncongested over much of this range. Dispersed fluorescence (DFL) spectra confirm the dominating role played by vibronic coupling and identify Franck–Condon active ring modes built off the vibronically-induced bands. In *p*DIB, the S_2 state has been tentatively observed at about 6100 cm^{-1} above the S_0-S_1 origin. In *p*IBN, the S_0-S_1 origin is considerably stronger, but vibronic coupling still plays an important role, involving fundamentals of b_2 symmetry. The bending mode of the nitrile group dominates the vibronically-induced activity. Calculations carried out at the TD-DFT B3LYP/6-31+G(d) level of theory account for the extremely weak S_0-S_1 oscillator strength of *p*DIB and the larger intensity of the S_0-S_1 origins of *p*IBN and *p*DCB (*para*-dicyanobenzene) as nitrile groups are substituted for isonitrile groups. In *p*DIB, a nearly perfect cancellation of transition dipoles occurs due to two one-electron transitions that contribute nearly equally to the S_0-S_1 transition. The spectra of both molecules show no clear evidence of charge-transfer interactions that play such an important role in some cyanobenzene derivatives.

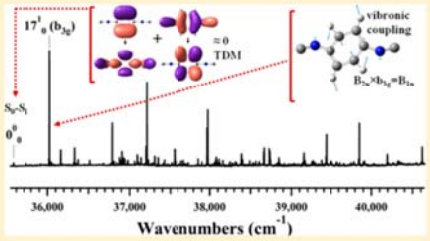

I. INTRODUCTION

Titan, one of the moons of Saturn, has a photochemically driven atmosphere rich in nitrogen and laced with methane (~3%).[1] The lack of oxygen in the atmosphere produces a reducing atmosphere that, under exposure to solar radiation, has produced a suite of organic hydrocarbons, nitriles, and isonitriles.[1,2] Thought to be a model for early Earth's atmosphere, the chemical composition of Titan's atmosphere has been the subject of intense investigation via planetary missions and laboratory-based investigations seeking to determine the nature and altitude-dependent abundance of key constituents.[3] Sophisticated photochemical models are now in place that account for many of the smaller hydrocarbons and nitriles, but much work remains to be done in refining these models and extending them to include larger molecules, where much less is known about the pathways and chemical composition.[4−9]

A role is proposed for aromatic hydrocarbons, polyynes, and nitriles.[10] In this increased molecular size regime, structural isomers are more the norm than the exception. Because these isomers are likely to have unique reactivity, laboratory investigations of photochemistry relevant to Titan's atmosphere are increasingly focused on isomer-specific detection schemes.

Among the most elementary of structural isomers are nitriles (R−C≡N) and isonitriles (R−N≡C) that differ in the relative positions of the N and C atoms in the terminal diatom chain. When R is an alkyl group, the nitriles are lower in energy than their isonitrile counterparts by about 80−100 kJ/mol.[11] At thermal equilibrium, the nitrile isomers should therefore dominate in abundance over their isonitrile counterparts.

However, there are reasons to wonder whether the isonitriles may also play a significant role in the chemical processes taking place in Titan's atmosphere. There is intense interest in establishing whether a "prebiotic" atmosphere such as Titan's could produce molecules relevant to the development of biological processes, including key building blocks such as amides (R−NH−C(=O)−R) that are pervasive in proteins and nitrogen heteroaromatics (purines and pyrimidines) that are relevant to DNA. However, the nitrile group relegates the

Received: January 5, 2015
Revised: February 18, 2015
Published: February 20, 2015

DOI: 10.1021/acs.jpca.5b00099
J. Phys. Chem. A 2015, 119, 2863−2877

nitrogen atom at the terminus of the molecular structure, held firmly in place by an ultrastable C≡N triple bond, with subsequent reactions likely to simply carry along the nitrile substituent unscathed. The isonitrile group represents a first step in the incorporation of the nitrogen atom into the chemical structure, and its destabilization makes it a more likely target for subsequent reactions that further transform the nitrogen atom's chemical properties. The unique properties of the isonitrile group are evident in the two resonance structures for the isonitrile group, which are formally zwitterionic and carbene in character.

$$[R{-}\overset{\oplus}{N}{\equiv}\overset{\ominus}{C}: \leftrightarrow R{-}\ddot{N}{=}C:]$$

The aromatic nitriles/isonitriles are of particular interest because the pathways that produce the first aromatic ring often do not directly produce benzene but rather substituted derivatives such as ethynylbenzene, cyanobenzene, and isocyanobenzene. For instance, the reaction of UV-excited cyanoacetylene (HC_3N) with 1,3-butadiene is known to produce cyanobenzene as one of its prominent products.[12] Because the barrier to isomerization in the electronic ground state is large (~150 kJ/mol)[13] the nitrile or isonitrile isomers are stable relative to rearrangement once formed. This is especially true at the temperatures important in Titan's atmosphere (T < 100 K).

As a result, it is worth exploring in greater depth how the substitution of cyano and isocyano substituents onto an aromatic ring affects the electronic properties and the chemical and photochemical reactivity. In particular, as a precursor to photochemical studies, we present here a detailed study of the vibronic spectroscopy of two prototypical disubstituted cyano/isocyano derivatives, *para*-disocyanobenzene (CN−Ph−NC, *p*DIB, Figure 1b) and *para*-isocyanobenzonitrile (CN−Ph−CN, *p*IBN, Figure 1b), carried out under jet-cooled conditions in the gas phase. We combine the results of R2PI, LIF, and DFL spectroscopy to map out the Franck−Condon active and vibronically-induced transitions in the S_0−S_1 transitions of the two molecules. When joined with dicyano derivative *para*-dicyanobenzene (NC−Ph−CN, *p*DCB, Figure 1b), an interesting triad of isomers is formed, with *p*DCB and *p*DIB having no dipole moment and D_{2h} ground state symmetry, while *p*IBN, with its incorporation of nitrile and isonitrile substituents on the same ring, has a calculated dipole moment of 0.795 D and C_{2v} symmetry.

In what follows, we will compare and contrast the spectroscopic results among this triad, along with their monosubstituted analogs, cyanobenzene (benzonitrile, C_6H_5CN, PhCN) and isocyanobenzene (C_6H_5NC, PhNC) (Figure 1a). Furthermore, ethynyl-substituted aromatics ethynylbenzene (phenylacetylene, $C_6H_5C{\equiv}CH$) and *para*-diethynylbenzene ($HC{\equiv}C{-}C_6H_4{-}C{\equiv}CH$) are isoelectronic with their cyano/isocyano counterparts and are useful additional points of comparison.

Of the monosubstituted nitrile/isonitrile benzene derivatives, several groups[14−16] have studied the perturbative effects of the nitrile group on the electronic spectroscopy of benzene. Cyanobenzene has its S_0−S_1 origin as the most prominent transition in the excitation spectrum, with significant Franck−Condon activity in several of the ring modes typically active in the spectra of benzene derivatives.[15] vibronically-induced transitions are present but rather weak, involving b_2 symmetry fundamentals capable of vibronic coupling to the S_2 state,

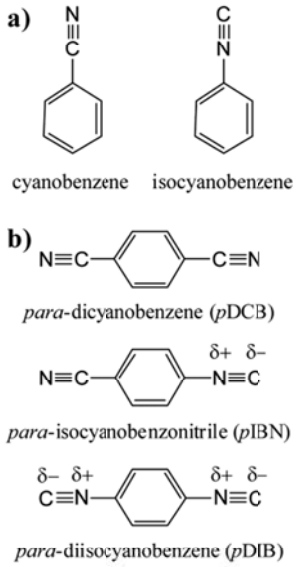

Figure 1. (a) Structural isomers of nitrile/isonitrile monosubstituted benzenes: cyanobenzene and isocyanobenzene. (b) Structures of *p*DIB (D_{2h} point group) and *p*IBN (C_{2v} point group) that were specifically studied in this work, alongside *p*DCB.

whose transition from the ground state carries significant oscillator strength. Furthermore, while early studies based on low-resolution dispersed fluorescence[14] were interpreted as showing the increasing presence of broad, red-shifted emission attributable to charge-transfer emission, later higher-resolution spectra by Sekiya and co-workers[16] showed this broadening to be simply unresolved sharp transitions, leading them to conclude that charge-transfer emission was not present in cyanobenzene.

Much less is known about its isonitrile counterpart, isocyanobenzene, PhNC. No jet-cooled spectrum is available for PhNC. However, there is an absorption cell study by Lombardi and co-workers that explores the spectroscopy of the isoelectronic series ethynylbenzene, cyanobenzene, and isocyanobenzene.[17] From their absorption cell studies, they found that the S_0−S_1 origin transition for isocyanobenzene was much weaker than in cyanobenzene, with vibronically-induced transitions involving an in-plane bend of the isonitrile group dominating the spectrum. Indeed, in this sense, the isonitrile substituent acted more like the ethynyl substituent in ethynylbenzene[18] than the nitrile group in cyanobenzene.

In this work, we present nearly complete assignments of the major transitions in *p*DIB and *p*IBN, identifying the nitrile/isonitrile bends as major sources of vibronic coupling between S_1 and S_2 in both molecules. The various contributors to the dipole-allowed and vibronically-induced components of the spectrum are considered to deduce that changes in the S_0−S_1 oscillator strength are the major source of the differences observed, with vibronic coupling similar in magnitude in both molecules.

DOI: 10.1021/acs.jpca.5b00099
J. Phys. Chem. A 2015, 119, 2863−2877

II. EXPERIMENTAL AND COMPUTATIONAL METHODS

Commercially available *p*DIB (Sigma-Aldrich, 98%) or *p*IBN (Aldrich CPR) was entrained in 3.8 bar backing pressure helium and expanded through a pinhole to generate a supersonic expansion via a Series 9 general valve (500−800 μm, LIF chamber) or a Jordan valve (500 μm, R2PI chamber) to collisionally cool the molecule to its zero-point vibrational energy level in the ground state. To obtain sufficient vapor pressure, the sample was heated to ∼60−80 °C in the general valve and to 45−55 °C in the Jordan valve. After cooling, the molecules were interrogated using laser spectroscopy via both fluorescence- and ionization-based detection schemes.

In LIF, the frequency-doubled output of a Nd:YAG pumped dye laser is used to promote the molecules to the excited state, and the total fluorescence from the molecules is collected and plotted as a function of excitation wavelength, thereby generating an excitation spectrum. The ionization-based counterpart to LIF is R2PI. In R2PI, two photons are used to ionize a molecule of interest, and the total ion signal is collected as a function of excitation wavelength by a microchannel plate at the end of a time-of-flight mass spectrometer. In the case of the disubstituted benzenes studied here, a first resonant photon (supplied from the frequency-doubled output of a Nd:YAG pumped dye laser) and a second photon of higher energy (193 nm from a ArF excimer laser) were used to ionize the molecule due to the high ionization potential of the molecules under study. When the ground state information about the molecule was desired, DFL spectra were collected by fixing the excitation wavelength on a particular transition and dispersing the total fluorescence into individual components across a grating onto a CCD or iCCD camera.

Geometry optimizations and harmonic vibrational frequency calculations were carried out for the ground and first excited singlet states of *p*DIB and *p*IBN using DFT and TD-DFT calculations that employed the B3LYP functional and 6-31+G(d) basis set. The Gaussian 09 suite of programs was used for this purpose.[19] Molecular orbitals were visualized using Chemcraft Software.[20]

III. RESULTS AND ANALYSIS

A. Calculations. Figure 2 summarizes the key structural parameters of the optimized structures calculated for the S_0 and S_1 states of *p*DIB (Figure 2a) and *p*IBN (Figure 2b). The nitrile and isonitrile substituents are calculated to have ground state C≡N/N≡C bond lengths that differ by only 0.016 Å from one another, with the isonitrile being slightly longer. Thus, the two resonance structures that formally contribute to the isonitrile group lead to a bond length nearly identical to that of a nitrile triple bond. The biggest structural difference between nitrile and isonitrile substituents in *p*IBN is the 0.05 Å shortening in the C(Ph)−N bond relative to C(Ph)−C in the ground state. The Merz−Kollman charges[21] associated with the nitrile/isonitrile groups and phenyl carbons to which they are attached are included in the figure and were calculated at the DFT B3LYP/6-31+G(d) level of theory. As the zwitterion resonance structure would indicate, the isonitrile group has a charge distribution of +0.40 on the nitrogen and −0.42 on the carbon, whereas the nitrile group in *p*IBN has a charge distribution of +0.32 on the carbon and −0.43 on the nitrogen. The Merz−Kollman charge analysis strikingly suggests that the nitrogen in the isonitrile group is nearly electrostatically

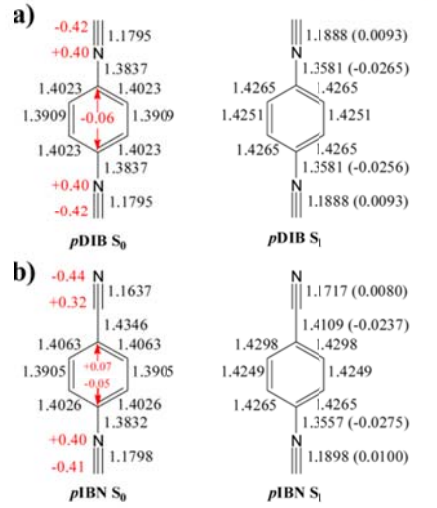

Figure 2. Optimized (DFT B3LYP/6-31+G(d)) ground and S_1 excited state geometries for *p*DIB and *p*IBN. All bond lengths are in angstroms (Å), and the difference between excited and ground state bond lengths is indicated in parentheses for important bonds. Atomic charges are presented in red next to select atoms and were computed using the Merz−Kollman scheme. See the text for further details.

equivalent in charge to the carbon in the nitrile group when substituted on a phenyl ring.

The optimized ground state geometry for *p*DIB has D_{2h} symmetry ($\tilde{X}(^1A_g)$), and its 36 normal modes consist of 7 a_g, 1 b_{1g}, 4 b_{2g}, 6 b_{3g}, 2 a_u, 6 b_{1u}, 6 b_{2u}, and 4 b_{3u} vibrations. Vibrations that involve the isonitrile groups in substantial ways come in g/u pairs with similar frequencies, differing in the phase of oscillation of the atoms in the two substituents. The substitution of one of the isonitrile groups in *p*DIB for a nitrile group forms *p*IBN, lowering the symmetry of the ground state structure to C_{2v}. The a_g/b_{1u} vibrations in D_{2h} reduce to a_1, producing 13 totally symmetric vibrations in *p*IBN. A similar collapse of a_u/b_{1g}, b_{2g}/b_{3u}, and b_{3g}/b_{2u} symmetry species in D_{2h} produces 3 a_2, 8 b_1, and 12 b_2 modes in C_{2v}, respectively. In some cases, the g/u vibrational pairs now become substantially localized on one or the other substituent.

Vertical TD-DFT B3LYP/6-31+G(d) calculations predict a $\pi\pi^*$ first excited state of *p*DIB, $\tilde{A}(^1B_{2u})$, with an allowed *b*-axis-polarized electronic transition from S_0 but very small oscillator strength (f = 0.0012). In *p*IBN, the analogous S_1 state has B_2 symmetry, with an oscillator strength still small (f = 0.0073) but some 6 times larger than in *p*DIB. As anticipated for phenyl derivatives, the optimized excited state geometries of the two molecules are similar to those in the ground state, with an expansion of the ring associated with the $\pi\pi^*$ excitation, slight elongation of both CN and NC bonds (by ∼0.01 Å), and shortening by about 0.03 Å of the C(Ph)−C/N bonds (Figure 2). These predicted structural changes of the C(Ph)−CN and C≡N bonds upon electronic excitation of *p*IBN are in reasonable agreement with a previous study by Kleinermanns and co-workers, which fit the geometry change of cyanoben-

DOI: 10.1021/acs.jpca.5b00099
J. Phys. Chem. A 2015, 119, 2863−2877

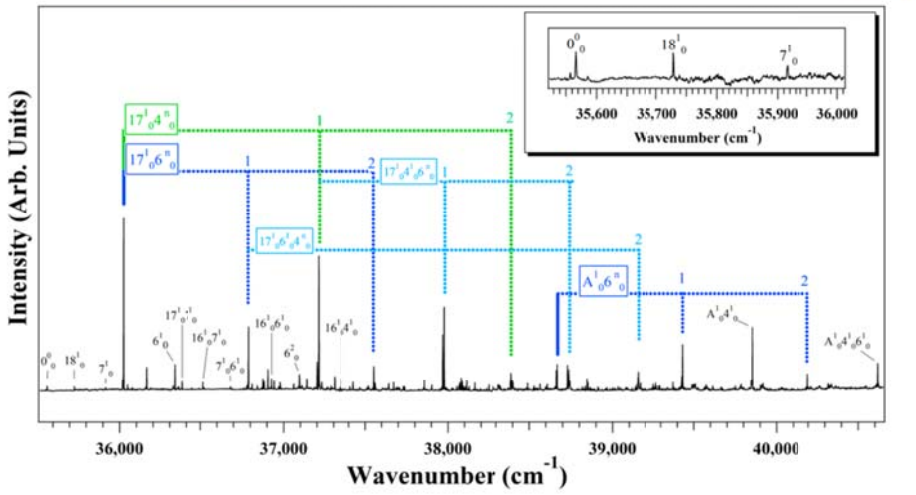

Figure 3. S_0–S_1 excitation spectrum of *para*-diisocyanobenzene. The S_0–S_1 origin is weak, and many transitions that carry intensity can be assigned to vibronically coupled b_{3g} modes (ν_{16-17}) which serve as false origins upon which the Franck–Condon activity of totally symmetric a_g modes ($\nu_{4,6-7}$) is built. Assigned progressions are labeled, with the identity of the vibrational quantum number n presented above each tie line. The inset provides a close-up view of the S_0–S_1 origin region.

zene between S_0 and S_1 to experimentally dispersed fluorescence data.[15]

The vertical TD-DFT B3LYP/6-31+G(d) calculations for *p*DIB/*p*IBN also predict the presence of a nearby second excited state of B_{1u}/A_1 character that has a much larger oscillator strength (f = 0.5329/0.5115). Vertical splitting calculations place the S_2 state some 1196/1313 cm^{-1} above S_1 at the ground state geometry for *p*DIB/*p*IBN. Attempts to optimize the S_2 states of *p*DIB and *p*IBN produced structures with energies below the B_{2u}/B_2 states, counter to experiment (sections B and C). This swap in the energy ordering of S_1 and S_2 states via TD-DFT methods was found previously in the isoelectronic ethynyl-substituted benzene.[22] Because of the vertical TD-DFT prediction of a nearby high oscillator strength second excited state, Herzberg–Teller vibronic coupling of b_{3g}/b_2 modes was carefully considered when assigning the vibronic spectrum.

B. UV Spectroscopy of *para*-Diisocyanobenzene (*p*DIB). The LIF excitation spectrum of *p*DIB has been collected in the region spanning about 35 000 to 42 500 cm^{-1}. We have also recorded a cursory R2PI spectrum over the 35 500–36 550 cm^{-1} region (Supporting Information Figure S1) to verify that the transitions observed in the LIF spectrum are due to the *p*DIB monomer. The LIF excitation spectrum from 35 500 to 40 650 cm^{-1} is shown in Figure 3.

The spectrum is notable relative to other phenyl derivatives in that vibronic activity spans this entire 5000 cm^{-1} range and remains relatively sharp and uncongested over much of this range. Assignments for the vibronic transitions are included in the figure, which are derived from a comparison with its analogs, the predictions of the calculations, and the dispersed fluorescence (DFL) spectra, whose description follows. The labeled tie lines provide a framework for understanding the spectrum. The vibrational numbering follows Mulliken notation,[23] with the form of the normal modes involved in the assigned transitions shown in Figure 4. Table 1 compares the experimental and calculated frequencies for the assigned modes in the S_0 and S_1 states.

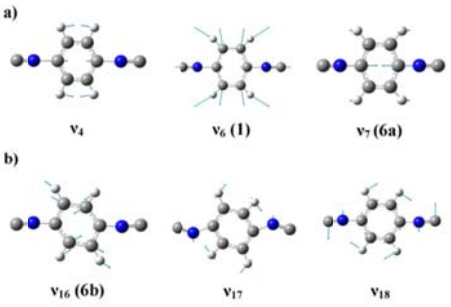

Figure 4. Pictorial representation of ground state normal modes of importance in the UV spectroscopy of *p*DIB. (a) a_g modes involved in Franck–Condon activity and (b) b_{3g} modes involved in Herzberg–Teller coupling of S_1 to S_2. DFT (B3LYP/6-31+G(d)) was used to calculate the harmonic frequencies.

The S_0–S_1 origin is assigned to the very weak transition at 35 566 cm^{-1}, which is seen most clearly in the magnified view shown in the inset of Figure 3. Backing pressure and ultraviolet hole-burning studies (Supporting Information, Figure S1) indicated that this transition and the other two bands +162 and +350 cm^{-1} above it were not hot bands but arose from the

DOI: 10.1021/acs.jpca.5b00099
J. Phys. Chem. A 2015, 119, 2863–2877

Table 1. Assignments for *para*-Diisocyanobenzene Vibrations

para-diisocyanobenzene (*p*DIB)					
		ground state frequencies		excited state frequencies	
mode	symmetry	expt	calc[a]	expt	calc[b]
4 (ν C–X)	a_g	1207	1235	1187	1233
6 (ring breath, 1)	a_g	826	834	766	780
7 (ring def., 6a)	a_g	393	394	350	341
16 (ring def., 6b)	b_{3g}	650	659	596	605
17 (β N≡C)	b_{3g}	501	515	458	418
18 (β C–X)	b_{3g}		183	162[c]	179

[a]Ground state calculations were performed using density functional theory with the B3LYP functional and a 6-31+G(d) basis set. Frequencies are unscaled. [b]Excited state calculations were performed using time-dependent density functional theory using the B3LYP functional and a 6-31+G(d) basis set. Frequencies are unscaled. [c]Assignment is tentative.

same ground state zero-point level as the more intense transitions, despite their extraordinarily weak intensity relative to the dominant transition at 36 024 cm^{-1} (+458 cm^{-1}).

The most intense transition in the spectrum appears +458 cm^{-1} above the origin, assigned to 17^1_0, a b_{3g} fundamental involved in vibronic coupling with the S_2 state. Franck–Condon progressions involving the ν_4, ν_6, and ν_7 ring-deformation and ring-breathing modes build off of this fundamental. Transitions due to other fundamentals with S_1 frequencies of 162 cm^{-1} (tentatively assigned to 18^1_0), 596 cm^{-1} (16^1_0), and 3104 cm^{-1} serve as false origins for other progressions and combination bands involving $\nu_{1,6-7}$. Taken together, these account for the majority of the most intense transitions in the excitation spectrum.

To aid in the assignment of the excitation spectrum, dispersed fluorescence spectra of the origin and many other prominent transitions in the excitation spectrum were collected. When examining the dispersed fluorescence spectra, the presence of Herzberg–Teller vibronic coupling is unequivocally evident in the emission spectrum of the transition at +458 cm^{-1}, as shown in Figure 5. This transition exhibits strong $\Delta v = \pm 1$ emission in a vibration of ground state frequency 501 cm^{-1}, and this emission pattern is characteristic of Herzberg–Teller vibronic coupling. Using the Mulliken notation scheme,[23] we assign the transition at +458 cm^{-1} to 17^1_0, a b_{3g} fundamental involving the in-plane bending of the isocyano substituents. The form of this normal mode is shown in Figure 4b. The prominent 17^1_2 (−1002 cm^{-1}) and $17^1_1 16^0_1$ (−1151 cm^{-1}) transitions in the +458 cm^{-1} dispersed fluorescence spectrum serve as false origins upon which other Franck–Condon vibronic activity involving a_g modes ($\nu_{4,6}$) is built.

After these transitions in the dispersed fluorescence spectrum of the 17^1_0 level are assigned, the assignment of the dispersed fluorescence spectrum of the 35 566 cm^{-1} transition as the S_0–S_1 electronic origin, shown in Figure 6, follows readily. After the subtraction of scattered light, resonance fluorescence is the strongest feature in the S_0–S_1 0^0_0 emission spectrum, indicating that the allowed character of the S_0–S_1 transition contributes to the emission, despite its weak character. In addition, as anticipated, the 17^0_1 and 16^0_1 transitions at −501 and −650 cm^{-1} that appear as a result of vibronic coupling serve as false origins for Franck–Condon activity in $\nu_{4,6}$. The weak transition at −393 cm^{-1} is assigned as 7^0_1, involving the a_g fundamental equivalent to 6a in Varsanyi notation, the substituent-sensitive in-plane ring deformation.[24] The assignment of the ν_7 fundamental is confirmed by the dispersed fluorescence of the +808 cm^{-1} transition (Supporting Information Figure S2) assigned as $17^1_0 7^1_0$, which shows a strong transition at −390 cm^{-1} due to $17^1_0 7^1_1$. The excited state frequency of ν_7 is 350 cm^{-1}. Interestingly, the dispersed fluorescence from the +458 cm^{-1} (17^1_0) transition shows more vibronic activity than the dispersed fluorescence spectrum of the S_0–S_1 origin. Because the strong $\Delta v_{17} = \pm 1$ transitions arise from the vibronic coupling of S_1 ($v_{17} = 1$) with S_2, the larger Franck–Condon

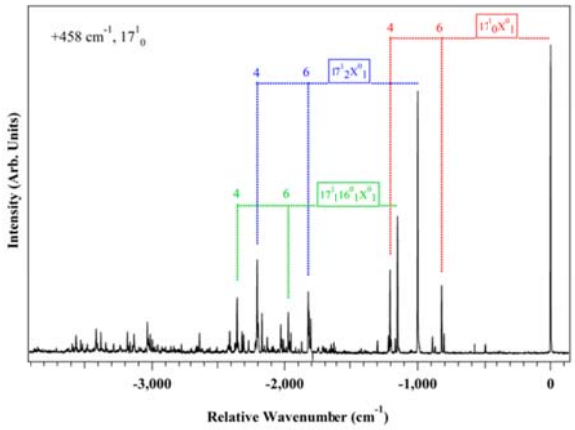

Figure 5. Dispersed fluorescence spectrum of the +458 cm^{-1} transition of *p*DIB, assigned to 17^1_0. The 17^1_0, 17^1_2, and $17^1_1 16^0_1$ transitions serve as false origins upon which Franck–Condon activity is built. X is used to denote a totally symmetric mode; the identity of X is listed above each respective tie line.

DOI: 10.1021/acs.jpca.5b00099
J. Phys. Chem. A 2015, 119, 2863−2877

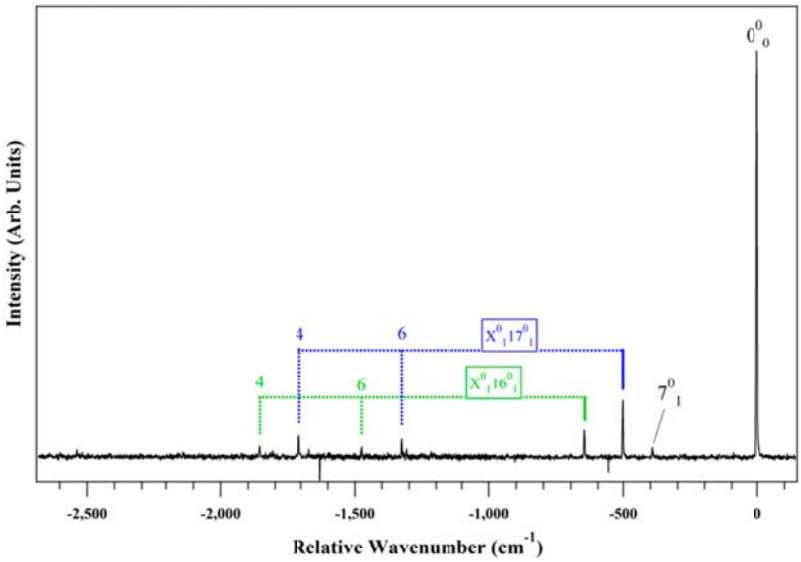

Figure 6. Dispersed fluorescence spectrum of the S_0–S_1 origin transition of *p*DIB. The 16^0_1 and 17^0_1 transitions serve as false origins upon which Franck–Condon activity is built. X is used to denote a totally symmetric mode; the identity of X is listed above each respective tie line.

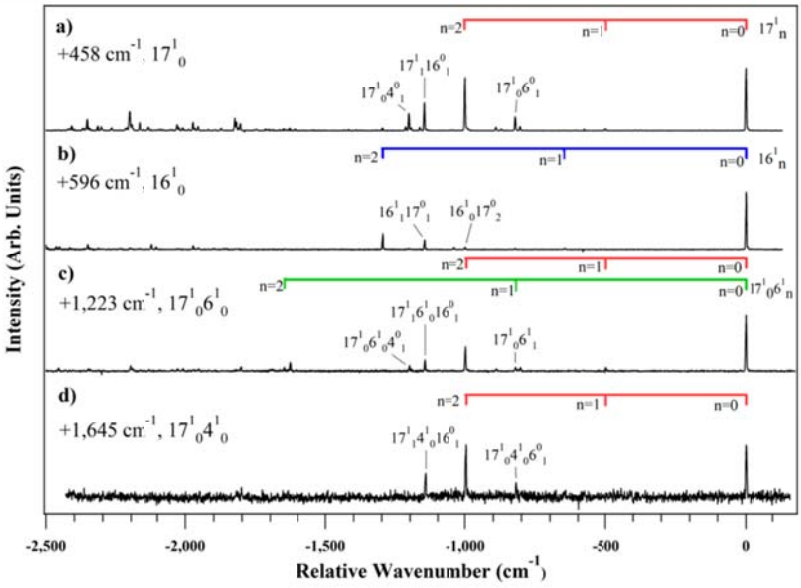

Figure 7. Dispersed fluorescence spectra of the (a) 17^1_0 (b) 16^1_0, (c) $17^1_0 6^1_0$, and (d) $17^1_0 4^1_0$ transitions of *p*DIB. These transitions derive their oscillator strength in excitation from vibronic coupling. See the text for further discussion.

DOI: 10.1021/acs.jpca.5b00099
J. Phys. Chem. A 2015, 119, 2863−2877

activity in combination bands built off of these transitions must reflect a larger geometry change associated with the S_0-S_2 transition than S_0-S_1.

Figure 7 presents dispersed fluorescence spectra from a series of prominent transitions in the excitation spectrum, assigned to Herzberg–Teller-induced transitions. For comparison, the spectrum of 17^1_0 is included (Figure 7a). The transition +596 cm^{-1} above the S_1 origin is assigned as 16^1_0, with a dispersed fluorescence spectrum (Figure 7b) closely analogous to that of the 17^1_0 transition. Vibronic coupling produces a false origin at −1297 cm^{-1}, assigned to 16^1_2. The calculations predict ν_{16}, a second b_{3g} vibration analogous to 6b (Varsanyi notation), to have a frequency of 659/605 cm^{-1} (Table 1) in S_0/S_1. Note that, in addition to the pure $\Delta v = \pm 1$ transitions involving mode 16 (16^1_0 and 16^1_2), the cross-sequence bands producing $16^1_1 17^0_1$ and $16^1_0 17^0_2$ transitions are also present, and they are with a reversed intensity pattern from 17^1_0. This effect, analogous to Duschinsky mixing, was pointed out by Small as a necessary consequence when two or more modes of the same symmetry are involved in vibronic coupling.[25] Further consideration of the consequences of such Duschinsky mixing for vibronic coupling will be taken up in the Discussion section.

The DFL spectra of the +1223 and +1645 cm^{-1} transitions are shown in Figure 7c,d, respectively. Their marked similarity to the DFL of 17^1_0 is apparent. On the basis of this similarity and the strong Franck–Condon activity involving ν_4 and ν_6 in other dispersed fluorescence spectra, the transitions at 1223 and 1645 cm^{-1} are assigned to $17^1_0 6^1_0$ and $17^1_0 4^1_0$, respectively. Progressions in ν_6 (6^1_0 at 765 cm^{-1}, 6^2_0 at 1528 cm^{-1}) and a $7^1_0 6^1_0$ combination band at +1116 cm^{-1} are present in the excitation spectrum, consistent with these assignments. The $17^1_0 6^1_0$ dispersed emission (Figure 7c) is remarkably similar to that of 17^1_0 (Figure 7a) in the first 1200 cm^{-1} of the spectrum, signaling the presence of one quantum in ν_{17}. A modulation in the intensity of the $17^1_0 6^1_n$ progression is also apparent, though the intensities of these transitions are likely affected by interference effects between the S_1 and S_2 components of the vibronically mixed excited state wave function. It is also possible that $17^1_0 6^1_0$ is in Fermi resonance with 15^1_0, another b_{3g} fundamental with a predicted excited state frequency of 1317 cm^{-1}, producing $\Delta v_{15} = \pm 1$ transitions that land in 15_0 or 15_2, the latter of which is beyond the end point of the spectrum. A more detailed investigation of this possibility awaits future work.

Finally, the assignment of the transition at 3104 cm^{-1}, which serves as a false origin for Franck–Condon activity involving $\nu_{4,6}$, remains. We do not have a firm assignment for this transition, and as such, it is denoted as A^1_0 in Figure 3. A candidate assignment for the +3104 cm^{-1} transition is the 13^1_0 b_{3g} fundamental for the following reasons: (i) theory predicts a C–H stretch fundamental near 3233 cm^{-1}, which upon scaling by the typical scale factor at this level of theory[26] (0.9636) results in a predicted transition near 3115 cm^{-1} and (ii) 3104 cm^{-1} has progressions and combination bands involving $\nu_{4,6}$ built off of it much like the 16^1_0 and 17^1_0 b_{3g} fundamentals. However, there is little by way of precedence for vibronic coupling involving CH stretch modes in aromatics nor does the mode have any significant component of CN bend to its motion, which is present in the other vibronically coupled b_{3g} modes (ν_{16-18}).

Given the dominant role played by the vibronic coupling of S_1 with S_2 and the large calculated oscillator strength for the S_0-S_2 transition, a search for the S_0-S_2 origin was carried out. We were guided in this search by the case of ethynylbenzene, where the S_2 state was located 41 955 cm^{-1} S_1.[27] Figure 8a presents the LIF excitation spectrum of *p*DIB in the 41 320–42 550 cm^{-1} region, some 5754–6984 cm^{-1} above the S_1 origin. An intense set of closely spaced transitions was detected, centered on 41 710 cm^{-1}, some 6145 cm^{-1} above the S_1 origin. We tentatively assign this to the S_0-S_2 origin because of its large intensity and isolated frequency well above the last S_0-S_1 transition. The absence of an overlapping transition makes it difficult to accurately determine the intensity increase in Figure 8a with respect to Figure 3, though the intensity of the transitions in Figure 8a is large, in keeping with the tentative association of this region with S_2.

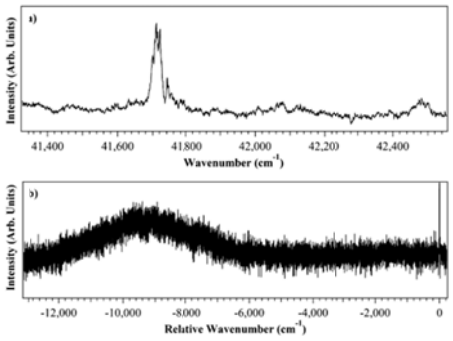

Figure 8. (a) Tentative identification of the S_0-S_2 region in *p*DIB, about 6100 cm^{-1} above the S_0-S_1 origin transition and (b) dispersed fluorescence spectrum of the +6145 cm^{-1} transition. Note that the resonance fluorescence/scattered light is offscale.

The dispersed fluorescence spectrum from 6145 cm^{-1} is shown in Figure 8b. No sharp transitions are observed, but instead a broad, red-shifted emission peak −9500 cm^{-1} above the ground state zero-point level was observed. This red-shifted and broadened emission indicates that if the bands carrying the oscillator strength in absorption are the S_2 origin, then internal conversion to high-lying levels of S_1 must be occurring on a time scale that is fast compared to fluorescence. Given the large shift, which is about 3500 cm^{-1} further than $\Delta v = 0$ Franck–Condon emission, there is a possible role of the charge-transfer state at these high energies that red-shifts the emission.

C. 4-Isocyanobenzonitrile. Figure 9 presents the R2PI spectrum of *p*IBN (C_{2v} point group) acquired over the range 35 100 to 37 800 cm^{-1}, with major transitions labeled with their assignments. Mass-resolved R2PI spectra were recorded in lieu of LIF spectra because of the suspected degradation of *p*IBN over time upon exposure to atmospheric water vapor. Table 2 summarizes the assigned vibrational frequencies of the modes involved in the vibronic activity, which can be compared to their counterparts in *p*DIB from Table 1. As in *p*DIB, assignments are made on the basis of a comparison with other phenyl derivatives, the predictions of calculations, and dispersed fluorescence spectra, which will be discussed shortly.

The R2PI spectrum shows strong vibronic activity over the first 2000 cm^{-1}, but no transitions are observed above 37 500 cm^{-1}, suggesting the onset of a nonradiative pathway that is not present in *p*DIB. Further investigation via ultraviolet depletion

DOI: 10.1021/acs.jpca.5b00099
J. Phys. Chem. A 2015, 119, 2863–2877

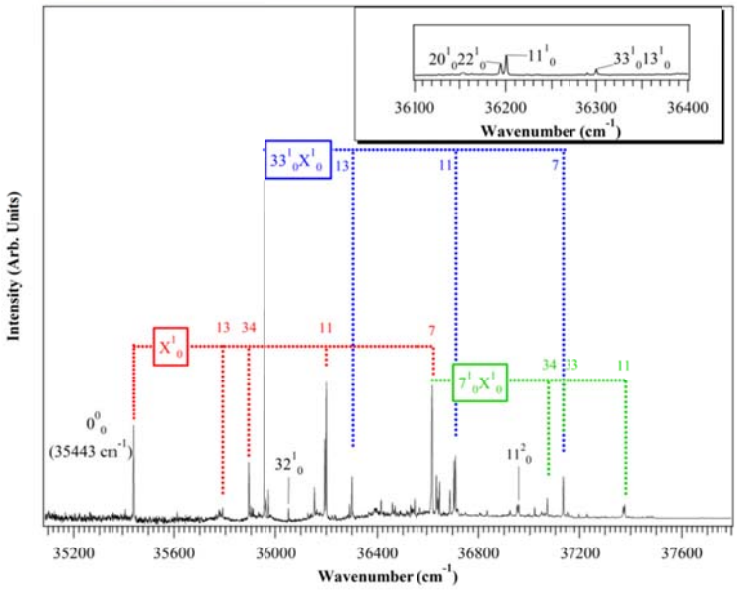

Figure 9. Assigned R2PI spectrum of *p*IBN. Inset: Magnified view in the region where the Fermi-resonant $11^1_0/20^1_022^1_0$ transitions occur. The number labels above the tie lines indicate the mode number X of the totally symmetric vibrations carrying Franck–Condon intensity.

Table 2. Assignments for *para*-Isocyanobenzonitrile (*p*IBN) Vibrations

para-isocyanobenzonitrile (*p*IBN)					
		ground state frequencies		excited state frequencies	
mode	symmetry	expt	calc[a]	expt	calc[b]
7 (C–NC stretch)	a_1	1209	1234	1177	1192
8 (C–CN stretch)	a_1	1173	1201		
11 (ring breathe, 1)	a_1	818	828	752	746
13(ring def., 6a)	a_1	384	386	346	338
24	b_1	81	83		
32 (ring def., 6b)	b_2	653	663	610	619
33 (β C≡N)	b_2	544	557	510	506
34 (β N≡C)	b_2	462	479	448	448
35 (b C–X)	b_2	175	187	170	180

[a]Ground state calculations were performed using density functional theory with the B3LYP functional and a 6-31+G(d) basis set. Frequencies are unscaled. [b]Excited state calculations were performed using time-dependent density functional theory using the B3LYP functional and a 6-31+G(d) bass set. Frequencies are unscaled.

spectroscopy, a double-resonance technique capable of identifying nonradiative transitions, is needed to confirm this hypothesis. The S_0–S_1 origin is assigned to the transition at 35 443 cm^{-1}, with an intensity much stronger relative to vibronic bands than in *p*DIB. The dominant vibronic band is assigned to 33^1_0, a b_2-symmetry fundamental of excited state frequency 510 cm^{-1}, closely analogous to the 17^1_0 transition in *p*DIB. Its strong intensity signals the presence of strong Herzberg–Teller vibronic coupling in *p*IBN, as in *p*DIB.

Herzberg–Teller vibronic coupling manifests itself most strongly in ν_{33} but is also apparent in the appearance of other b_2 symmetry fundamentals, including 34^1_0 (+448 cm^{-1}) and 32^1_0 (+610 cm^{-1}), that should otherwise be symmetry-forbidden. There is also significant Franck–Condon activity in ring modes, much as in *p*DIB, with 13^1_0 (6a), 11^1_0 (1), and 7^1_0 transitions built off the origin and 32^1_0 fundamentals identified by tie lines. The fundamental and combination bands involving 11^1_0 are all closely spaced doublets (Figure 9 inset) due to Fermi resonance between 11^1_0 and $20^1_022^1_0$, where ν_{20} and ν_{22} are two out-of-plane b_1-symmetry fundamentals. Evidence for this assignment is given in what follows.

Figure 10 shows the dispersed fluorescence spectrum following the excitation of the S_0–S_1 origin. The most intense band in emission is due to resonance fluorescence back to the ground state zero-point level, consistent with the increased intensity of the S_0–S_1 origin in excitation. Also prominent in the S_0–S_1 origin emission is the 7^0_1 transition at −1209 cm^{-1}, tentatively assigned to the C–NC stretch. The 7^0_1 fundamental is the most prominent member of a characteristic triad of peaks that is propagated in all of the combination bands built off them (shown in blue in the figure). On the basis of a comparison with *p*DIB (Table 1) and the nature of the modes anticipated to have significant Franck–Condon activity, we tentatively assign the transition at −1173 cm^{-1} to 8^0_1, the C–CN stretch. The dominant intensity of 7^0_1 over 8^0_1 reflects larger Franck–Condon activity in ν_7 compared to that in ν_8, suggesting a larger geometry change along the C–NC bond. This is borne out by the TD-DFT calculations, which show a shortening of the C–NC bond by −0.0275 Å compared to −0.0237 Å for the

DOI: 10.1021/acs.jpca.5b00099
J. Phys. Chem. A 2015, 119, 2863–2877

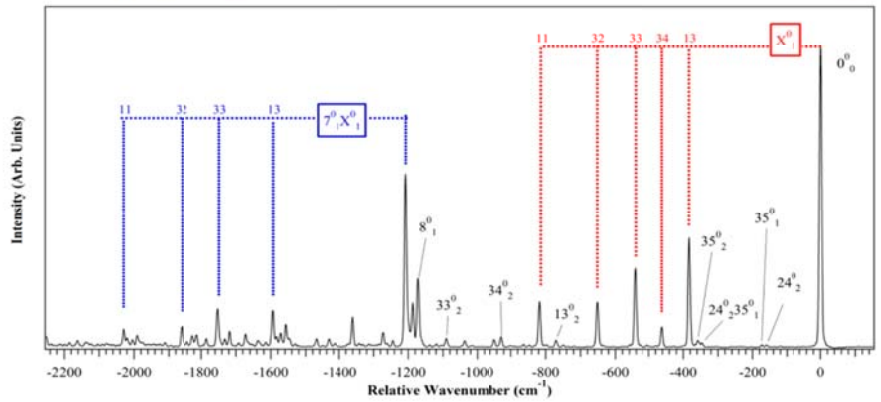

Figure 10. Dispersed fluorescence of the S_0–S_1 origin of *p*IBN.

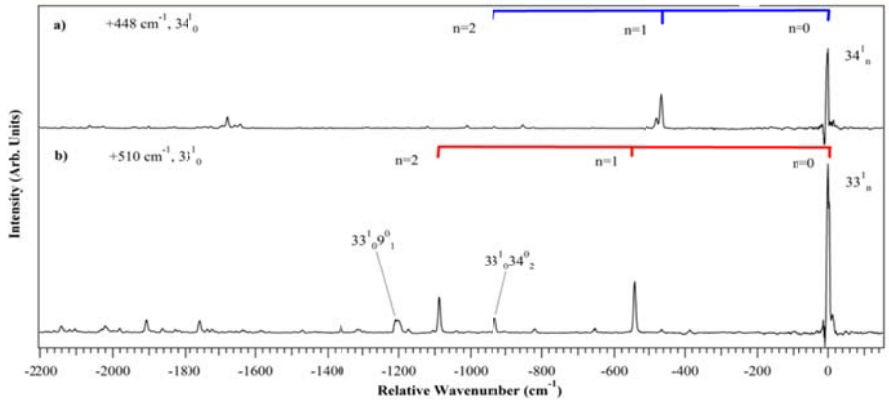

Figure 11. Dispersed fluorescence spectra of the strong b_2 fundamentals of *p*IBN. (a) 34^1_0 and (b) 33^1_0.

C–CN bond (Figure 2). In the origin emission (Figure 10), the 32^0_1, 33^0_1, and 34^0_1 b_2 fundamentals are of moderate intensity, consistent with the larger inherent oscillator strength for the S_0–S_1 transition in *p*IBN. These fundamentals appear to be built off the origin and 7^0_1 transitions.

Figure 11a,b shows the dispersed fluorescence spectra following the excitation of the 33^1_0 and 34^1_0 transitions, respectively. While these spectra at first glance appear to be similar to the expectation for totally symmetric fundamentals, the b_2 symmetry of the upper vibrational level assures us that the $\Delta v = \pm 1$ transitions (e.g., to 33^1_0 and 33^1_2) arise exclusively from Herzberg–Teller vibronic coupling, as they terminate in a_1 vibrational levels. The 33^1_1 transition, on the other hand, is a dipole-allowed transition. The resonance fluorescence peaks (33^1_0 or 34^1_0) are contaminated with scattered light, making their intensity uncertain, but the relative importance of Franck–Condon allowed versus HT induced can be estimated from the X^1_2/X^1_1 intensity ratio. When X = 33, this intensity ratio is near 1, consistent with similar contributions from HT and dipole-allowed portions of the spectrum. The much weaker intensity of the 34^1_0 in excitation (Figure 9) is also reflected in the much smaller 34^1_2 transition in emission relative to 34^1_1. It is also noteworthy that the ν_{33} and ν_{34} vibrations appear to participate in Duschinsky mixing, as manifested in cross-sequence bands such as $33^1_0 34^0_2$ (Figure 11b).

The inset of Figure 9 shows a close-up of the doublet at 36 200 cm^{-1}, assigned to the Franck–Condon-allowed 11^1_0 fundamental and Fermi resonance $20^1_0 22^1_0$ combination band. Figure 12a,b shows that the two dispersed fluorescence spectra are very similar, indicating mixing between them due to Fermi resonance. On the basis of the strong $\Delta v = 0$ propensity present in the origin emission (Figure 10), the two upper levels reflect their mixed character in the relative intensities of the levels in which they terminate in the ground state. On the basis of the ground state frequencies, we assign the two upper levels as 11^1_0 (+758 cm^{-1}) and $20^1_0 22^1_0$ (+752 cm^{-1}), recognizing

DOI: 10.1021/acs.jpca.5b00099
J. Phys. Chem. A 2015, 119, 2863–2877

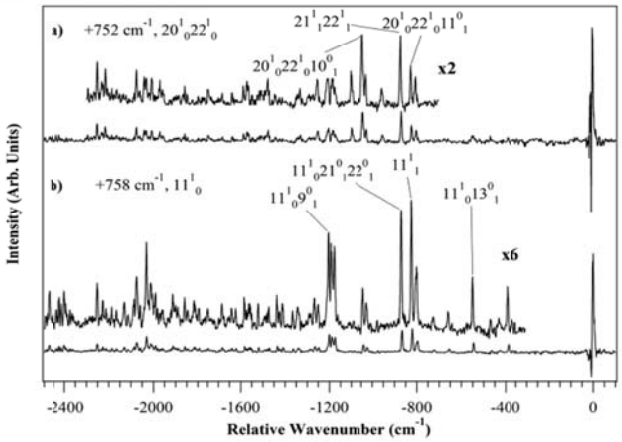

Figure 12. Dispersed fluorescence of Fermi resonance modes (a) $20^1_0 22^1_0$ and (b) 11^1_0 of *p*IBN.

Table 3. List of Experimental S_0-S_1 Origins for the Series, Alongside Calculated Excited State Properties

molecule	exptl S_0-S_1 0^0_0 (cm^{-1})[a]	calc S_0-S_1 0^0_0 (cm^{-1})[b]	ΔE_{12} (cm^{-1})[c]	f_{01}[c]	f_{02}[c]	dM_e/dQ_β[d]	$I(0^0_0)/I(\beta^1_0)$
benzene	38 086[e] (0)	41 444	5397	0.0000	0.0000		
		Monosubstituted Benzene					
ethynylbenzene	35 879[f] (−2207)	37 673	1093	0.0003	0.3249		0.30 (ν_{35} = 492 cm^{-1}) 2.0 (ν_{34} = 561 cm^{-1})
cyanobenzene	36 516[g] (−1570)	38 555	3565	0.0081	0.2258	1.28	4.7 (ν_{32} = 517 cm^{-1}) 45.0 (ν_{31} = ~577 cm^{-1})
isocyanobenzene	36 706[h] (−1380)	38 673	3267	0.0014	0.2466	1.59	~0.43 (ν_{32} = 452 cm^{-1}) ~0.75 (ν_{31} = 547 cm^{-1})
		Disubstituted Benzene (para)					
para-diethynylbenzene[i]	34 255[j] (−3831)	36 292	1466	0.0010	0.6581		0.24 (ν_{20} = 492 cm^{-1})
para-dicyanobenzene	35 120[k] (−2966)	36 427	1516	0.0173	0.4918	3.56	3.4 (ν_{17} = 519 cm^{-1})
para-isocyanobenzonitrile	35 443[l] (−2643)	36 929	1313	0.0073	0.5115	ν_{33} = 4.60 ν_{34} = 2.34	0.25 (ν_{33} = 510 cm^{-1}) 1.6 (ν_{34} = 448 cm^{-1})
para-diisocyanobenzene	35 566[l] (−2520)	37 137	1196	0.0012	0.5339	5.10	0.03 (ν_{17} = 458 cm^{-1})

[a]The shift from the benzene experimental S_0-S_1 origin is indicated in parentheses. [b]This work. Optimization calculations were run using B3LYP/6-31+G(d) (TD-DFT). [c]This work. Vertical calculations were run using B3LYP/6-31+G(d). [d]Approximate induced transition dipole moment when displacing along the bending coordinate β in the ground state. [e]Gruenloh, C. J., et al. *J. Chem. Phys.* **2000**, *113*, 2290−2303. [f]Powers, D. E.; Hopkins, J. B.; Smalley, R. E. *J. Chem. Phys.* **1981**, *74*, 5971−5976. [g]Mordzinski, A.; Sobolewski, A. L.; Levy, D. H. *J. Phys. Chem. A* **1997**, **101**, 8221−8226. [h]Muirhead, A. R., et al. *J. Chem. Phys.* **1972**, *56*, 4385−4393. [i]Vertical and adiabatic calculations (B3LYP/6-31+G(d)) incorrectly predict the energy ordering of S_1 and S_2. The states have been swapped here in accordance with experimental observations. [j]Stearns, J. A.; Zwier, T. S. *J. Phys. Chem. A* **2003**, **107**, 10717−10724. [k]Fujita, K., et al. *J. Phys. Chem.* **1992**, *96*, 10693−10697. [l]This work.

that the out-of-plane vibrations are also involved in extensive Duschinsky mixing. Indeed according to the calculations, modes 20 and 21 change their Mulliken numbering between the excited and ground states; ν_{20} in the ground state is more closely similar to ν_{21} in the excited state from the normal mode analysis.

IV. DISCUSSION

A. Detection in Titan's Atmosphere. Because both aromatics and nitriles are known to be present in Titan's atmosphere, it is natural to postulate the presence of aromatic nitriles as other constituents in the atmosphere. Furthermore, the large barrier to isomerization of isonitriles to nitriles raises the prospect that isonitriles, once formed, would be stable relative to isomerization for long-enough time scales to engage in unique reactions that could lead to the incorporation of the nitrogen atom into structures of prebiotic relevance. Because of their large bond dipoles, both nitriles and isonitriles typically have large permanent dipole moments, making them detectable in the microwave or millimeter wave regions. However, when symmetry exists, as it would in *p*DCB or *p*DIB, microwave detection is not possible. All of the aromatic nitriles included in the series PhCN, PhNC, *p*DCB, *p*IBN, and *p*DIB have ultraviolet spectra with sharp vibronic structures that enable their isomer-specific detection. The present study has completed the series of singly substituted and *para*-substituted

DOI: 10.1021/acs.jpca.5b00099
J. Phys. Chem. A 2015, 119, 2863−2877

nitriles and isonitriles, which have shown unique spectroscopic signatures.

The UV spectra are useful beyond their potential role as spectroscopic signatures in that these same UV absorptions also can serve as the basis for selective photochemical reactions. In particular, one avenue open to the isonitriles is UV-induced isomerization to their nitrile counterparts. *p*DCB is the most stable of the three isomers, with each of the nitrile to isonitrile changes raising the energy by ~80 kJ/mol. Because the UV absorption begins at about 35 000 cm^{-1} (286 nm), the absorption of a UV photon places ~400 kJ/mol into the molecule. If internal conversion to the ground state is facile, then it would produce a vibrationally excited ground state molecule with energy significantly in excess of the calculated barriers for isonitrile to nitrile interconversion (34 kcal/mol = 142 kJ/mol).[13] An energy-level diagram for the photoisomerization is included in the Supporting Information (Figure S3). One would anticipate that each isomerization could occur independently along the separate hindered rotation coordinate for the NC group. It would be interesting to follow this photoisomerization from *p*DIB → *p*IBN → *p*DCB, which is a task left for future work. Here, we simply offer photoisomerization as a method for photoprocessing the isonitrile group to its nitrile counterpart in Titan's atmosphere, anticipating that the lower energy of the nitrile isomer would favor its formation once on the ground state surface.

B. Comparison of Vibronic Spectroscopy of Isoelectronic Series. The present results on the vibronic spectroscopy of *p*DIB and *p*IBN complete a series of studies of mono and para disubstituted nitrile and isonitrile benzene derivatives.[14,17,28,29] We are thus afforded an opportunity to compare and contrast the UV spectroscopy of the members of the series. Table 3 summarizes some of the key results. The table also includes data for isoelectronic ethynyl-substituted analogs ethynylbenzene and *para*-diethynylbenzene.

Using the S_0-S_1 origin of benzene as the "zero" for a relative wavenumber scale, the electronic frequency shifts of the S_0-S_1 electronic origins of cyanobenzene ($\Delta\nu = -1570$ cm^{-1}) and isocyanobenzene ($\Delta\nu = -1380$ cm^{-1}) are similar, with the shift for nitrile substitution about 10% greater than that for isonitrile. The analogous frequency shifts for the disubstituted triad fall into the order one would predict on the basis of the monosubstituted pair, with $\Delta\nu$(*p*DCB) > $\Delta\nu$(*p*IBN) > $\Delta\nu$(*p*DIB), with the magnitude of the shifts just less than twice that of the monosubstituted members. The larger shift for nitrile over isonitrile is in keeping with the notion that the former group, as a more highly polar substituent, perturbs the aromatic π cloud of benzene to a greater extent, and thus the wavelength of the S_0-S_1 $\pi\pi^*$ transition.

Both *p*DIB and *p*IBN have sharp S_0-S_1 vibronic spectra that extend over several thousand wavenumbers, with *p*DIB having transitions with significant intensity out to almost 5000 cm^{-1} above the S_1 origin. This vibronic structure contains transitions arising from Franck–Condon activity that reflect the change in geometry between ground and excited states and involving nontotally symmetric fundamentals that gain intensity from vibronic coupling between the S_1 and S_2 states.

One of the most striking aspects of the comparison among the five members of the nitrile/isonitrile series is the very different relative intensities of the dipole-allowed and Herzberg–Teller-induced portions of the spectrum. Because of the high oscillator strength of the S_0-S_2 transitions in these molecules, even a small amount of vibronic coupling can mix in sufficient S_2 character to induce large transitions in the S_0-S_1 spectrum, as we see.

All five members of the nitrile/isonitrile series have in-plane NC/CN bending mode fundamentals of the right symmetry to vibronically couple S_1 and S_2 states, and in every case, these bending modes are a principal means of doing so, with intensities larger than any other vibronically-induced transitions. The forms of these bending modes for *p*DIB and *p*IBN are compared in Figure 13. Note that the disubstituted

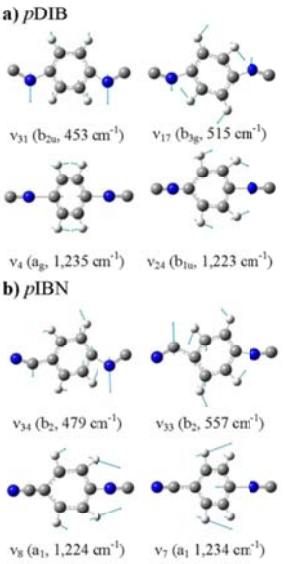

Figure 13. Form of the bending and C–X stretch modes of the nitrile/isonitrile groups in (a) *p*DIB and (b) *p*IBN.

molecules have a set of four in-plane bending fundamentals that come in two in-phase/out-of-phase pairs. In *p*DIB (Figure 13a), the higher-frequency pair involves bending the C(Ph)-N≡C angle ($\nu_{31}(b_{2u})$ = 453 cm^{-1}; $\nu_{17}(b_{3g})$ = 515 cm^{-1}), while the lower-frequency pair (not shown) involves bending the entire isonitrile group ($\nu_{32}(b_{2u})$ = 131 cm^{-1}, $\nu_{18}(b_{3g})$ = 183 cm^{-1}). In *p*IBN (Figure 13b), the four in-plane bending fundamentals are very similar in frequency to those in *p*DIB; however, the replacement of one isonitrile group by nitrile leads to a partial localization of the bending fundamentals on the nitrile or isonitrile substituents.

Table 3 compares the intensity of the S_0-S_1 origin transition to that of the b_2/b_{3g} in-plane bending fundamental of the substituent(s), $I(0^0_0)/I(\beta^1_0)$. Here we have chosen the generic label "β" to signify the bending mode, with the mode number relevant to the particular molecule included in the table.

The singly substituted and disubstituted nitrile derivatives cyanobenzene[14] and *p*DCB[28] both have strong S_0-S_1 electronic origins and vibronic structure dominated by Franck–Condon activity built on the electronic origin. This is what is observed for most aromatic derivatives with allowed S_0-S_1 transitions.[30] Franck–Condon activity involves several totally symmetric in-

DOI: 10.1021/acs.jpca.5b00099
J. Phys. Chem. A 2015, 119, 2863–2877

plane ring modes (1, 6a, 12, and 18 in Varsanyi notation) involving short progressions that reflect a modest geometry change associated with the $S_0(A_1) \rightarrow S_1(B_2)$ $\pi\pi^*$ transition. First-order vibronic coupling to the S_2 state occurs via nontotally symmetric fundamentals (b_2 in PhCN and b_{3g} in *p*DCB) and is comparatively weak. In particular, $I(0^0_0)/I(\beta^1_0)$ = 4.7 and ~45 for PhCN and 3.4 for *p*DCB (Table 3).

By contrast, in *p*DIB, with its pair of para-substituted isonitrile groups, the S_0-S_1 electronic origin is very weak to the point of being barely discernible in the spectrum (Figure 3), with vibronic coupling accounting for the most intense transitions in the spectrum. In the Results and Analysis section, the most intense transition in the spectrum of *p*DIB, located 458 cm^{-1} above the origin, was assigned to b_{3g} in-plane NC-bending fundamental 17^1_0 (Figure 5). As a result, the origin/β^1_0 intensity ratio is more than a factor of 110 times smaller (~0.03) than in PhCN and *p*DCB.

The final two molecules, PhNC and *p*IBN, which contain one isonitrile group, take the middle ground, with intensity ratios $I(0^0_0)/I(\beta^1_0)$ of about 0.3 to 1.6 (Table 3). In the case of PhNC, studied by Muirhead et al., this ratio is estimated from the room-temperature absorption spectrum shown in one of their figures.[17] Furthermore, diethynyl analog *p*DEB also has a similar intensity ratio (Table 3) and so also appears to belong to this same subgroup.[22]

That this intensity ratio changes by more than a factor of 100 in the disubstituted nitrile/isonitrile series is rather remarkable, given how similar the molecules in the series are in so many other ways. Within Herzberg–Teller theory,[31] the contribution to the transition moment due to vibronic coupling for a vibronic transition β^1_0 between S_0 and S_1 states due to vibronic coupling with S_2 is given by

$$M_{01}^{\mathrm{H}^-} = M_{02} \cdot \left\langle \psi_2 \left| \frac{\partial H_{\mathrm{el}}}{\partial Q_\beta} \right| \psi_1 \right\rangle \cdot \frac{\langle \chi^0_{v=0} | Q_\beta | \chi^1_{v=1} \rangle}{\Delta E_{12}} \tag{1}$$

where M_{01} and M_{02} are electronic transition moments for the S_0-S_1 and S_0-S_2 transitions, respectively, ψ_1 and ψ_2 are the S_1 and S_2 excited state electronic wave functions, χ^0 and χ^1 are the vibrational wave functions in S_0 and S_1, and ΔE_{12} is the energy separation between the S_1 and S_2 states involved in vibronic coupling. If we define

$$\gamma_{12} = \left\langle \psi_2 \left| \frac{\partial H_{\mathrm{el}}}{\partial Q_\beta} \right| \psi_1 \right\rangle \tag{2}$$

then intensity ratio $I(0^0_0)/I(\beta^1_0)$ is proportional to

$$\frac{I(0^0_0)}{I(\beta^1_0)} \propto \left[\frac{f_{01}}{f_{02}} \left(\frac{\Delta E_{12}}{\gamma_{12}} \right)^2 \right] \tag{3}$$

where we have subsumed the integral over χ into the constant of proportionality, recognizing that it accounts for the $\Delta v = \pm 1$ selection rules if the form of β is not changed significantly between the S_0 and S_1 states. In eq 3, f_{01} and f_{02} are the oscillator strengths of the S_0-S_1 and S_0-S_2 transitions, respectively.

Equation 3 shows explicitly the terms that contribute to changes in the origin/β^1_0 intensity ratio, which are taken as representative of the ratio of dipole-allowed to vibronically-induced contributions to the spectrum. This intensity ratio can vary due to (i) changes in the inherent oscillator strengths for the S_0-S_1 or S_0-S_2 transitions and (ii) the size of the Herzberg–Teller coupling matrix element between S_1 and S_2 (related to γ_{12}) and/or the energy separation ΔE_{12} between S_1 and S_2.

Table 3 includes calculated values for the factors contributing to the origin/β^1_0 intensity ratio from eq 3, for all members of the series. The vertical splittings ΔE_{12} are similar within the *p*DCB/*p*IBN/*p*DIB series, as are the S_0-S_2 oscillator strengths. The column marked $((\partial M_e)/(\partial Q_\beta))$ lists calculated estimates of the relative transition moment derivatives along each of the indicated bending fundamentals. These were calculated by mapping out the transition moment vector $M_e(Q)$ for small displacements from equilibrium along each bending mode and taking the slope at $Q = 0$. As anticipated, the induced transition moment upon displacement along the bending coordinate is primarily along the *a* axis, indicating the mixing of S_1 (*b*-axis polarized) with S_2 (*a*-axis polarized). However, these calculated transition moment derivatives in the disubstituted series differ by no more than a factor of 2 and therefore cannot account for the greater than 100-fold increase in the $I(0^0_0)/I(\beta^1_0)$ intensity ratio.

What does change dramatically along the *p*DIB → *p*IBN → *p*DCB is the S_0-S_1 oscillator strength f_{01}. The variations in f_{01} identify the small intensity ratio in *p*DIB with the very small S_0-S_1 oscillator strength, correctly predicting *p*IBN as intermediate and *p*DCB as largest, as observed experimentally. Thus, the dominant reason for the observed changes in the ratio of dipole-allowed to vibronically-induced components to the spectra is the changes in the oscillator strength in the S_0-S_1 transition.

In seeking an explanation for the dramatic changes in the inherent oscillator strengths of the S_0-S_1 transitions, TD-DFT calculations were carried out on the S_0-S_1 transitions of interest that identified the single-electron transitions responsible for them. As Table 4 shows, in all of the S_0-S_1 transitions

Table 4. Coefficients for Single-Electron Excitations in Series of Molecules

molecule	single electron excitations and coefficients in S_0-S_1[a]	
ethynylbenzene	26 → 28	0.478
	27 → 29	0.518
cyanobenzene	26 → 28	0.578
	27 → 29	−0.404
isocyanobenzene	26 → 28	0.539
	27 → 29	−0.455
para-diethynylbenzene	32 → 34	0.482
	33 → 35	0.515
para-dicyanobenzene	32 → 34	0.608
	33 → 35	−0.358
para-isocyanobenzonitrile	32 → 34	0.570
	33 → 35	−0.417
para-diisocyanobenzene	32 → 34	0.519
	33 → 35	−0.479

[a] S_1 optimization calculations were run using B3LYP/6-31+G(d) (TD-DFT).

DOI: 10.1021/acs.jpca.5b00099
J. Phys. Chem. A 2015, 119, 2863−2877

of interest, two single-electron transitions contribute. The molecular orbitals responsible for these transitions are shown in Figure 14 for *p*DIB, and the analogous orbitals for the whole set

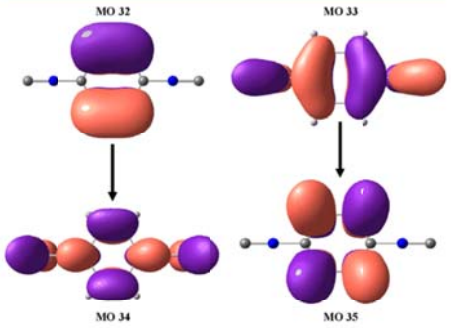

Figure 14. Pictorial representations of molecular orbitals (MOs) comprising S_0−S_1 of *p*DIB. The MOs of the remaining molecules in the series (Table 4) are presented in Supporting Information. Calculations were carried out at the DFT B3LYP/6-31+G(d) level of theory.

of molecules are included in the Supporting Information (Figures S4 and S5). As is apparent from Figure 14, the single-electron transition between molecular orbitals 32 and 34 moves electron density from off-axis carbons onto the two isonitrile substituents, with the transition dipole moment along the *b* axis. For the 33 → 35 transiton, the electron density moves in the opposite direction from the substituents to the off-axis carbons. Because the S_0−S_1 transition is a nearly equal mixture of 32 → 34 and 33 → 35 (with coefficients +0.519/−0.479), the resulting overall TDM cancels nearly perfectly, resulting in a calculated oscillator strength very near zero (f_{01}(*p*DIB) = 0.0012), despite the fact that it is a dipole-allowed transition by symmetry. This is similar to the makeup calculated for *p*DEB (0.482/0.515), which also has an oscillator strength very near zero (f_{01} = 0.0010). In the other two members of the disubstituted aromatics, the MOs are very similar in shape (Supporting Information, Figures S4 and S5), but the contributions from the two one-electron transitions are no longer nearly equal, changing from +0.570/−0.417 in *p*IBN to +0.608/−0.358 in *p*DCB. The calculated oscillator strengths get increasingly large as this difference in the coefficients increases.

While differences in the S_0−S_1 oscillator strength account for the qualitative change in the ratio of dipole-allowed to vibronically-induced portions of the spectrum, changes to f_{01} alone do not account quantitatively for the changes to the $I(0^0_0)/I(\beta^1_0)$ intensity ratios over the entire series. For instance, the calculated f_{01} oscillator strength for *p*DCB is a factor of 14 larger than that for *p*DIB, while the experimental intensity ratio $I(0^0_0)/I(\beta^1_0)$ jumps by more than a factor of 100. Similarly, the oscillator strength for f_{01} in PhCN is about a factor of 5 larger than in PhNC, but the experimental intensity ratio is about a factor of 11 or larger. Some of this discrepancy could arise from the sensitivity of the calculated oscillator strength in *p*DIB to the precise values of the mixing coefficients because they nearly cancel one another.

C. Multimode Vibronic Coupling and Duschinsky Mixing. Up to this point, the focus has been on the bending fundamentals that dominate vibronic coupling between S_1 and S_2. As discussed in section C, in the case of *p*IBN there are two bending fundamentals of the right symmetry for vibronic coupling to S_2, ν_{33}, and ν_{34}, which are primarily nitrile and isonitrile bends, respectively, as shown in Figure 11. As a result, the vibronic spectroscopy of *p*IBN presents an opportunity to test the different effects of nitrile versus isonitrile substitution on the vibronic coupling. In the R2PI spectrum of Figure 9, the intensity of the 33^1_0 fundamental is more than 5 times that of 34^1_0. The same is true in the emission spectrum from the S_1 0^0 level: the 33^0_1 fundamental is several times more intense than its 34^0_1 counterpart. Applying eq 3 to this comparison, because the oscillator strengths (f_{01}, f_{02}) and energy splitting ΔE_{12} are identical in this case, one can surmise that the intensity ratio between the two bending fundamentals, $I(33^1_0)/I(34^1_0)$, is related to changes in the strength of the vibronic coupling matrix element, as embodied in $\gamma_{12}(\nu_{33}) > \gamma_{12}(\nu_{34})$. Indeed, this is exactly what is predicted by the calculations of the transition moment integrals (Table 3). We see that $((\partial M_e)/(\partial Q_{\beta CN}))$ is about twice the size of $((\partial M_e)/(\partial Q_{\beta NC}))$, which would lead to $I(33^1_0)/I(34^1_0) \approx 4$, as observed. Thus, in *p*IBN, the nitrile bend couples to S_2 more efficiently than the isonitrile bend.

These arguments, however, ignore the interference effects that can arise when multiple nontotally symmetric vibrations are involved in vibronic coupling. As Small has pointed out in his classic paper,[25] the presence of multiple nontotally symmetric modes vibronically coupled to the nearby S_2 state will necessarily result in Duschinsky mixing between the modes. This Duschinsky mixing is evident in ν_{16-17} in *p*DIB in the presence of cross-sequence bands in the DFL spectra from the $16^1_0/17^1_0$ levels of *p*DIB (Figure 7a,b). In addition to "pure" Δv = +1 transitions 16^1_2 (Figure 7b) and 17^1_2 (Figure 7a), transitions to the $16_1 17_1$ level are also clearly evident in both spectra.

Furthermore, Small also developed arguments that in the presence of multimode vibronic coupling a lack of mirror symmetry should exist between the intensities of the vibronically-induced fundamentals in the excitation spectrum and origin DFL spectrum because of interference effects.[25] These asymmetries are present in the spectra of both *p*DIB and *p*IBN, sometimes in dramatic fashion. For example, modes 16 and 17 in *p*DIB have b_{3g} symmetry and are engaged in vibronic coupling, with mode 16 being a 6b-like in-plane ring distortion and mode 17 being isonitrile bend β. In excitation (Figure 3), their intensity ratio is $[(I(17^1_0))/(I(16^1_0)) = 6.4$, while in emission from the S_1 origin (Figure 6), $((I(17_1{}^0))/(I(16^0_1)) = 2.0$. The same two modes in *p*IBN (modes 32 and 33 in this case) have $((I(33^1_0))/(I(32^1_0)) > 10$ but $((I(33^0_1))/(I(32^0_1)) > 1.5$. Small[25] and Hollas and co-workers[32] have developed expressions for multimode vibronic coupling that show explicitly how these intensity asymmetries might arise. Their formulation shows that when $\nu_a < \nu_b$, $((I(a^1_0))/(I(b^1_0)) > ((I(a^0_1))/(I(b^0_1))$ when vibronically-induced transition moment vectors m_a and m_b are antiparallel and that the inequality of intensity ratios is reversed when m_a and m_b are parallel. Thus, the large asymmetry in the intensity ratios for these modes arises from their induced moments being antiparallel and similar in size so that interference effects are large.

It is worth noting that the same intensity ratios for ν_{33} and ν_{34} in *p*IBN are not very different, with 33^1_0 dominating 34^1_0 and 33^0_1 dominating 34^0_1 by a similar amount. This is further

DOI: 10.1021/acs.jpca.5b00099
J. Phys. Chem. A 2015, 119, 2863−2877

evidence that the transition moment change induced by the nitrile bend (mode 33) is much larger than that for the isonitrile bend (mode 34) so that the sum (large + small) and difference (large − small) do not modulate the intensity ratio very much.

V. CONCLUSIONS

Vibronic excitation spectra of two isomers, *para*-diisocyanobenzene (*p*DIB) and *para*-isocyanobenzonitrile (*p*IBN), have been recorded under jet-cooled conditions over the 35 000–42 500 and 35 100–37 800 cm^{-1} regions, respectively. These isomers are calculated to be 80 and 159 kJ/mol less stable than the *para*-dicyanobenzene isomer studied previously by Kaya and co-workers and Levy and co-workers.[28,29] UV excitation of both isomers produces sharp spectra that reach several thousand wavenumbers above the electronic origins. The major vibronic features in both spectra were identified and assigned with the aid of dispersed fluorescence spectra, previous studies of analogous molecules, and the predictions of DFT calculations. Both spectra display evidence of strong vibronic coupling of the S_1 state with S_2, mediated through bending mode fundamentals involving the nitrile/isonitrile groups. Dispersed fluorescence spectra were recorded to aid in the assignments. In *p*DIB, the S_1 origin is extremely weak due to the nearly equal but opposing contributions from two one-electron transitions, leading to a nearly perfect cancellation of the S_0–S_1 transition dipole moment, despite its symmetry-allowed character ($\tilde{X}(A_{1g}) \rightarrow \tilde{A}(B_{2u})$). The b_{3g} β_{NC} bending fundamental is responsible for much of the vibronic coupling to S_2, dominating the spectrum. The substitution of a nitrile group for one of the isonitriles to form *p*IBN reduces the symmetry to C_{2v} and turns on intensity in the S_1 origin. The asymmetric substitution partially localizes the nitrile and isonitrile bending modes, with the nitrile bend dominating the vibronic coupling to S_2. Photoisomerization is postulated as a mechanism for the conversion of *p*DIB and *p*IBN to *p*DCB, suggesting that if these isomers are formed in Titan's atmosphere then they may interconvert by solar irradiation to the more stable nitrile counterparts.

■ ASSOCIATED CONTENT

Supporting Information

UV hole-burning spectrum and backing-pressure studies of the 0^0_0 region of *p*DIB. DFL spectrum of the +808 cm^{-1} transition in *p*DIB. Energy-level diagram for the *p*DIB → *p*IBN → *p*DCB isomerization surface. MOs of two single-electron transitions in the monosubstituted species examined in the work. MOs for the para-disubstituted species studied. This material is available free of charge via the Internet at http://pubs.acs.org

■ AUTHOR INFORMATION

Corresponding Author

*E-mail: zwier@purdue.edu.

Present Address

(A.K.G.) Open Grid Europe GmbH, Gladbecker, Str. 404, 45326 Essen, Germany.

Notes

The authors declare no competing financial interest.

■ ACKNOWLEDGMENTS

We gratefully acknowledge support for this research from the NASA Planetary Atmospheres program (13-PATM13-0029). D.N.M.-H. gratefully acknowledges support from the NASA Earth and Space Science Fellowship, and A.K.G. gratefully acknowledges support from Deutscher Akademischer Austausch Dienst.

■ REFERENCES

(1) Raulin, F.; Brasse, C.; Poch, O.; Coll, P. Prebiotic-Like Chemistry on Titan. *Chem. Soc. Rev.* **2012**, *41*, 5380–5393.

(2) Moreno, R.; Lellouch, E.; Lara, L. M.; Courtin, R.; Bockelée-Morvan, D.; Hartogh, P.; Rengel, M.; Biver, N.; Banaszkiewicz, M.; González, A. First Detection of Hydrogen Isocyanide (HNC) in Titan's Atmosphere. *Astron. Astrophys.* **2011**, *536*, L12.

(3) Waite, J. H.; Young, D. T.; Cravens, T. E.; Coates, A. J.; Crary, F. J.; Magee, B.; Westlake, J. The Process of Tholin Formation in Titan's Upper Atmosphere. *Science* **2007**, *316*, 870–875.

(4) Wilson, E. H.; Atreya, S. K., Current State of Modeling the Photochemistry of Titan's Mutually Dependent Atmosphere and Ionosphere. *J. Geophys. Res.:Planet* **2004**, *109*.

(5) Yung, Y. L. An Update of Nitrile Photochemistry on Titan. *Icarus* **1987**, *72*, 468–472.

(6) Krasnopolsky, V. A. A Photochemical Model of Titan's Atmosphere and Ionosphere. *Icarus* **2009**, *201*, 226–256.

(7) Krasnopolsky, V. A. The Photochemical Model of Titan's Atmosphere and Ionosphere: A Version without Hydrodynamic Escape. *Planet. Space Sci.* **2010**, *58*, 1507–1515.

(8) Krasnopolsky, V. A. Titan's Photochemical Model: Further Update, Oxygen Species, and Comparison with Triton and Pluto. *Planet. Space Sci.* **2012**, *73*, 318–326.

(9) Banaszkiewicz, M.; Lara, L. M.; Rodrigo, R.; López-Moreno, J. J.; Molina-Cuberos, G. J. A Coupled Model of Titan's Atmosphere and Ionosphere. *Icarus* **2000**, *147*, 386–404.

(10) Cable, M. L.; Hoerst, S. M.; Hodyss, R.; Beauchamp, P. M.; Smith, M. A.; Willis, P. A. Titan Tholins: Simulating Titan Organic Chemistry in the Cassini-Huygens Era. *Chem. Rev.* **2012**, *112*, 1882–1909.

(11) Koizumi, H.; Baer, T. The Heats of Formation of Tert-Butyl Isocyanide and Other Alkyl Isocyanides by Photoelectron Photoion Coincidence Spectroscopy. *J. Phys. Chem. A* **2004**, *108*, 5956–5961.

(12) General Discussion. *Faraday Discuss.* **2010**, *147*, 83–102.

(13) Mironov, M. A. General Aspects of Isocyanide Reactivity. In *Isocyanide Chemistry*; Wiley-VCH Verlag GmbH & Co. KGaA, 2012; pp 35–73.

(14) Mordzinski, A.; Sobolewski, A. L.; Levy, D. H. Dual Fluorescence in Aromatic Nitriles: The Role of the Charge-Transfer State. *J. Phys. Chem. A* **1997**, *101*, 8221–8226.

(15) Imhof, P.; Krügler, D.; Brause, R.; Kleinermanns, K. Geometry Change of Simple Aromatics Upon Electronic Excitation Obtained from Franck-Condon Fits of Dispersed Fluorescence Spectra. *J. Chem. Phys.* **2004**, *121*, 2598–2610.

(16) Sakota, K.; Nishi, K.; Ohashi, K.; Sekiya, H. Absence of Dual Fluorescence in Jet-Cooled Benzonitrile and p-Tolunitrile. *Chem. Phys. Lett.* **2000**, *322*, 407–411.

(17) Muirhead, A. R.; Allen Hartford, J.; Huang, K.-T.; Lombardi, J. R. Optical Spectra of an Isoelectronic Series; the $\pi^* \leftarrow \pi$ Transition in Phenyl Isocyanide, Ethynylbenzene, and Benzonitrile. *J. Chem. Phys.* **1972**, *56*, 4385–4393.

(18) Powers, D. E.; Hopkins, J. B.; Smalley, R. E. Vibrational Relaxation in Jet-Cooled Phenylalkynes. *J. Chem. Phys.* **1981**, *74*, 5971–5976.

(19) Frisch, M. J.; Trucks, G. W.; Schlegel, H. B.; Scuseria, G. E.; Robb, M. A.; Cheeseman, J. R.; Scalmani, G.; Barone, V.; Mennucci, B.; Petersson, G. A.; Nakatsuji, H.; Caricato, M.; Li, X.; Hratchian, H. P.; Izmaylov, A. F.; Bloino, J.; Zheng, G.; Sonnenberg, J. L.; Hada, M.; Ehara, M.; Toyota, K.; Fukuda, R.; Hasegawa, J.; Ishida, M.; Nakajima, T.; Honda, Y.; Kitao, O.; Nakai, H.; Vreven, T.; Montgomery, J. A., Jr.; Peralta, J. E.; Ogliaro, F.; Bearpark, M.; Heyd, J. J.; Brothers, E.; Kudin, K. N.; Staroverov, V. N.; Kobayashi, R.; Normand, J.; Raghavachari, K.; Rendell, A.; Burant, J. C.; Iyengar, S. S.; Tomasi, J.; Cossi, M.; Rega,

DOI: 10.1021/acs.jpca.5b00099
J. Phys. Chem. A 2015, 119, 2863–2877

N.; Millam, M. J.; Klene, M.; Knox, J. E.; Cross, J. B.; Bakken, V.; Adamo, C.; Jaramillo, J.; Gomperts, R.; Stratmann, R. E.; Yazyev, O.; Austin, A. J.; Cammi, R.; Pomelli, C.; Ochterski, J. W.; Martin, R. L.; Morokuma, K.; Zakrzewski, V. G.; Voth, G. A.; Salvador, P.; Dannenberg, J. J.; Dapprich, S.; Daniels, A. D.; Farkas, Ö.; Foresman, J. B.; Ortiz, J. V.; Cioslowski, J.; Fox, D. J. *Gaussian 09*, Revision A.2; Gaussian, Inc.: Wallingford, CT, 2009.

(20) Andrienko, G. A. *Chemcraft*, 1.6., available from:http://www.chemcraftprog.com.

(21) Singh, U. C.; Kollman, P. A. An Approach to Computing Electrostatic Charges for Molecules. *J. Comput. Chem.* **1984**, *5*, 129−145.

(22) Stearns, J. A.; Zwier, T. S. Infrared and Ultraviolet Spectroscopy of Jet-Cooled Ortho-, Meta-, and Para-Diethynylbenzene. *J. Phys. Chem. A* **2003**, *107*, 10717−10724.

(23) Mulliken, R. S. Report on Notation for the Spectra of Polyatomic Molecules. *J. Chem. Phys.* **1955**, *23*, 1997−2011.

(24) Varsanyi, G. *Assignments for Vibrational Spectra of 700 Benzene Derivatives*; Wiley: New York, 1974.

(25) Small, G. J. Herzberg-Teller Vibronic Coupling and Duschinsky Effect. *J. Chem. Phys.* **1971**, *54*, 3300−3306.

(26) Merrick, J. P.; Moran, D.; Radom, L. An Evaluation of Harmonic Vibrational Frequency Scale Factors. *J. Phys. Chem. A* **2007**, *111*, 11683−11700.

(27) Leopold, D. G.; Hemley, R. J.; Vaida, V.; Roebber, J. L. Direct Absorption Spectra of Higher Excited States of Jet-Cooled Monosubstituted Benzenes: Phenylacetylene, Styrene, Benzaldehyde, and Acetophenone. *J. Chem. Phys.* **1981**, *75*, 4758−4766.

(28) Fujita, K.; Fujiwara, T.; Matsunaga, K.; Ono, F.; Nakajima, A.; Watanabe, H.; Koguchi, T.; Suzuka, I.; Matsuzawa, H. Electronic Spectra of P-Dicyanobenzene (P-Dcnb), P-Dcnb-H_2O Complex, and P-Dcnb Dimer in a Supersonic Jet. *J. Phys. Chem.* **1992**, *96*, 10693−10697.

(29) Jiang, S.; Levy, D. H. Supersonic Jet Studies on the Photophysics of Substituted Benzenes and Naphthalenes. *J. Phys. Chem. A* **2002**, *106*, 8590−8598.

(30) Hickman, C. G.; Gascooke, J. R.; Lawrance, W. D. The S_1−S_0($^1b_2$−$^1a_1$) Transition of Jet-Cooled Toluene: Excitation and Dispersed Fluorescence Spectra, Fluorescence Lifetimes, and Intramolecular Vibrational Energy Redistribution. *J. Chem. Phys.* **1996**, *104*, 4887−4901.

(31) Struve, W. S. *Fundamentals of Molecular Spectroscopy*; Wiley, 1989; pp 245−248.

(32) Bacon, A. R.; Hollas, J. M. Duschinsky Effect Caused by Herzberg—Teller Vibronic Coupling of Two B2 Vibrations in the S_0−S_1 Systems of Benzonitrile and Phenylacetylene. *Chem. Phys. Lett.* **1985**, *120*, 477−480.

DOI: 10.1021/acs.jpca.5b00099
J. Phys. Chem. A 2015, 119, 2863−2877